The impacts of convection on upper-tropospheric and lower-stratospheric water vapor: a new perspective from satellite observations

Jing Feng （冯 婧）

Doctor of Philosophy

Department of Atmospheric and Oceanic Sciences
McGill University
Montreal, Quebec, Canada

June 2021

A thesis submitted to McGill University in partial fulfillment of the requirements of the degree of Doctor of Philosophy

Abstract

Upper-tropospheric and lower-stratospheric (UTLS) water vapor plays an essential role in controlling the outgoing longwave radiation. Convection can affect UTLS water vapor through cross-tropopause transport and by modulating the tropopause temperature. However, this mechanism remains poorly quantified due to a lack of observations above convective storms. In this thesis, we aim to understand the role of convection in shaping the humidity structure in the UTLS by developing a novel retrieval method.

First, we develop a cloud-assisted retrieval method to obtain thermodynamic fields above an overcast thick cloud layer using hyperspectral infrared observations only. Based on the Optimal Estimation approach, this method iteratively retrieves temperature and water vapor profiles above a thick cloud layer, which is approximated as a slab with uniform ice density and thickness. The retrievability of water vapor is examined by using simulations that represent different instrument settings. These experiments demonstrate that observations from operational infrared sounders, such as AIRS and IASI, contain considerable information content for retrieving lower stratospheric water vapor above thick clouds. Interestingly, we find that the underlying cloud layer improves the performance of the retrieval method compared to clear-sky conditions. Using AIRS observations, further validation with collocated aircraft data shows that this method can detect the elevated water vapor concentration due to convective moistening.

We further discover that the cloud properties near the top of convective clouds lead to non-negligible spectral uncertainties in infrared radiances. These uncertainties can be alleviated, but not fully eliminated, by assuming a slab-cloud as in the cloud-assisted retrieval.

To overcome this issue, we develop a synergistic method. This method incorporates observations from active sensors and nearest reanalysis products in synergy with hyperspectral infrared observations. The improved synergistic method retrieves temperature, water vapor, and cloud properties simultaneously. A simulation experiment is designed to investigate whether the proposed retrieval methods can capture anomalous atmospheric conditions above deep convective clouds using existing instruments. We find that the synergistic method reduces root-mean-square-errors in temperature and column-integrated water vapor by more than half and accurately reproduces the spatial distributions of temperature and humidity anomalies above convective storms.

Finally, we implement the improved method by combining infrared radiance observations from AIRS L1B products, ice water content (IWC) profile and effective radius from DARDAR-Cloud, and also atmospheric profiles from ERA5 in the nearest grid. Applying this method to satellite overpasses over tropical cyclones (TCs), we construct a dataset that contains retrieved temperature, humidity, and IWC above TCs. With a focus on the tropical tropopause layer (TTL), the influences of TCs on the TTL are investigated by creating composites of temperature, humidity, IWC, and radiative heating rates with respect to the distance to the cyclone centers. We find that overshooting convective clouds (DCC-OTs) greatly impact the TTL water budget. DCC-OTs contribute to 80 % of the TTL cloud ice above cyclones and increase the column-integrated water vapor above the tropopause by up to 40 % compared to the climatology. Other non-overshooting TTL clouds are found to be collocated with TTL temperature minima and dehydration. Overall, the synergistic retrieval reveals that cyclones increase the stratospheric humidity above them. However, further radiative transfer calculations show that the increased moisture is typically associated with radiative cooling of the TTL, which inhibits the diabatic ascent of the moistened air. Therefore, the radiative balance of the TTL under the impact of the cyclone is not in favor of maintaining the moist anomalies in the TTL or transporting water vertically to the stratosphere.

Abrégé

La vapeur d'eau dans la haute troposphère et la basse stratosphère (HTBS) joue un rôle essentiel dans le contrôle du rayonnement sortant à grandes longueurs d'ondes. La convection peut affecter la vapeur d'eau dans la HTBS par le biais de transport à travers la tropopause, ainsi qu'en modifiant la température de la tropopause. Ce mécanisme est cependant mal quantifié en raison d'un manque d'observations au-dessus des orages convectifs. Dans cette thèse, nous cherchons à comprendre le rôle de la convection dans la formation des profils d'humidité dans la HTBS en développant une nouvelle méthode d'extraction de données.

Tout d'abord, nous développons une méthode d'extraction de données assistée par les nuages (cloud-assisted) permettant d'obtenir les variables thermodynamiques au-dessus d'une couche nuageuse épaisse, en utilisant uniquement des observations hyperspectrales infrarouges. Basée sur l'approche d'estimation optimale, cette méthode recouvre de manière itérative les profils de température et de vapeur d'eau au-dessus d'une couche nuageuse épaisse approximés en tant que couche d'épaisseur et de densité de glace uniformes. Les recouvrement de vapeur d'eau sont examinés à l'aide de simulations de différents réglages d'instruments. Ces expériences démontrent que les observations obtenues par sondeurs infrarouges opérationnels, tels que le AIRS et le IASI, contiennent une quantité considérable d'information permettant de récupérer la teneur en vapeur d'eau au-dessus des nuages épais dans la basse stratosphère. Curieusement, nous trouvons qu'une couche nuageuse sous-jacente améliore les performances d'extraction de données par rapport à un ciel dégagé. En utilisant des observations AIRS, une validation supplémentaire basée sur des données provenant d'aéronefs montre que cette méthode peut détecter la concentration

élevée de vapeur d'eau due à l'humidification convective.

Par la suite, nous constatons que les propriétés des nuages près du sommet des nuages convectifs entraînent des incertitudes spectrales non négligeables pour la radiance infrarouge. Ces incertitudes peuvent être atténuées, mais pas totalement éliminées, en faisant l'approximation d'un nuage en tant que couche uniforme, comme pour la technique d'extraction de données assistée par les nuages (cloud-assisted). Pour surmonter ce problème, une méthode d'extraction de données synergique est développée. Cette méthode intègre les observations de capteurs actifs et les produits de réanalyse les plus rapprochés, en synergie avec les observations hyperspectrales infrarouges. La méthode synergique améliorée permet d'extraire simultanément la température, la vapeur d'eau et les propriétés des nuages. Une expérience de simulation est conçue afin de déterminer si les méthodes d'extraction de données peuvent détecter des conditions atmosphériques irrégulières au-dessus des nuages convectifs profonds à l'aide d'instruments existants. Nous constatons que la méthode synergique réduit de plus de moitié l'erreur quadratique moyenne sur la température et la vapeur d'eau (intégrée sur la colonne atmosphérique) et reproduit avec précision la distribution spatiale des anomalies de température et d'humidité au-dessus des orages de convection.

Pour terminer, nous intégrons la méthode améliorée en combinant les observations de radiance infrarouge du produit AIRS L1B, le profil de teneur en eau glacée (IWC, ice water content) et le rayon effectif obtenu avec DARDAR-Cloud, ainsi que les profils atmosphériques ERA5 de la zone la plus rapprochée. En appliquant cette méthode aux survols satellitaires de cyclones tropicaux (TC, tropical cyclone), nous construisons un ensemble de données qui contient la température, l'humidité et la IWC récupérées au-dessus des TC. Avec une attention particulière sur la couche de la tropopause tropicale (TTL, tropical tropoapause layer), l'impact des cyclones sur la TTL est ensuite étudiée en créant des composites de température, d'humidité, de IWC et de taux de réchauffement radiatif en fonction de la distance du centre des cyclones. Nous constatons que les nuages convectifs protubérants influencent grandement le bilan en eau de la TTL. Les nuages convectifs protubérants contribuent à 80% de la présence de glace dans les nuages de la TTL au-dessus des cyclones, et augmentent la teneur en vapeur d'eau (intégrée à la colonne atmosphérique) au-dessus de la tropopause de plus de 40% par rapport aux valeurs cli-

matologiques. D'autres nuages sans protubérance sont aussi situés dans la zone de température et déshydratation minimale de la TTL. Dans l'ensemble, l'extraction de données synergique révèle que les cyclones augmentent l'humidité stratosphérique au-dessus d'eux. Cependant, d'autres calculs de transfert radiatif montrent que l'augmentation de l'humidité est généralement associée à un refroidissement radiatif de la TTL, qui empêche l'ascension diabatique de l'air humidifié. En conséquence, l'équilibre radiatif de la TTL sous l'impact d'un cyclone ne favorise pas le maintien des anomalies d'humidité dans la TTL ou le transport vertical d'eau vers la stratosphère.

Contents

Acronyms

A-TRAIN	Afternoon Constellation
AIRS	Atmospheric Infrared Sounder
BT	Brightness Temperature
CALIOP	Cloud-Aerosol Lidar with Orthogonal Polarization
CDFS	Cumulative Degree of Freedom for Signal
CIWV	Column Integrated Water Vapor
CLARREO	Climate Absolute Radiance and Refractivity Observatory
DARDAR	raDAR/liDAR
DCC	Deep Convective Cloud
DFS	Degrees of Freedom for Signal
ECCC	Environment and Climate Change Canada
ECMWF	European Centre for Medium-Range Weather Forecasts
ERA	European Centre for Medium-Range Weather Forecasts Reanalysis
FIR	Far-Infrared
FOV	Field-Of-View
GEM	Global Environmental Multiscale model
GIIRS	Geosynchronous Interferometric Infrared Sounder
HTR	Heating Rate
LBL	Line-By-Line
IASI	Infrared Atmospheric Sounding Interferometer
IR	Infrared
IWC	Ice Water Content

IWP	Ice Water Path
LZRH	Level of Zero Radiative Heating
MAE	Mean Absolute Error
MIR	Mid-Infrared
MLS	Microwave Limb Sounder
MODTRAN	MODerate resolution atmospheric TRANsmission
NESR	Noise Equivalent Spectral Radiances
NWP	Numerical Weather Prediction
OT	Overshooting
PDF	Probability Density Function
PPMV	Parts Per Million by Volume
RMSE	Root-Mean-Square-Error
STD	Standard Deviation
TC	Tropical Cyclone
TES	Tropospheric Emission Spectrometer
TOA	Top-Of-Atmosphere
TTL	Tropical Tropopause Layer
UTC	Coordinated Universal Time
UTLS	Upper-Troposphere and Lower-Stratosphere
WV	Water Vapor

List of Figures

List of Tables

Acknowledgements

First and foremost, I would like to express my sincere gratitude to my supervisor, Prof. Yi Huang, for his invaluable guidance, encouragement, patience, and caring throughout my Ph.D. study. I especially thank him for always motivating my research, responding to every question and inquiry, providing concrete feedback that helps me improve, and guiding my future career path. I will always look up to his passionate dedication to a high standard of research while always being humble, patient, and considerate to others.

I would like to thank members of my defence committee, Prof. Jonathon Wright, Prof. Frederic Fabry, Prof. David Straub, Prof. Frederic Fabry, Prof. Nicolas Cowan, for their valuable feedbacks on the thesis. I am grateful to members of my supervisory committee, Prof. Andreas Zuend and Prof. Peter Yau, for their constant encouragements and inspiring feedbacks. I thank Dr. Zhipeng Qu, who shared the numerical simulation outputs and offered timely support with the project. I thank Charles Brunette and Anäis M. Podrabinok for translating the French version of the abstract. My friends and colleagues, Lei Liu, Xun Wang, and Kevin Bloxam, provided me with generous help that improves my papers, proposals, and this dissertation. I sincerely appreciate their kind support.

I would like to acknowledge the financial support from Mr. and Mrs. Leong Fellowship granted by McGill University and a top-up offered by Prof. Yi Huang for recognizing my work and supporting my study at McGill.

I would like to extend my gratitude to many friends and colleagues. I am deeply indebted to Yuwei Wang for his selfless help in almost every aspect of my research and life. I am sincerely thankful to Sisi Chen for cheering me up and sharing her academic experiences. I also had the great pleasure of working with my colleagues and officemates, Dalrin Ampritta, Qiurun Yu, and David Wang. Particularly helpful to me during this time were my friends, Shijia Li and Yuchen Liu, who enriched my life by engaging me in outdoor recreations.

Finally, I feel lucky to be unconditionally loved by my family. I would like to thank my best friend, the love of my life, and my husband, Xu Dai, without whom I would be on a different path than I am today. I thank my parents-in-law for their encouragement and financial supports. My cat, Bingxiang, and all my friends and families back in China must be acknowledged for their emotional supports. The last words go to my parents, Zhaoyun Feng and Yufen Ju, for their love that raised me up. This dissertation is dedicated to them.

Contributions of Author

This thesis consists of five chapters: an introduction, three original articles, and a conclusion. The first article has been published in the Journal of Atmospheric and Oceanic Technology. The second and third articles have been submitted for publication. Yi Huang conceptualized the work described in Chapter 2 and the numerical model simulation conducted in Chapter 3. Jing Feng and Yi Huang co-designed the work described in Chapters 3 and 4. Zhipeng Qu carried out the numerical model simulation in Chapter 3. Jing Feng developed and implemented the retrieval, collected the data, conducted the analysis, and wrote the paper under the supervision of Yi Huang.

Contributions to Original Knowledge

1. The work described in Chapters 2 and 3 develops a novel, synergistic method to retrieve thermodynamic profiles from hyperspectral infrared radiance observation. This method has a unique advantage in retrieving temperature and water vapor profiles simultaneously in the presence of clouds.

2. The study conducted in Chapter 4 offers the first infrared hyperspectra-based dataset of thermodynamic profiles above convective clouds. This datset provides strong evidence of direct hydration in the upper-troposphere and lower-stratosphere (UTLS) right above overshooting deep convective clouds for the first time using remote sensing techniques.

3. The study in Chapter 4 challenges the conventional view that radiative heating favors the transport of air from convective outflow to the stratosphere. On the contrary, this study shows that radiative cooling effects of clouds and water vapor greatly suppress the transport of air masses across the isentropic surfaces. Under this condition, convectively injected moisture is less likely to stay within the UTLS.

1
Introduction

Water forms the fundamental parts of Earth's climate system. In its gaseous phase, water vapor is the most important greenhouse gas [Mitchell, 1989]. It enhances the climate sensitivity to anthropogenic emissions because increased moisture in a warming climate amplifies the greenhouse effect [IPCC, 1990].

Water vapor decreases exponentially with height as the atmosphere gets colder, leading to a dry upper-troposphere and lower-stratosphere (UTLS). Despite its scarcity, water vapor in the UTLS has fundamental radiative and chemical effects. The radiative budgets at the top-of-atmosphere (TOA) are especially sensitive to UTLS water vapor due to a sharp thermal contrast between the warm surface and the cold UTLS, as opposed to other vertical ranges [Held and Soden, 2000, Huang et al., 2010]. Like other greenhouse gases in the UTLS, water vapor radiatively cools the stratosphere but warms the troposphere. Hence, an increase in stratospheric water vapor may accelerate the decadal rate of surface warming [Solomon et al., 2010].

As a primary source of reactive hydrogen species, stratospheric water vapor is involved in the catalytic loss cycles of ozone [Hampson, 1964, Dvortsov and Solomon, 2001]. In the polar stratosphere, water vapor also impacts ozone loss via its role in heterogeneous chlorine activation by affecting the threshold temperature and the formation of polar stratospheric clouds [Solomon et al., 1986, Vogel et al., 2011, Kirk-Davidoff et al., 1999, Drdla and Müller, 2012].

1.1 How convection may impact UTLS water vapor

Air enters the stratosphere primarily across the tropical tropopause layer [TTL, Brewer, 1949, Fueglistaler et al., 2009], which connects the underlying convective overturning circulation and the Brewer-Dobson circulation in the stratosphere. As a result of mean atmospheric circulation and convection, air can rise above the bottom of TTL. Once in the TTL, it tends to rise further into the stratosphere and is then carried poleward by the Brewer-Dobson circulation. The ascent motion across the isentropic surface is supported by prevailing radiative heating in the TTL.

In this tropical entry process, it is widely accepted that the maximum amount of water vapor entering the stratosphere is determined by the tropopause temperature [Brewer, 1949, Holton and Gettelman, 2001, Gettelman et al., 2002a] through a ‘freeze-drying’ mechanism. However, this thermal control process of stratospheric water vapor cannot explain the recent observed decadal increase in stratospheric water vapor [Oltmans et al., 2000, Rosenlof et al., 2001, Hurst et al., 2011] since the tropopause was observed to be cooling over the same period [Rosenlof et al., 2001, Randel et al., 2004]. This decadal increase in water vapor cannot be fully explained by methane oxidation [Rosenlof et al., 2001] either. Hence, the long-term trend in stratospheric water vapor must be attributed to other mechanisms.

As an important pathway for airmasses to reach the tropopause, the role of convection in UTLS water vapor remains poorly quantified. Through a combination of dynamical and radiative cooling [Holloway and Neelin, 2007, Rivoire et al., 2020], deep convection is related to cold tropopause temperature on both small and large scales [Gettelman et al., 2002b]. Hence, convection can impact the stratospheric water vapor by modulating the tropopause temperature [Randel et al., 2015].

Substantial evidence that convection reaches above the level of neutral buoyancy has been obtained [Fueglistaler et al., 2009, Solomon et al., 2016]. Observations have found that overshooting convection in tropical and mid-latitude storms can inject water vapor and ice crystals into the stratosphere [Corti et al., 2008, Anderson et al., 2012], leading to extreme moistening events that persist for hours [Werner et al., 2020]. These deep convective events evidently impact the ice transport into the tropical stratosphere [beyond the cold-point tropopause, Bolot and Fueglistaler, 2021].

However, the overall impact of overshooting convection on the global stratospheric water vapor budget is still poorly understood. As suggested by Jensen et al. [2007], convectively injected ice can be either a source or a sink of water vapor. Depending on the pre-existing relative humidity [Jensen et al., 2007], the injected ice particles can either sublimate in a sub-saturated environment or cause deposition and sedimentation in a supersaturated environment. This mechanism is controlled by multiple processes, including deposition growth, sedimentation, sublimation, and dynamical transport, that are not well constrained by observations. For example, observational studies show that supersaturation frequently occurs in the TTL [Jensen et al., 2013] and the efficiency of dehydration in the TTL might be lower than expected [Rollins et al., 2016]. Despite the observed evidence of convective hydration above both tropical [e.g., Corti et al., 2008, Schiller et al., 2009] and mid-latitude convection [e.g., Anderson et al., 2012, Sun and Huang, 2015, Smith et al., 2017], studies have argued that the overall contribution of overshooting convection to the stratospheric water vapor budget might be insignificant [e.g., Ueyama et al., 2018, Schoeberl et al., 2019, Randel and Park, 2019].

In summary, deep convection may impact both the tropical and mid-latitude entry of water vapor by modulating the tropopause temperature and cross-tropopause mass transport. It is an open question how deep convection, especially overshooting convection, impacts on UTLS water vapor.

1.2 Limitations of current observations and simulations

The understanding of convective impacts on UTLS water vapor is impeded by limitations in current observations and simulations. Current global reanalysis datasets do not agree well with observation in the UTLS [Jiang et al., 2015, Davis et al., 2017]. They tend to produce a persistent wet bias in the upper-troposphere and have large discrepancies in the lower-stratosphere among different products [Huang et al., 2007, Jiang et al., 2012, 2015, Davis et al., 2017], due to several known issues in the forecast models and the assimilation process. These reanalysis datasets have different treatments in radiative schemes and convective schemes [e.g., in treating entrainment and detrainment, Wright et al., 2020]. Few cloud schemes (except in ERA) allow supersaturation with respect to ice, which is frequently observed in the UTLS [Schoeberl et al., 2019]. The problems in these schemes lead to a large spread in high cloud amounts and TTL diabatic heating budgets [Wright and Fueglistaler, 2013, Wright et al., 2020], both of which are fundamental to tropical tropopause temperature and UTLS water vapor. Other problems include the lack of parametrized methane oxidation [except in ERA, Davis et al., 2017] and significant biases in vertical and horizontal transports [Jiang et al., 2015, Schoeberl et al., 2012]. It also should be noted that UTLS water vapor products from some reanalyses may not be physically meaningful because of a strong relaxation to observed climatology [e.g., MERRA and MERRA-2 Davis et al., 2017]. These issues are not constrained by assimilation, as UTLS water vapor observations and all-sky infrared radiances are not assimilated [Davis et al., 2017], leading to poor agreements between reanalysis and observations.

Observations of UTLS water vapor are limited in time and space and are rarely available above convective storms. Balloon-borne and airborne in-situ measurements [e.g., Corti et al., 2008, Hurst et al., 2011, Anderson et al., 2012, Jensen et al., 2013, Lee et al., 2019] have greatly advanced the understanding of the UTLS water vapor, but are limited to specific campaigns. Although several aircraft campaigns have targeted deep convective events, it remains a challenge to sample air in extreme weather conditions near the tops of storms. While the operational radiosonde network performs poorly in the cold and low-pressure environment of UTLS [Kley, 2000], current satellite remote sensing instruments do provide global observations of UTLS water. However, current retrieval products from these instruments may not be suitable for assessing convective impacts. For example, the water vapor products in overcast conditions provided by hyperspectral infrared sounders are not reliable due to the cloud-clearing retrieval scheme [Susskind et al., 2003, Gambacorta et al., 2014, Zhou et al., 2005]. Satellite instruments based on microwave emissions or occultation techniques are sensitive to stratospheric water vapor, but they have limited sensitivity to small-scale variations due to a large sampling footprint. Moreover, the strong scattering of thick convective clouds may degrade the data quality of microwave sounders [such as MLS, Livesey et al., 2017]. Therefore, current observations are not sufficient in quantifying convective impacts on UTLS water vapor.

1.3 Outline of Dissertation

The lack of observations of UTLS water vapor above convective storms, in conjunction with the potentially large convective impact, motivates the development of a satellite retrieval method to provide the humidity structure above convective storms. This dissertation is structured as follows:

In Chapter 2, a cloud-assisted retrieval method is developed. This method uses an airborne hyperspectral infrared sounder alone to retrieve atmospheric states above thick cloud layers. Following a set of simulation experiments, we investigate the optimal spectral specification for detecting UTLS water vapor to provide a guideline for future instruments.

In Chapter 3, the uncertainties in infrared radiances induced by cloud properties near the tops of convective clouds are assessed. We then develop a synergistic retrieval method that combines infrared sounders, active sensors, and outputs from numerical weather prediction models to constrain retrieval uncertainties. Furthermore, we conduct an observation system simulation experiment to evaluate the ability of retrieval methods in detecting the spatial distributions of thermodynamic anomalies above convective storms.

In Chapter 4, by implementing the synergistic retrieval method with operational satellite instruments, we construct a satellite observational dataset of thermodynamic conditions above tropical cyclone events. Using this dataset, we quantitatively evaluate the impacts of tropical cyclones on cloud, temperature, water vapor, and radiative heating in the TTL.

Finally, Chapter 5 summarizes the main contributions of this dissertation and discusses future research.

2

Cloud-assisted retrieval of lower stratospheric water vapor from nadir view satellite measurements

This study examines the feasibility of retrieving lower stratospheric water vapor using a nadir infrared hyperspectrometer, with a focus on the detectability of small-scale water vapor variability. The feasibility of the retrieval is examined using simulation experiments that model different instrument settings. These experiments show that the infrared spectra, measured with sufficient spectral coverage, resolution and noise level, contain considerable information content that can be used to retrieve lower stratospheric water vapor. Interestingly, it is found that the presence of an opaque cloud layer at the tropopause level can substantially improve the retrieval performance, as it helps remove degeneracy in the retrieval problem. Under this condition, an elevated lower stratospheric water vapor concentration, for instance, caused by convective moistening, can be detected with an accuracy of 0.09 $\mathrm{g/m^2}$ using improved spaceborn hyperspectrometers. The cloud-assisted retrieval is tested using measurements from the Atmospheric Infrared Sounder (AIRS). Validation against collocated aircraft data shows that the retrieval can detect elevated water vapor concentration due to convective moistening.

2.1 Introduction

Despite its scarcity, stratospheric water vapor is an important atmospheric composition due to its radiative and chemical effects. It radiatively cools the stratosphere but potentially warms the troposphere and surface [Solomon et al., 2010, Dessler et al., 1995, Huang et al., 2016]. It also may affect total ozone loss rate through several chemical processes [Anderson et al., 2012].

However, current satellite observations have limited ability to detect stratospheric water vapor variations. Satellite nadir view radiance measurements usually do not have sufficient sensitivity to the low concentration of stratospheric water vapor, while limb view measurements have large sampling footprints, making small-scale water vapor variability hard to detect. Current global climate models also have various deficiencies in their simulations of lower stratospheric water vapor, mostly caused by temperature bias [e.g., Schoeberl et al., 2012] and representation of the deep convection process [e.g., Neale et al., 2010].

Aircraft in situ observations have demonstrated that lower stratospheric water vapor is highly variable. For instance, Anderson et al. [2012] showed that in the data samples taken by summertime flights over North America, convective moistening occurs on nearly 50% of these flights, with elevated lower stratospheric water vapor concentrations being as high as 15 ppmv. Although composite analyses suggest deep convection tends to elevate water vapor concentration in the upper troposphere and lower stratosphere in this region [Sun and Huang, 2015, e.g.,], there has been no conclusive evidence of convective moistening resulted from individual convective events from satellite water vapor measurements [Schwartz et al., 2013, [e.g.,]. It is likely due to the large footprint size and coarse vertical resolution (which lead to significant spatial averaging) of the current instruments such as Microwave Limb Sounder (MLS). These previous studies highlight the need to improve the monitoring of stratospheric water vapor variability.

As advanced nadir-view satellite measurements have relatively small footprints and high spectral resolution, they are better suited for monitoring small-scale water vapor variability in the lower stratosphere with relatively high vertical resolution. However, nadir retrieval of lower stratospheric water vapor is challenging because 1) the water vapor variability is much smaller in the lower stratosphere than in the upper troposphere right across the tropopause, which induces significant uncertainty in lower stratospheric water vapor retrieval due to the smoothing effect (see the discussion in section 2.2.3); and 2) the temperature variation is not monotonic around the tropopause, which causes the retrieval to lack the thermal contrast necessary for attributing a water vapor anomaly to a particular vertical level. In theory, these limitations can be largely relieved if there is an opaque cloud layer right at the tropopause, which blocks the upwelling radiation from the troposphere. In this study, we test the feasibility of this retrieval idea, i.e., the sensitivity of the retrieval to stratospheric water vapor with the presence of an opaque cloud, using an evaluation framework similar to Bani Shahabadi and Huang [2014]. In section 2.2.2, we first investigate the Information Content in such a retrieval using synthetic satellite radiance simulated from atmospheric profiles and adopting a widely-used optimal estimation method [Rodgers, 2000] that simultaneously retrieves the stratospheric temperature and humidity. In section 2.2.3, we present test retrieval results under various sensor specifications based on simulation experiments. In section 2.2.4, retrievals based on the Atmospheric Infrared Sounder [Chahine et al., 2006, AIRS;] radiance data are attempted and compared to collocated airborne in situ measurements.

2.2 Retrieval Method and Information Content

2.2.1 Retrieval method

The retrieval method is based on the optimal estimation method [Rodgers, 2000]. The relationship between atmospheric quantities and measurements can be linearized as :

$$\begin{aligned} y &= F(x_0) + \frac{\partial F}{\partial x}(x - x_0) + \varepsilon \\ &= y_0 + K(x - x_0) + \varepsilon \end{aligned} \tag{2.1}$$

Here the state vector x contains temperature and the logarithm of specific humidity at 60 fixed pressure levels (15 of them are in the stratosphere). y refers to upwelling radiances measured at the top of atmosphere, and ε is the residual that includes measurement error and forward model error. We use the MODerate resolution atmospheric TRANsmission 5.0 [MODTRAN, Berk et al., 2005] to compute synthetic radiance $F(x)$, and the Jacobians K (see fig. 2.1 for illustration). The quantity x_0 is the prior guess of state vector, and y_0 is the corresponding synthetic radiance.

The goal then is to solve for x, the truth atmospheric state vector, through an inverse model. Because the retrieval problem is ill-posed, it is not appropriate to directly invert the Jacobian matrix K to solve for x. We adopt a Bayesian inference-based optimal estimation method instead [Rodgers, 2000]. $\hat{x}$, the best estimate of x can be derived as:

$$\hat{x} = x_0 + GK(x - x_0) + G(y - Kx) \tag{2.2}$$

$$G = S_a K^T (K S_a K^T + S_\varepsilon)^{-1} \tag{2.3}$$

where S_a is the covariance matrix of state vector, S_ε is the covariance matrix of measurement error.

Applying the Gaussian-Newton iteration method, the iteration formula for $\hat{x}_{i+1}$ at each iteration time step then becomes:

$$\hat{x}_{i+1} = x_0 + (K_i^T S_\varepsilon^{-1} K_i + S_a^{-1})^{-1} K_i^T S_\varepsilon^{-1} [y - F(\hat{x}_i) + K_i(\hat{x}_i - x_0)] \tag{2.4}$$

where K_i is the Jacobian matrix computed at the ith time step.

The Jacobian matrix K is computed by finite differencing, $\frac{\partial F(x)}{\partial x} = \frac{F(x+\Delta x) - F(x)}{\Delta x}$, where the perturbation Δx is 1 K for temperature and 10% for specific humidity. Logarithmic scaling is used for water vapor, i.e., $K_q = \frac{\partial F}{\partial ln(q)}$, because its radiative effect is logarithmically dependent on its concentration [Huang and Bani Shahabadi, 2014]. As shown in Fig. 2.1, a positive Jacobian value reveals an increase in TOA observed radiance in response to an increase in atmospheric temperature or specific humidity.

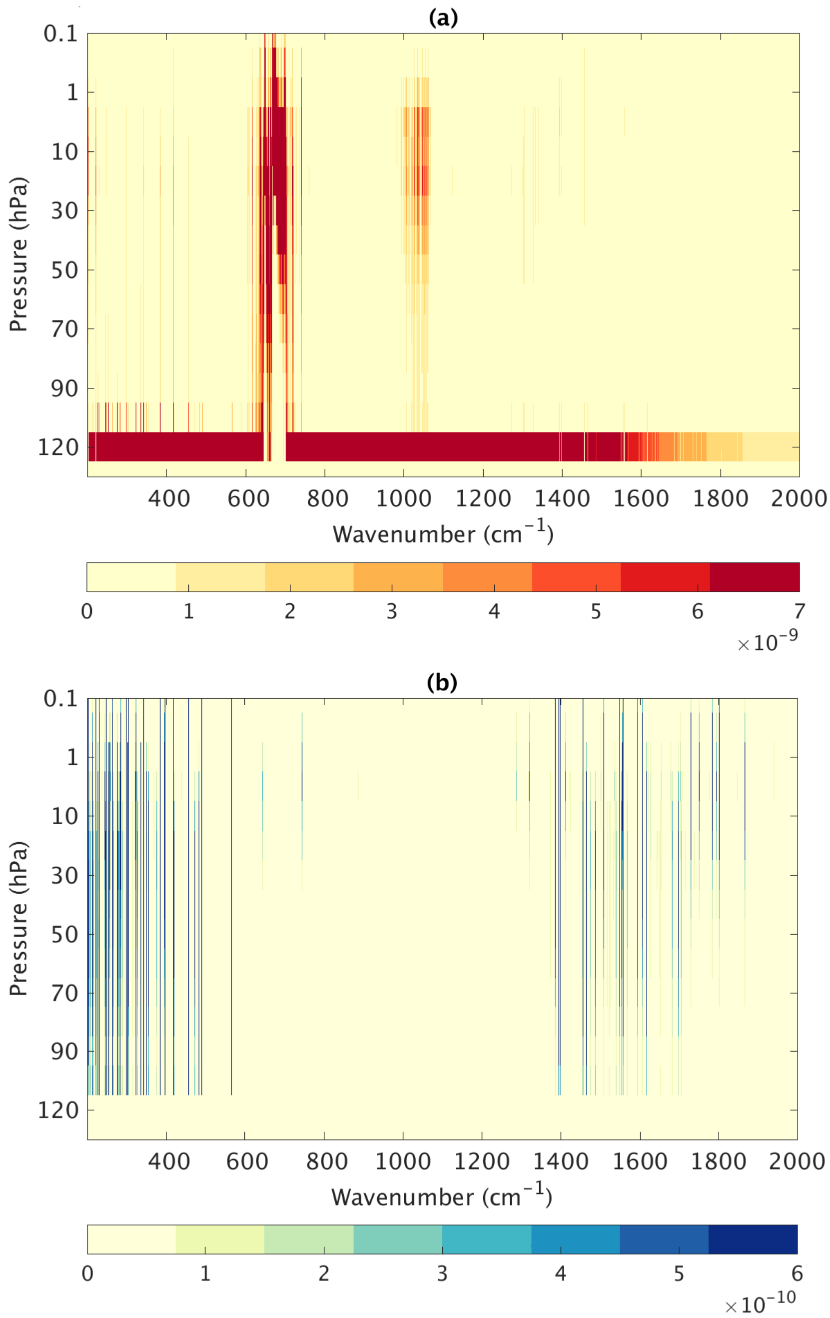

Figure 2.1: Spectral Jacobian in terms of brightness temperature of (a) temperature ($\mathrm{K/K}$) and (b) water vapor ($\mathrm{K/log(g/kg)}$) computed with an opaque cloud layer located at 120 hPa, using MODTRAN 5.0 for spectral range from 200 to 2000 $\mathrm{cm^{-1}}$, with a spectral resolution of 0.1 $\mathrm{cm^{-1}}$. Note that the temperature and water vapor Jacobian used in the retrieval are in units of $\mathrm{W/(cm^2 sr cm^{-1})/K}$ and $\mathrm{W/cm^2 sr cm^{-1}}$, respectively.

2.2.2 Prior

To form the prior knowledge on the retrieval quantities, 5051 atmospheric profiles with their tropopause at 120 hPa are obtained from 6-hourly ERA-interim [ECMWF Interim Re-Analysis, Dee et al., 2011] dataset within the region of $40°$N - $60°$N and $100°$W - $130°$W, from the year 2000 to 2013. As mentioned earlier, this dataset does not depict small-scale (sub-grid) variations of stratospheric water vapor, and tends to have a dry bias in the stratosphere [Schoeberl et al., 2012]. To account for such variability, we applied artificial moistening to the lower stratosphere. Although the exact pattern of lower stratospheric moistening is still not clear, previous studies have shown several clues. First, enhanced water vapor may enter the lower atmosphere from several sources, including horizontal transport from tropical tropopause layer driven by large-scale air motion and vertical transport from troposphere driven by overshooting convection [Smith, 2013, Grosvenor et al., 2007, Dessler et al., 1995]. Elevated water vapor mixing ratios up to 15 ppmv are observed across the lower stratosphere ranging from the tropopause to 50 hPa [Anderson et al., 2012]. To represent these observed moist features, random enhancements of water vapor that linearly decrease with pressure level are added to the original profiles from 200 hPa to 50 hPa, where the increase of water vapor at 120 hPa has a mean of 5 ppmv and a standard deviation of 5 ppmv (negative value is set to be zero). 5051 moistened profiles, together with 5051 original profiles from ERA-interim, comprise the prior knowledge. A subset of them is shown in Fig. 2.2.

In our retrieval, the covariance matrix S_a is useful in that its diagonal elements show the uncertainty in the prior estimate and its off-diagonal elements reflect the correlation between the state vector elements. The covariance matrix can be calculated directly from the atmosphere profiles as mentioned above (the 10102 profiles). However, S_a computed this way includes correlation between different layers due to artificial moistening. An alternative approach is to keep the correlation of original dataset without moistening, but add variance to the lower stratosphere and upper troposphere. Following this idea, a correlation matrix $R_0[120 \times 120]$ is first calculated based on the original data from ERA-interim. The R (shown in Fig. 2.3) is converted back to covariance matrix S_a based on the standard deviations of the enlarged datasets with artificial moistening, as shown in Eq. 2.5.

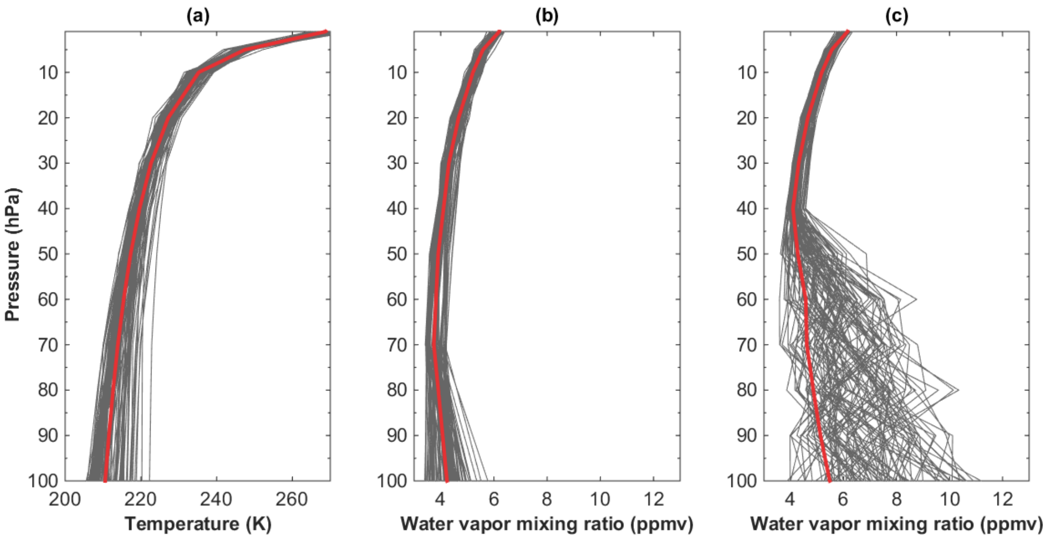

Figure 2.2: (a) Temperature profiles, (b) original water vapor mixing ratio profiles, and (c) artificially moistened water vapor mixing ratio profiles. Grey curves in each panel are 20 randomly selected profiles, and the red curve shows the mean.

$$\begin{aligned}
&R = D_0 S_{a0} D_0;\\
&D_{0ii} = 1/d_0(i),\ i = 1, ..., 120;\\
&D_{ii} = d(i),\ i = 1, ..., 120;\\
&S_a = DRD;
\end{aligned} \tag{2.5}$$

Where vector d_0 and d are the standard deviations of the original and moistened dataset, respectively.

2.2.3 Forward Model

We first examine the retrieval feasibility with a hypothetical ideal instrument. This ideal instrument is assumed to have spectral coverage from 200 to 2000 cm^{-1}, with 0.1 cm^{-1} spectral resolution, and uncorrelated uniform noise level at $\sigma = 2.5 \times 10^{-8}\ \mathrm{W/(cm^2 srcm^{-1})}$ (about 0.1K in the Mid Infrared, using 200K as the background temperature). Normally distributed random noise with mean 0 and standard deviation σ is generated and added to forward model-calculated radiance F(x) to mimic measurements with sensor noise, following Eq.1. In addition, several cases (see Table 2.1) are designed to examine the effect of spectral coverage, spectral resolution, and noise level, testing the possibility of performing this retrieval with different instrument specifications.

A layer of opaque cloud with uniform ice particle density of 1.5 $\mathrm{g/m^3}$ is prescribed right below the tropopause level, at 120 hPa, which effectively blocks radiative emission from layers below. Instead of iteratively retrieving it, cloud top temperature is computed directly from the mean brightness temperature in the window band (wave number from 850 cm^{-1} to 900 cm^{-1}), as the emissivity of the cloud is close to 1. Cloud optical parameters are prescribed according to the library of Yang et al. [2013] to simulate reflectance and transmittance throughout the spectra.

The quality of retrieval is assessed with different metrics. The root-mean-square error (RMSE) indicates the uncertainty in the retrieval at each level, and the mean error shows the systematic bias in the retrieval.

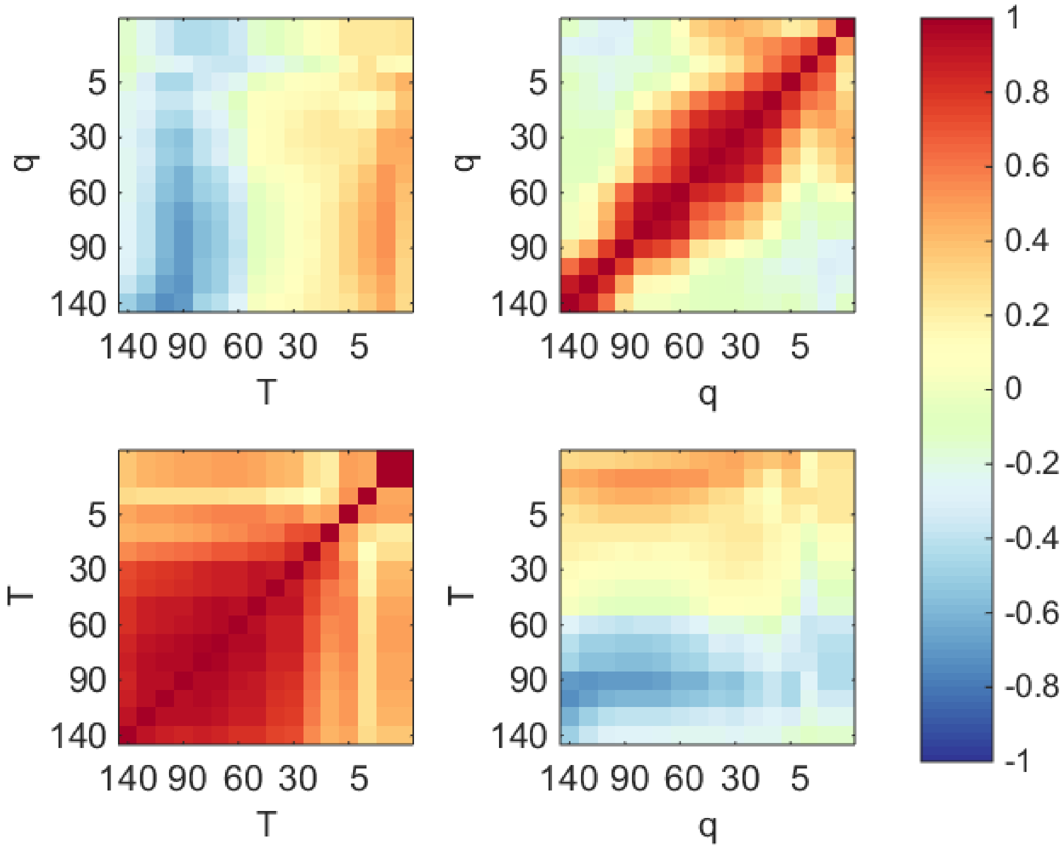

Figure 2.3: Correlation matrix of the state vector. 'T' refers to temperature, and 'q' is the logarithm of water vapor mixing ratio. The tick labels along the axes are pressure levels in hPa.

Table 2.1: Hypothetical sensor specification and performance assessment. The DFS and featured changes in RMSE are calculated for stratospheric levels from 100 hPa to 40 hPa. Prior RMSE for T, WV, and CIWV is 2.26 K, 1.07 ppmv, and 0.31 $\mathrm{g/m^2}$ respectively

	Spectral parameters			Opaque cloud at tropopause					Clear sky				
				DFS		RMSE			DFS		RMSE		
Case	Noise level [W/(cm²srcm⁻¹)]	Coverage [cm⁻¹]	Resolution [cm⁻¹]	T	WV	T [K]	WV [ppmv]	$CIWV$ [g/m²]	T	WV	T	WV	$CIWV$
1	0.25×10^{-8}	200-2000	0.1	9.03	2.68	0.30	0.65	0.09	7.85	2.68	0.34	0.73	0.18
2	0.25×10^{-7}	650-2000	0.1	6.30	0.90	0.38	1.04	0.29	5.10	0.31	0.48	1.07	0.31
3	0.75×10^{-8}	650-2000	0.5	6.30	0.92	0.39	1.00	0.27	5.26	0.51	0.54	1.07	0.31
4	0.75×10^{-8}	650-2000	0.1	7.71	1.33	0.33	0.91	0.23	6.77	1.24	0.36	0.97	0.28
5	0.25×10^{-8}	650-2000	0.5	7.62	1.15	0.34	0.92	0.23	6.59	1.07	0.40	1.07	0.31
6	0.25×10^{-7} 0.25×10^{-7}	200-650 650-2000	0.1	6.44	1.53	0.37	0.81	0.18	5.47	1.34	0.48	0.85	0.23
7	0.25×10^{-7} 0.75×10^{-8}	200-650 650-2000	0.5	6.31	1.11	0.38	0.88	0.21	5.29	0.97	0.53	1.01	0.31

2.2.4 Information Content

A retrieval is expected to reduce uncertainty in lower stratospheric temperature and water vapor mixing ratio, and to distinguish moistened cases from unmoistened cases. In order to test the retrieval method proposed here, a test data set consisting of 200 profiles are randomly selected. Several scenarios (Table 2.1) with different instrumental parameters are designed to test the feasibility of this retrieval using current or improved satellite instruments.

We first use the concept of degrees of freedom for signal [Rodgers, 2000] to assess the retrieval potential. The averaging kernel A, derived from Eq. 2.4, relates retrieved quantities to their truth values:

$$\hat{x}_{i+1} - x_0 = A(x - x_0) \tag{2.6}$$

where $A = (K^T S_\varepsilon^{-1} K + S_a^{-1})^{-1} K^T S_\varepsilon^{-1} K$. A narrowly shaped row vector of A peaking at the corresponding pressure level would indicate high vertical resolution. Fig. 2.4a and Fig. 2.4b presents a few selected row vectors of the averaging kernel for temperature and water vapor retrievals at 100, 50 and 10 hPa, demonstrating that the water vapor concentrations at these levels can be delineated to a certain extent.

The degrees of freedom for signal (DFS), which is the trace of A, is calculated here to provide an estimate on how much independent information can be obtained in the retrieval [Rodgers, 2000]. Table 2.1 shows the DFS for a variety of instrument specifications tested in this study. The DFS values show how the retrieval is impacted by the spectral coverage (inclusion of the Far Infrared (FIR) in particular), spectral resolution, and instrument noise.

In agreement with the DFS values, spectral signals due to enhanced water vapor also reveal the effects of the different instrument parameters. An effective retrieval requires signals larger than the measurement noise, the prescriptions of which in our tests are shown by dashed lines in Fig. 2.5. Because the signal strength essentially depends on the spectral resolution, a finer resolution potentially leads to improved retrieval performance given the same noise level.

As we are most interested in lower stratosphere from 100 hPa to 40 hPa, CDFS (cumulative DFS normalized by the total DFS) is used to demonstrate how the information content distributes across the vertical profile (Fig. 2.4c). Although the DFS has similar values in the two cases (see Table 2.1), the CDFS in the cloudy sky is constantly higher than the clear sky down to where the cloud is located. It is illustrated in Fig. 2.4, that the averaging kernels of the lowermost stratospheric layers (e.g., at 100 hPa) in the cloudy case are noticeably narrower and, very importantly, inhibits the tropospheric effects from below the cloud level, where the water vapor variability (uncertainty) is order-of-magnitude larger. This advantage is verified by the retrieval tests below.

2.3 Simulation experiments with different instrument specifications

In case 1, we present the performance of the above-mentioned ideal instrument to illustrate the theoretical limits of the retrieval. As shown in Fig. 2.5a and b, this instrument specification fully enables the TOA spectrum to capture signals coming from lower stratospheric moistening.

Current satellite missions, however, do not meet these instrumentation requirements

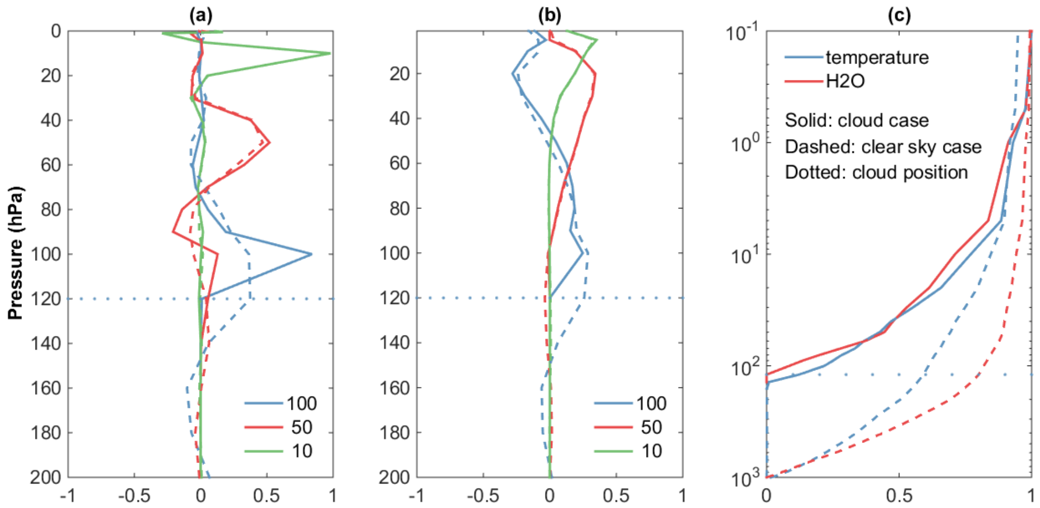

Figure 2.4: Rows of averaging kernel matrix that correspond to 100, 50, and 10 hPa for (a) temperature and (b) specific humidity retrievals. (c) Cumulative degrees of freedom for signal for temperature (blue) and water vapor (red).

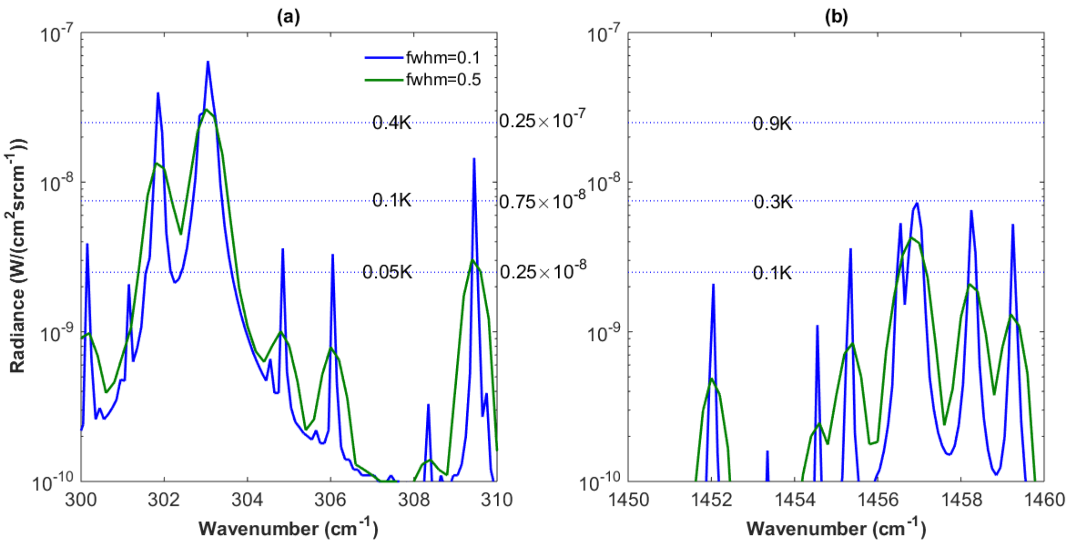

Figure 2.5: Spectral signals of elevated water vapor in a selected case (Truth in Fig. 6) in the water vapor (a) rotational and (b) vibration-rotational band, with with 0.1 cm^{-1} and 0.5 cm^{-1} resolution respectively. The dotted lines show the three noise levels specified in the test, converted to brightness temperature units using 200 K as reference temperature.

simultaneously. The IR spectrometer carried by AIRS has a noise level of 0.75×10^{-8} $\mathrm{W/(cm^2 sr cm^{-1})}$ (0.3 K in MIR), but its resolution is coarser than 0.5 $\mathrm{cm^{-1}}$. Though the Tropospheric Emissions Spectrometer [TES; Beer et al., 2001] has a high spectral resolution, its noise level is higher. Fig. 2.5 suggests the inclusion of FIR measurements, as designed for the Climate Absolute Radiance and Refractivity Observatory [CLARREO, Wielicki et al., 2013], may be helpful, in that signals at some FIR frequencies are of greater magnitude.

Several cases are then designed to test the effects of different instrument settings in light of these instruments. Table 2.1 lists detailed instrument settings in each case, with corresponding retrieval results shown in Fig. 2.7. Note that all the listed values for the RMSE are computed based on levels between 100 hPa and 40 hPa, the vertical range of most concern in this study. Among them, case 1 is the ideal case that combines optimal noise and spectral resolution with an extended spectral region to obtain the best representation of the true water vapor profile. Case 2 is designed to represent instrument specifications of TES, and case 3 is for AIRS. Cases 4 and 5 consider the cases if the measurement errors for AIRS and TES are reduced, which can be realized by taking multiple measurements of the same target or extending the stare time (e.g., if deployed on a geostationary satellite), or hypothetically, by reducing detector noise. Cases 6 and 7 are designed to assess the effect of FIR coverage. Retrieval tests are performed using these parameter specifications under both cloudy (opaque cloud at the tropopause) and clear sky scenarios.

In the ideal case, the retrieval process greatly decreases the uncertainty in the state vector compared to prior guess, as shown in Fig. 2.6 and Fig. 2.7. With a fine spectral resolution of 0.1 $\mathrm{cm^{-1}}$ and a low noise level, the retrieval result is able to detect the elevation of water vapor concentration. The retrieval process reduces uncertainty (RMSE) in temperature, water vapor, and column integrated water vapor (CIWV) by 87%, 40%, and 69% , respectively. As inferred from the relatively low vertical resolution indicated by the averaging kernel, the retrieval cannot perfectly reproduce an individual moistening profile (place the anomalous water vapor at the right place), but it reduces systematic bias at each level dramatically with a satisfactory estimation of CIWV.

For different sensor specifications, temperature retrieval in all the cases reaches $\leqslant 1$ K uncertainty in the lower stratosphere, but the quality of water vapor retrieval differs. In accordance with our expectation, cases 2 and 3 have limited reduction of uncertainty in water vapor, although it seems case 3 (AIRS) has some potential to detect strong moistening. Cases 4 and 5 indicate that reduction in measurement error improves retrieval accuracy. Moreover, cases 6 and 7 highlight the coverage of FIR with good radiometric accuracy would significantly reduce the uncertainty, achieving an accuracy of $\leqslant 0.88\ \mathrm{ppmv}$ for lower stratospheric mean water vapor mixing ratio. Among all six non-ideal sensor specifications, case 6 provides best retrieval quality, which affords 0.38 K accuracy for temperature, 0.21 $\mathrm{g/m^2}$ for column integrated water vapor in the lower stratosphere.

It is interesting to note that although the information contents for water vapor retrievals are comparable in the clear-sky case, the retrieval tests show that the retrieval performance is worse in the clear-sky case. The reduction in uncertainty is generally only half of that accomplished in the cloudy case. As reasoned above, this is because of the obscuration of the upper tropospheric water vapor variability. As indicated by the averaging kernel (Fig. 2.4b), there are substantial contributions across the tropopause level in the clear sky case. The presence of a cloud layer at the tropopause effectively eliminates such complication as well as the degeneracy caused by the non-monotonic change in temperature across the tropopause.

When examining the performance of this retrieval method, two different moistening patterns are investigated using ideal instrumentation settings. The first one is the case with enhanced water vapor continuously extending from cloud top to 50 hPa. It reaches 51% and 80% uncertainty reduction for water vapor mixing ratio and CIWV respectively. Another one is with isolated moistening in one 20 hPa segment. In this case, retrieval results show 21% uncertainty reduction for water vapor mixing ratio, and 42% for CIWV. The inferior performance in the latter case is because the retrieval process can not always place the elevated water vapor at the right vertical level due to the limited vertical resolution of the retrieval technique as indicated by the averaging kernel in Fig. 2.4.

This retrieval method uses known cloud properties to assist stratospheric retrieval, uncertainty in cloud properties might affect the retrieval. The high emissivity of the cloud is essential to the retrieval process, as it provides an accurate cloud top temperature that largely eliminates background radiance differences. The cloud top pressure level in this study is fixed at the tropopause to simplify the retrieval process, though it is worth exam-

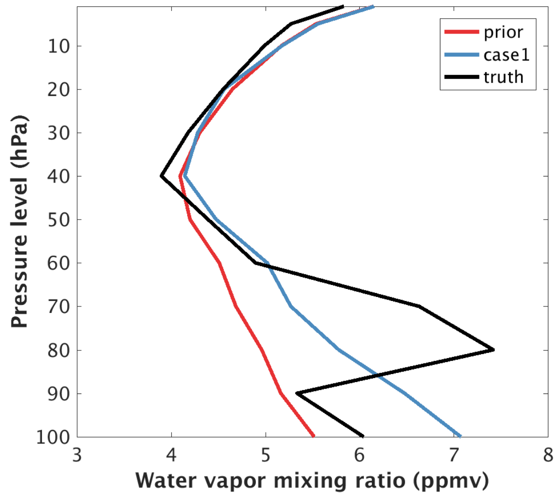

Figure 2.6: Cloud-assisted retrieval of water vapor for one moistened case. See Table 2.1 for case 1.

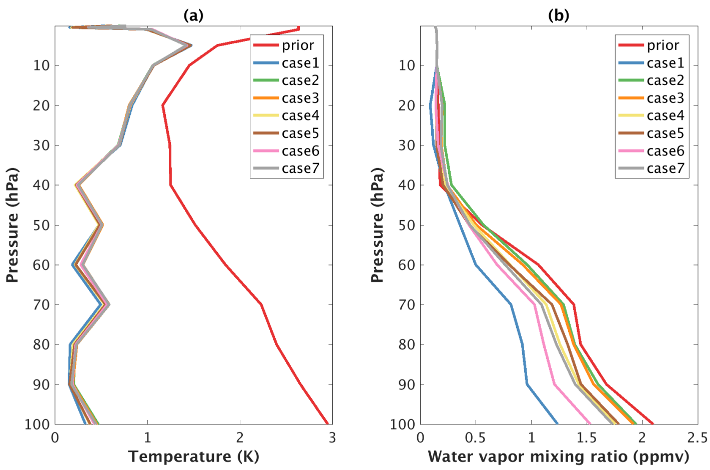

Figure 2.7: Root mean square error in cloud-assisted retrieval of (a) temperature, and (b) water vapor. See Table 2.1 for the instrument specifications in different cases.

ining how it can be retrieved and how cloud tops that overshoot the tropopause may affect retrieval results in future.

The forward model error might also add uncertainty to the result. First, the specification of frequency increment, spectral resolution, and slit function affect the performance of the radiative transfer model. The frequency increment is limited to 0.1 cm^{-1} by minimum bin size of MODTRAN, which means that Table 2.1 might have underestimated the performance of TES (which has a spectral sampling size at 0.0592 cm^{-1}). Furthermore, the retrieval only considers temperature and water vapor, other absorbers like CO_2, O_3 and CH_4 are assumed to have constant values. Variability in these gases may affect retrieval quality, although our tests prove that 20% perturbation of these gases throughout the stratosphere does not have a significant impact on the spectral signal of water vapor.

2.4 Application to AIRS

2.4.1 AIRS

AIRS has provided global measurements in a sun-synchronized orbit since 2002. The AIRS L1B radiance product contains 2378 infrared channels from 650 to 2665 cm^{-1}, with accuracy varying from 0.3 K to 0.5 K (against a 200 K reference temperature). It provides a Level 2 (L2) retrieval support product (version 6) for specific humidity on 100 pressure levels from 0.0161 hPa down to the surface, with a documented RMSE of 20% near surface [Susskind et al., 2011, Kahn et al., 2014], based on a cloud clearing method. However, this retrieval algorithm does not yield accurate water vapor retrieval in the upper troposphere and lower stratosphere (UTLS), for several reasons. First, because the cloud-clearing algorithm essentially depends on valid clear sky observations obtained from MODIS (Moderate Resolution Imaging Spectroradiometer), it does not work well when cloud uniformly obscures 3×3 FOVs. It results in a much larger RMSE with increased altitude, and dry biases over thick clouds [Wong et al., 2015]. Second, the average over 9 FOVs limits the ability to detect small-scale variation, although the latest single footprint retrieval does not have this requirement anymore [Irion et al., 2017]. Third, as discussed in previous section, the AIRS retrieval scheme shares the common problem with other nadir retrieval methods of UTLS water vapor performed in the clear sky condition, and is insensitive to the very low water vapor concentration (<10 ppmv) in the UTLS region [Fetzer et al., 2008, Gettelman et al., 2004, Read et al., 2007].

2.4.2 Aircraft

The in situ water vapor measurements used here are from the Harvard Water Vapor instrument which combines Harvard Lyman-α photo-fragment fluorescence instrument with a tunable diode laser direct absorption instrument [Anderson et al., 2012, Weinstock et al., 2009]. The maximum offest of this instrument is <0.2 ppmv. In this study, we take measurements during the summer of 2005. Flights from two days, June 17th and July 7th, are used here in that they have the cloud condition desired by our retrieval method. Both flights made continuous measurements of water vapor mixing ratio in the upper troposphere and lower stratosphere (see Fig. 2.8 and Fig. 2.9).

2.4.3 Retrieval test

In this section, we test the cloud-assisted retrieval method explained above using the AIRS L1B radiance over regions where elevated water vapor is detected by aircraft measurements. To perform this retrieval with AIRS L1B radiance, scenes over the same area as aircraft with at least 30 adjacent AIRS FOVs filled with deep convective clouds (DCCs) are selected. To identify DCCs, a threshold based on positive brightness temperature difference between a water vapor absorption channel (BT_{1419}) and an IR window channel (BT_{1231}) is used [Aumann and Ruzmaikin, 2013]. A positive brightness temperature difference, BT_{1419}-BT_{1231}, is induced by warmer stratospheric water vapor emission against the cold cloud top so that a large positive difference indicates a near tropopause cloud top and possible elevated stratospheric water vapor concentration. The selection of channel BT_{1419} is based on its strong water vapor absorption and a relatively low noise-to-signal ratio.

The DCCs are assumed to be a blackbody. Under this assumption, cloud top temperature can be inferred from the brightness temperature in the IR window channel. Based on this, cloud top pressure is then estimated from an *a priori* temperature profile (the AIRS L2 temperature retrieval), varying from 90 to 180 hPa. Only the above cloud part is retrieved, and latter used in evaluation. The covariance matrix S_a is derived using the same training dataset described in the simulation experiments (see section 2.2). To start the iteration, we use the AIRS L2 temperature and water vapor retrieval at each FOVs as the first guess .

Fig. 2.8 shows the aircraft track from 18:00 to 22:40 UTC on June 17th. The aircraft flew from south to north, and then returned along the same track. It crossed the tropopause five times during the measurement period. During the flight, elevated water vapor was observed with mixing ratios up to 8 ppmv at a level around 80 hPa for a roughly 10 hPa vertical interval. Around twelve hours earlier, AIRS detected an area of DCCs to the east of flight track, as shown in Fig. 2.8 with solid squares, among which colored squares denotes a positive BT_{1419}-BT_{1231}. These samples are collected for later retrieval.

In Fig. 2.8 (d), retrieval results for water vapor from 150 hPa to 50 hPa are presented. We calculated the probability density function (PDF) at 2 ppmv spaced intervals at every 20 hPa vertical level. Compared to AIRS L2 retrieval, the water vapor retrieved here has a much larger variability. Around 40$\%$ of the profiles indicate water vapor elevation at levels between 50 to 90 hPa, which agrees with aircraft measurements. The narrow vertical layer with high water vapor concentrations at around 75 hPa depicted by the aircraft data is not evident in the retrieval. This is within our expectation as previous simulation experiments suggest limited vertical resolution in the retrieval. On the other hand, the aircraft measurements have limited spatial coverage such that the narrowness of the layer may not be real.

On July 7th, the aircraft detected very high water vapor mixing ratios, up to 18 ppmv at 117 hPa and an elevated water vapor layer over 30 hPa thick below 145 hPa. There are two concurrent AIRS scenes containing DCCs: one group of FOVs in the west, upwind of the flight track, around 6 hours earlier; another group of FOVs parallel to the flight track, about 4 hours later. Although these scenes only contain 49 FOVs with DCCs, the aircraft measurements (Fig. 2.9 (c)) shows a clear distinction between unmoistened and moistened samples at a lower level. Interestingly, the mean of retrieved water vapor suggests a different vertical distribution of water vapor compared to the case of June 17th, which corresponds to the in situ measured enhancement up to 35 ppmv around 120 hPa very well.

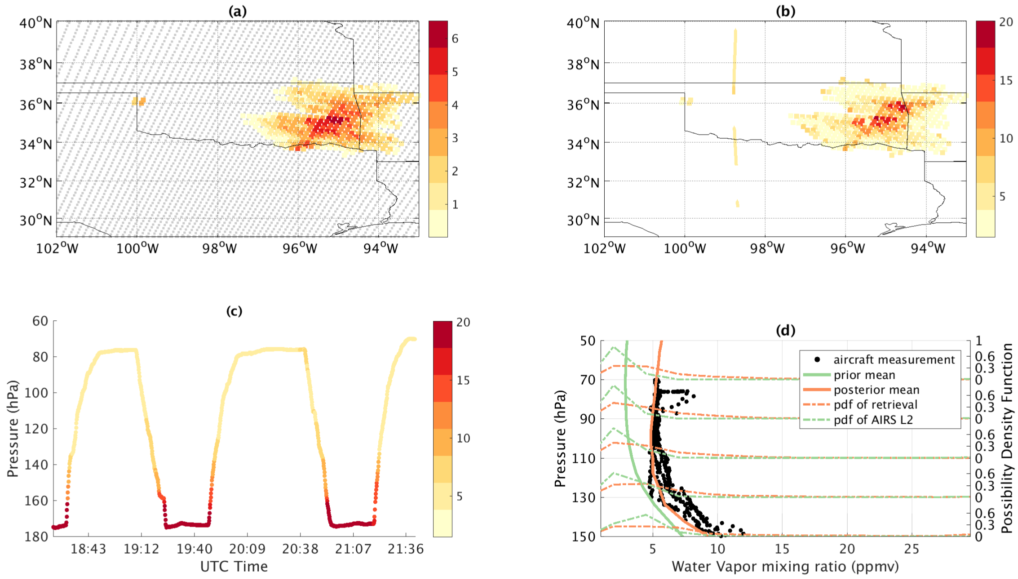

Figure 2.8: Retrieval of June 17th, 2005. (a) Brightness temperature difference (BT_{1419}-BT_{1231}) in the AIRS L1B measurements. (b) Water vapor volume mixing ratio at 78 hPa retrieved from the AIRS L1B measurements and that between 75.5 and 80.5 hPa measured by the aircraft. (c) Aircraft altitude time series, color-coded by measured water vapor mixing ratio. (d) Vertical distribution of retrieved water vapor mixing ratio (mean in red solid line and PDFs of each 20 hPa vertical interval in red dashed line), compared to the aircraft measurements (black dots) and the prior guess (green). Units are mixing ratio in ppmv in all plots.

Our tests here indicate that nadir-view hyper-spectral radiance measurements, such as the AIRS L1B data, contain information for detecting elevated water vapor concentration in the UTLS region. Although the current retrieval methods have not fully used such information, an improved method can. In both case studies here, the cloud-assisted retrieval method detects moistening in the lower stratosphere, with the posterior mean profile showing better agreement with collocated airborne measurements than the AIRS L2 retrieval. Both cases strongly support this method regarding its ability to detect stratospheric water vapor elevation, and to improve the mean climatology of a region with water vapor mixing ratios lower than the 10-25 ppmv sensitivity limit of the AIRS instrument that have been suggested in previous studies [Fetzer et al., 2008, Gettelman et al., 2004, Read et al., 2007].

A few caveats should be noted regarding the retrieval though. Firstly, as discussed in section 2.2, the optimal estimation-based retrieval algorithm depends on both radiance measurements and prior information - as a rule of thumb, the magnitudes of the covariance matrixes S_a and S_e decide which dominates. Because the instrument (AIRS) noise level is relatively high, the prior information, including both the first guess and the covariance matrix S_a, is expected to influence the retrieval strongly. S_a is important in that it controls the covariance of the retrieved state vector. In the retrieval above, we have used a special way to construct the covariance matrix (see section 2.2). If the artificially moistened profiles are instead used to construct the off-diagonal element of S_a, the DFS of the retrieval will increase by 0.1 and consequently isolated layers with elevated water vapor concentration will be rendered by the retrieval method. In fact, when the retrieval is done this way, we find in the retrieval results narrow high water vapor concentration layers at upper levels, at around 50 hPa on June 17th and at around 50 and 120 hPa on July 7th. However, there was no aircraft measurement at the higher levels to validate such a retrieved water vapor pattern. This is a situation worth further investigating in future observational campaigns.

Secondly, the retrieval is limited by the present instrumentation. As the cloud top position is derived using the AIRS L2 temperature retrieval, the uncertainty in the AIRS L2 retrieval thus affects the results. The cloud top temperature determined in both cases is higher than the minimum temperature at the tropopause (e.g., 80 hPa) but corresponds to the temperature at 120 and 60 hPa. Because the 60 hPa level is 3 km above the tropopause and unlikely reached by the deep convection, the cloud top is thus placed at the lower level.

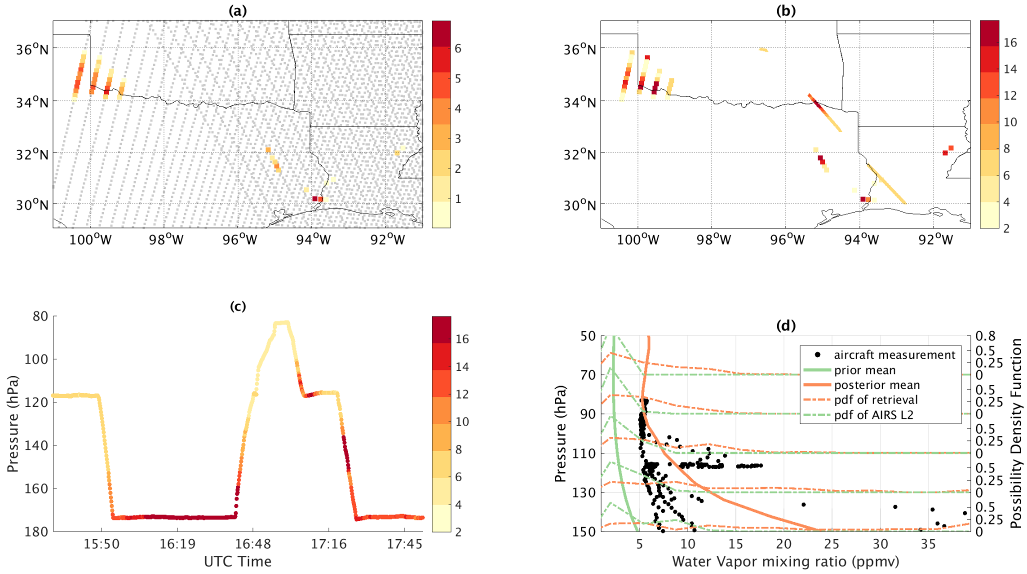

Figure 2.9: Retrieval of July 7th, 2005. As in Fig. 8, except that in (b) retrieval at 117.7 hPa and aircraft measurements within 115-120 hPa are shown.

In this regard, the uncertainty in cloud top position can be greatly reduced if we implement cloud top pressure data from CloudSat [Stephens et al., 2002] or CALIPSO [Cloud-Aerosol Lidar and Infrared Pathfinder Satellite Observation; Winker et al., 2003] .

In addition, the non-monotonic temperature structure induces ambiguity in the water vapor retrieval. Under this condition, had there been water vapor channels with narrow weighting functions peaking at different levels around the tropopause, atmospheric moistening below and above the tropopause can be distinguished in theory by their brightness temperature signals (anomalies of different signs). However, the AIRS spectral coverage and resolution are such that there is no water vapor channel with a weighting function that peaks above 100 hPa (the highest peak is around 150hPa). As a result, the retrieved enhancement of water vapor can only be widespread in the vertical. From the simulation tests in Section 2.2, it is expected that the retrieval could benefit from an instrument with FIR coverage (to utilize the stronger rotational lines of water vapor) or higher spectral resolution (to enhance the signals in the vibration-rotational band of water vapor).

2.5 Conclusions

In this study, we examine the feasibility of retrieving stratospheric water vapor using nadir view satellite infrared spectral measurements and apply this method to two case studies on the AIRS L1B radiance product. Our focus is on the detectability of small-scale water vapor variability, for instance, caused by convective moistening, leveraging on the relatively small footprint sizes of the nadir view instruments. The feasibility of the retrieval is assessed using simulation experiments to model a variety of instrument settings (Table 2.1). A hypothetical case with ideal instrument setting demonstrates the theoretical limits of this retrieval, while a suite of additional cases shows the performance that can be expected from current satellite instruments, as well as improvements that can be achieved under different instrumentation conditions. Had an ideal instrument with both FIR and MIR spectral coverage (200-2000 cm^{-1}), high spectral resolution ($0.1\ \mathrm{cm}^{-1}$) and low noise level ($0.25 \times 10^{-8}\ \mathrm{W}/(\mathrm{cm}^2\mathrm{srcm}^{-1})$) been used, the measurements would have a DFS of nearly 3 for lower stratospheric (40-100 hPa) water vapor (see case 1 in Table 2.1), indicating the high potential of this retrieval technique. The FIR coverage proposed for future missions, e.g., the Climate Absolute Radiance and Refractivity Observatory (CLARREO, https://clarreo.larc.nasa.gov) would be especially beneficial in that the signal strength in the water vapor rotational band is an order of magnitude larger than in the vibration-rotational band (see Fig. 2.5). Advanced detector with lower noise levels would also greatly enhance the retrieval performance. In this regard, a strategy that allows increased stare time of the target (e.g., on geostationary orbits or high-altitude drones) would be beneficial.

Interestingly, we find the performance of lower stratospheric water vapor retrievals can be considerably enhanced with the presence of a tropopause cloud layer. This is because an opaque cloud layer at this level effectively blocks the upwelling radiation from below the tropopause, which not only eliminates the uncertainty arising from the upper tropospheric water vapor variability due to the smoothing effect related to averaging kernel (Fig. 4) but also the degeneracy caused by the non-monotonic vertical temperature variations about the tropopause level. With the assistance of such a cloud layer, the retrieval can substantially reduce the uncertainty in the total amount of the lower stratospheric water vapor (see the CIWV column in Table 1). This indicates the feasibility of detecting above thick cumulonimbus or anvil clouds had the convective moistening of the lower stratosphere occurred.

We have tested the cloud-assisted retrieval technique using the infrared hyperspectral measurements of AIRS. The retrieval detects small-scale water vapor variability that is observed by in-situ aircraft measurements but not shown by the current AIRS L2 retrieval. The detected lower stratospheric moistening is in qualitatively good agreement with collocated aircraft data. Although the tests here imply that some aspects of the retrieval such as the vertical resolution are limited by the present instruments, the results indicate the potential of detecting highly elevated water vapor concentrations near or above the tropopause by using the nadir instruments. Given the climatic importance of atmospheric water vapor in the upper troposphere and lower stratosphere and the considerable uncertainty of its distribution in this region in the present datasets, future research is warranted to further develop and apply the retrieval technique proposed here. Besides AIRS, the technique can be applied to other nadir-view infrared hyperspectrometers, such as IASI (Infrared Atmospheric Sounding Interferometer) and CrIS (Cross-track Infrared Sounder), on polar orbiters. Similar instruments on geostationary satellites, such as GIIRS (Geosynchronous Interferometric Infrared Sounder) on Fengyun-4, may be especially suitable for this application because of their ability to continually monitor overshooting targets.

3

A simulation experiment-based assessment of retrievals of above-cloud temperature and water vapor using hyperspectral infrared sounder

Measuring atmospheric conditions above convective storms from space-borne instruments is challenging. The operational retrieval framework of current hyperspectral infrared sounders adopts a cloud-clearing scheme that is unreliable in overcast conditions. To overcome this issue, previous studies have developed an optimal estimation method that retrieves temperature and humidity above high, thick clouds, assuming a slab of cloud. In this study, we find that cloud properties near the top of convective clouds lead to non-negligible spectral uncertainties in simulated infrared radiances. These uncertainties cannot be fully eliminated by the slab-cloud assumption. To address this problem, a synergistic retrieval method is developed. This method retrieves temperature, water vapor, and cloud properties simultaneously by incorporating observations from active sensors in synergy with infrared radiances. A simulation experiment is conducted to evaluate the performance of different retrieval strategies via hypothetical observations from AIRS and DARDAR-Cloud products. In this simulation experiment, we simulate infrared radiance spectra from convective storms through the

combination of a numerical weather prediction (NWP) model and a radiative transfer model. The simulation experiment shows that the synergistic method is advantageous for strong retrieval sensitivity to temperature and IWC near the cloud top. By incorporating temperature and humidity profiles from reanalysis products, the synergistic method reduces root-mean-square errors in temperature and column integrated water vapor by more than half. It can also improve ice water content and effective radius retrievals with information from active sensors. Our results suggest that existing infrared hyperspectral sounders can detect the spatial distribution of temperature and humidity anomalies above convective storms.

3.1 Introduction

Water vapor in the upper-troposphere and lower-stratosphere (UTLS) plays an essential role in the Earth's climate system due to its important radiative [Huang et al., 2010, Dessler et al., 2013] and chemical effects [Shindell, 2001, Kirk-Davidoff et al., 1999, Anderson et al., 2012].

Our understanding of UTLS water vapor has long been informed by accurate in-situ observations carried out during aircraft and balloon campaigns. Long-term records provided by balloon-borne observations have suggested a decadal increase in stratospheric water vapor [Oltmans et al., 2000, Rosenlof et al., 2001, Hurst et al., 2011] but a decadal cooling in tropical tropopause temperature over the same period [Rosenlof et al., 2001, Randel et al., 2004]. These contradictory trends between water vapor and temperature are not well reproduced by reanalysis products, however the key processes at play are still under debate. This increase in UTLS water vapor, if true, may accelerate the decadal rate of surface warming through its impact on thermal radiation [Solomon et al., 2010]. While balloon campaigns suggest this crucial long-term change in UTLS water vapor, aircraft campaigns reveal that UTLS water vapor can be highly variable under the influence of deep convection. By sampling plumes from convective detrainment, these campaigns have found that overshooting deep convection can increase the UTLS water vapor by injecting moist plumes or ice particles that sublimate in a warmer environment [e.g., Corti et al., 2008, Schiller et al., 2009, Anderson et al., 2012, Sun and Huang, 2015, Smith et al., 2017]. Despite substantial evidence of convective hydration, it has been argued that the overall impact of convection on the global UTLS water vapor budget might be negligible [e.g., Ueyama et al., 2018, Schoeberl et al., 2019, Randel and Park, 2019].

Therefore, long-term, global observations of UTLS water vapor, especially above convective storms, are essential. However, the operational global radiosonde network does not perform well in cold and low-pressure environments such as the UTLS [Kley, 2000]. Moreover, while satellite observational products have been extensively used to investigate the spatial and temporal variability of UTLS water vapor [Sun and Huang, 2015, Randel and Park, 2019, Yu et al., 2020, Wang and Jiang, 2019, Jiang et al., 2020], these products have some limitations. Limb-viewing and solar occultation instruments are sensitive to the UTLS region. Nevertheless, they are not suitable for detecting the small-scale variability above convective storms because the horizontal sampling footprints of these instruments are larger than 100 km. Furthermore, contamination by convective clouds leads to higher uncertainty in the current product of microwave sounders [such as MLSv4.2, Livesey et al., 2017] due to strong scattering. Moreover, limited by the occurrence of solar occultation, instruments using this technique do not provide sufficient sampling to study convective impacts.

Meanwhile, the current hyperspectral sounding framework of NOAA and NASA adopts a cloud-clearing scheme [Susskind et al., 2003, Gambacorta et al., 2014]. This scheme infers the radiance of clear scenes from adjacent 3×3 instrument fields-of-view (FOVs) with varying cloud amounts, assuming the same temperature and atmospheric absorber (including water vapor) fields in all FOV footprints ($\sim$ 13.5 km). Consequently, such a cloud-clearing scheme would fail in overcast cloud conditions (uniform cloud amounts in adjacent footprints) or when thermodynamic properties vary drastically among adjacent footprints. Following thi framework, current retrieval products from hyperspectral infrared sounders, including AIRS [the Atmospheric Infrared Sounder, Chahine et al., 2006], IASI [Infrared Atmospheric Sounding Interferometer, Blumstein et al., 2004], and CrIS [Cross-track Infrared Sounder, Bloom, 2001], are not reliable above convective storms.

Recently, researchers have demonstrated the feasibility of performing single-footprint retrievals in cloudy-sky conditions from AIRS using an optimal estimation (OE) scheme [DeSouza-Machado et al., 2018, Irion et al., 2018, Feng and Huang, 2018]. Using the same instrument, such single-footprint retrievals improve the spatial resolution from 40.5 km under the cloud-clearing scheme to 13.5 km. In these studies, DeSouza-Machado et al. [2018] used the *a priori* cloud state from a numerical weather prediction model (NWP) and then adjusted the cloud state to match the observed brightness temperature of an infrared window channel. Irion et al. [2018] retrieved cloud optical depth, effective radius, and cloud-top temperature, using the *a priori* from collocated MODIS observations. While DeSouza-Machado et al. [2018] and Irion et al. [2018] discussed the implementation of all-sky, single-footprint OE scheme in general, Chapter 2 focused especially on optically thick cloud conditions, for which they conducted a comprehensive information content analysis. They showed that the existing hyperspectral infrared sounders contain a substantial degrees of freedom for signal (DFS, a higher DFS indicates a higher vertical resolution) in UTLS temperature ($\sim$5) and water vapor ($\sim$1). They also found that the presence of a thick cloud in the upper-troposphere increases the DFS compared to clear-sky conditions. By validating the retrieval using in-situ observations carried by aircraft campaigns, Chapter 2 elucidated that it is possible to retrieve both hydration and dehydration anomalies in the UTLS from current infrared hyperspectral sounders. In the case of optically thick clouds, e.g., deep convective clouds, these studies [DeSouza-Machado et al., 2018, Irion et al., 2018, Feng and Huang, 2018] similarly represent the cloud as a slab (thick and uniform layer) of ice clouds with fixed microphysics properties, based on *a priori* cloud states inferred from brightness temperature of an infrared window channel, NWP, or coincident passive cloud instrument [i.e., MODIS, Moderate Resolution Imaging Spectroradiometer Platnick et al., 2003]. Retrieval methods following this cloud assumption are referred to as slab-cloud methods hereinafter.

However, neglecting variability in cloud mass and microphysical properties leads to large uncertainty in the thermal emission of the cloud, which greatly contributes to observed radiances at TOA. Yang et al. [2013] showed that the scattering and absorption properties of ice clouds across the infrared spectra are greatly impacted by the size and shape of ice particles. Furthermore, deep convective clouds are typically associated with large temperature perturbations near the cloud top and drastic temperature decreases with altitude [Biondi et al., 2012]. Considering an anomalous temperature field, inferring cloud top position from the brightness temperature of an infrared window channel, as in previous studies, can be biased [Sherwood et al., 2004]. When the temperature lapse rate is large, the vertical distribution of ice content can determine the cloud thermal emission. Therefore, it is necessary to assess, and constrain, the impacts of these factors on retrieval accuracy.

The cloud uncertainties can be reduced by combining collocated observations from active sensors onboard the same satellite constellation. The A-Train satellite constellation provides a unique collocation between an orbital hyperspectral infrared sounder (i.e., AIRS) and active remote-sensing instruments, including the cloud profiling radar aboard CloudSat [Stephens et al., 2002] and CALIOP (Cloud-Aerosol Lidar with Orthogonal Polarization) aboard CALIPSO [Cloud-Aerosol Lidar and Infrared Pathfinder Satellite Observation, Winker et al., 2003]. Along the A-Train orbit track, these instruments passed over near-coincident locations within 2 minutes of each other (before the year 2015). The nearest lidar (90 $\mathrm{m} \times 90\ \mathrm{m}$) and CPR footprints (2.5 $\mathrm{km} \times 1.4\ \mathrm{km}$) were typically located around 5 km from the center of the AIRS footprints (13.5 $\mathrm{km} \times 13.5\ \mathrm{km}$), well within the AIRS FOVs. DARDAR-Cloud [Delanoë and Hogan, 2008, 2010] is a joint product that combines radar reflectivity measurements from CPR and lidar attenuated backscatter ratio from CALIOP to provide ice water content (IWC) and effective radius profiles at each CPR footprint. Compared to passive instruments, this joint product is more sensitive to the vertical ice distribution near the cloud top, which can be essential to the thermal emission of the cloud. Here we aim to develop an optimal estimation method to retrieve temperature, water vapor, ice water content, and effective radius simultaneously by incorporating active cloud remote sensing products and infrared hyperspectra, using the DARDAR-Cloud product and AIRS L1B observations to construct an example. A retrieval method that incorporates such collocated cloud products is referred to as a synergistic method.

In this paper, we quantify the uncertainty in infrared spectral radiances induced by cloud optical properties. The performance of retrieval strategies following the slab-cloud and synergistic methods is then evaluated following a simulation experiment, assuming an implementation based on the AIRS L1B and DARDAR-Cloud products. Due to the lack of observations, a simulation experiment that simulates observational signals from realistic temperature, humidity, and cloud fields above deep convective events is necessary. Section 3.2 describes the main components of this simulation experiment. We then implement different retrieval strategies, as formulated in Section 3.2.3, to retrieve from synthetic observations. The results are evaluated in Section 3.3 by comparing retrievals to the prescribed truth. The application of the improved synergistic retrieval scheme to existing instruments is discussed in Section 3.4.

3.2 Method

The simulation experiment in this study consists of the following components:

4. a cloud-resolving NWP model, which is used to provide the 'Truth' of atmospheric conditions during a tropical cyclone event and to construct the $a\ priori$ and test sets, as described in Section 3.2.1;
5. a radiative transfer model, which is used to generate synthetic observations with the AIRS instrument specifications and as the forward model in the retrieval, as described in Section 3.2.2;
6. retrieval algorithms as explained in Section 3.2.3; and
7. comparisons between the retrieved quantities and the NWP-generated truth in Section 3.3.

A tropical cyclone event is simulated because it generates a vast convective cloud that covers a large spatial domain for contrasting the above-storm temperature and humidity field. In the framework of this simulation experiment, we neglect the complexity in instrument scan geometry by assuming a nadir instrument viewing angle, uniform atmospheric conditions within one footprint, and availability of coincident cloud products for every sample. In reality, the scanning angle of AIRS footprints, which have the nearest CloudSat footprints within 6.5 km from the center, is around 16 degrees off the nadir.

3.2.1 Numerical weather prediction model

In this study, we use the Global Environmental Multiscale model (GEM) of Environment and Climate Change Canada [hereafter ECCC, Côté et al., 1998, Girard et al., 2014] to provide a detailed and realistic representation of storm-impacted atmospheric and cloud profiles, following the study of Qu et al. [2020]. The GEM model is formulated with non-hydrostatic primitive equations with a terrain-following hybrid vertical grid. It can be run as a global model or a limited-area model and is capable of one-way self-nesting. For the experiments conducted here, three self-nested domains are used with areas of 3300×3300, 2000×2000, and 1024×1024 km^2 and horizontal grid-spacings of 10, 2.5, and 1 km, respectively, centered at 141°E, 16°N. All simulations use 67 vertical levels, with vertical grid-spacing $\Delta \mathrm{z} \sim 250$ m in the UTLS region and a model top at 13.5 hPa (29.1 km). The simulation is initialized with conditions from the ECCC global atmospheric analysis at 00:00 UTC 16 May 2015. It runs for 24 hours until 00:00 UTC on 17 May 2015. Model outputs at 1 km horizontal grid-spacing are saved every 10 minutes and used in the simulation experiment.

For the two high-resolution simulations with 2.5-km and 1-km horizontal grid-spacing, the double-moment version of the bulk cloud microphysics scheme of Milbrandt and Yau (2010a, b; hereinafter referred to as MY2) is used. This scheme predicts the mass and number mixing ratio for each of six hydrometeors including non-precipitating liquid droplets, ice crystals, rain, snow, graupel, and hail. Condensation (ice nucleation) is formed only upon reaching grid-scale supersaturation with respect to liquid (ice). In addition to the MY2 scheme, the planetary boundary-layer scheme [Bélair et al., 2005] and the shallow convection scheme [Bélair et al., 2005] can also produce cumulus, stratocumulus, and other low-level clouds, which are of less relevance to our UTLS-centric simulation experiment.

A snapshot from the 1-km resolution GEM simulation, 410 minutes after the initial time step, is used for the radiance simulation because a mature storm at this time has generated abundant convective clouds, which our retrieval approach targets. Figure 3.1 shows the atmospheric conditions at this time step, including the distributions of temperature and water vapor at 81 hPa, at which level the variance is largest. To mimic the satellite infrared image, we show the distribution of the brightness temperature in a window channel at 1231 cm^{-1} (8.1 μm, BT_{1231}). A cold BT_{1231} suggests a deep convective cloud (DCC) that extends to the tropopause level. Overshooting deep convective clouds (OT-DCC) are outlined in Figure 3.1 (a) with solid red curves. These OT-DCC are defined as continuous, precipitating clouds that fully cover vertical ranges from near-ground to 380 K potential temperature. Overshooting DCCs are often identified from satellite infrared images based on a warmer BT in a water vapor channel (BT_{1419} cm^{-1}) relative to BT_{1231} , which can be attributed to water vapor emission above the cold point [Aumann and Ruzmaikin, 2013]. The BT-based criterion is used to select retrieval samples, mimicking the scenario of using infrared radiance measurements alone to identify overshooting DCCs, as performed in Chapter 2. Using the BT-based criterion, 9941 retrieval samples are identified, with their locations marked in Figure 3.1. Among these samples, 100 profiles are randomly selected to construct a test set. The size of the samples is verified to meet the convergence requirement of the statistical evaluation conducted in Section 3.3. The rest of the simulated profiles, regardless of cloud conditions, numbering O(10^6), are used to construct an $a\ priori$ dataset to define the prior knowledge used in the retrieval in Section 3.2.3.

3.2.2 Radiative transfer model

This study uses the MODerate spectral resolution TRANsmittance, version 6.0 (MODTRAN 6.0) [Berk et al., 2014] to simulate the infrared radiances observed by satellite. MODTRAN 6.0 provides a line-by-line (LBL) algorithm that performs monochromatic calculations at the center of 0.001 cm^{-1} sub-bins. Within each 0.2 cm^{-1} spectral region, this method explicitly sums contributions from line centers while precomputing contributions from line tails. This algorithm has been validated against a benchmark radiation model, LBLRTM, showing less than 0.005 differences in atmospheric transmittance through most of the spectrum [Berk and Hawes, 2017]. MODTRAN 6.0 accounts for both absorptive and scattering media in the atmosphere by implementing a spherical refractive geometry package and the DISORT discrete ordinate model to solve the radiative transfer equation [Berk and Hawes, 2017].

In this study, we use MODTRAN 6.0 to simulate the all-sky radiances with user-defined atmospheric profiles. 80 fixed atmospheric pressure levels are used. Temperature, water vapor, and ice cloud (IWC) profiles from GEM simulations at 67 layers are input into the model. Above the GEM model top (13.5 hPa), the values from a standard tropical profile [McClatchey, 1972] are placed between 13.5 and 0.1 hPa. Other trace gases are fixed at a tropical mean value.

User-defined cloud extinction and absorption coefficients are added to the model, based on the cloud optical library of Yang et al. [2013]. This cloud optical library provides a look-up table for the scattering, absorption, and polarization properties of ice particles of different habit shapes, roughness, and sizes. We parametrize the particle size distribution follow-

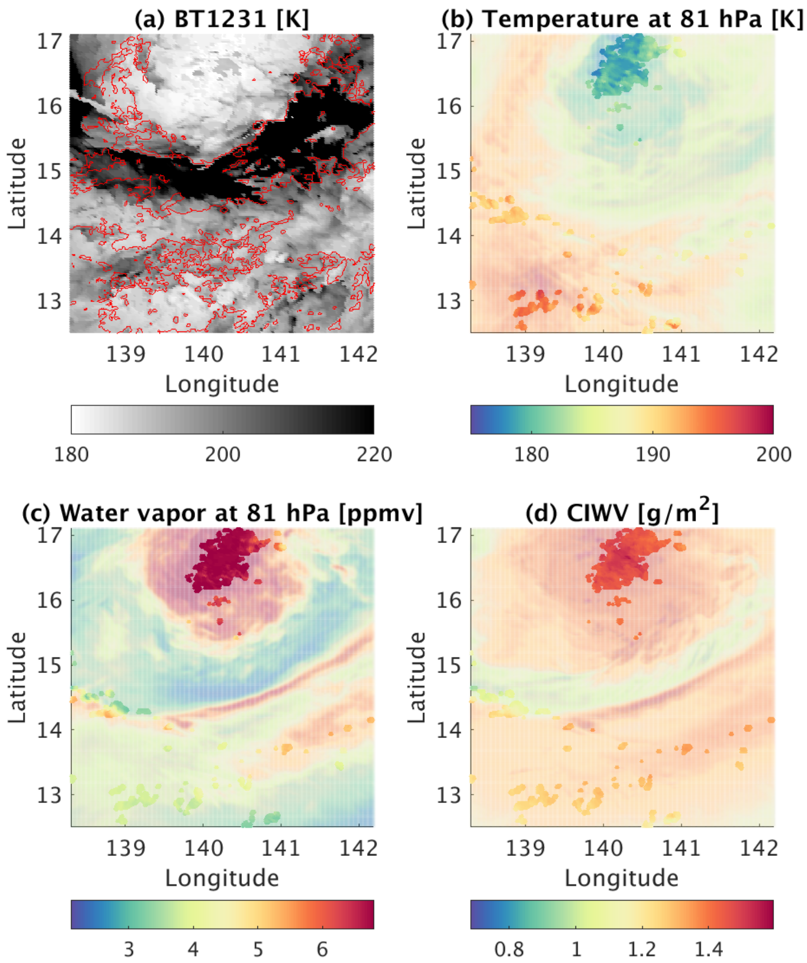

Figure 3.1: GEM-simulated atmospheric conditions used as the "Truth" in the simulation experiment. (a) Brightness temperature $[\mathrm{K}]$ at 1231 cm^{-1}. The red curve outlines the overshooting deep convective clouds. (b) Temperature $[\mathrm{K}]$ at 81 hPa. (c) Water vapor volume mixing ratio $[\mathrm{ppmv}]$ at 81 hPa. (d) Column integrated water vapor (CIWV) from 110 to 70 hPa. Solid color-coded dots mark the overshooting deep convective clouds sampled via BT-based criterion from which the test set is sampled to conduct the retrievals. Partially transparent colors show the rest of the simulated fields. The variable fields are taken at 410 minutes after the initial time step.

ing microphysical data obtained from in-situ observations at temperature lower than -60 ^{o}C [Heymsfield et al., 2013, Baum et al., 2014]. Following Baum et al. [2011] Appendix A-B, the mean extinction coefficients, mean absorption coefficients, and mean asymmetry factors over the parametrized particle size distribution are obtained at individual wavelengths, for effective radii range from 1 to 100 $\mu\mathrm{m}$. These optical properties are then supplied to the radiative transfer calculations for a specified effective radius. In the context of this paper, extinction coefficients, single-scattering albedo, and asymmetry factor are assumed to be the same for ice clouds at different vertical ranges (i.e., neglect the vertical variation in effective radius). The optical depth of ice clouds in the DCC samples exceeds 100, which completely attenuates emission from liquid clouds. Liquid clouds are therefore neglected.

The instrument specifications of AIRS are used in the retrieval framework of this simulation experiment. This instrument has 2378 channels from 650 to 2665 cm^{-1}. The radiometric noise of this instrument is obtained from the AIRS L1B product, which corresponds to a noise equivalent temperature difference (NEdT) around 0.3 K (at 250 K). This NEdT increases to around 0.5 K at 200 K reference temperature. Based on the radiometric quality of each channel, 1109 channels are selected. This rigorous channel selection also excludes O3 absorption channels (980-1140 cm^{-1}), CH4 absorption channels (1255-1355 cm^{-1}), and shortwave infrared channels (2400-2800 cm^{-1}). Adopting the AIRS spectral response function, synthetic radiances are generated using MODTRAN 6.0 with temperature, water vapor, and ice water content profiles from the test set described in Section 3.2.1. The effective radius of the test set is sampled from DARDAR-Cloud observations described in Section 3.2.2 and depicted in Figure 3.2. Spectrally uncorrelated noise is then generated and added to the synthetic radiance spectra. The noise at each channel follows the Gaussian distribution with its mean at the radiometric noise of the AIRS instrument. These infrared radiance spectra are used as synthetic observations in the simulation experiment.

3.2.2.1 Cloud induced uncertainties

In the following, we evaluate the variation in infrared spectra that results from variability in 1) the vertical distribution of ice mass, and 2) the effective radius. The surface roughness of ice particles is neglected as it mainly affects the scattering angle [Yang et al., 2013], which plays a minor role in the infrared channels. We focus on tropical cyclone events for their relevance to the simulation experiment.

To gain knowledge of cloud ice particles and their impacts on the infrared radiance spectrum and also to prescribe relevant information in the UTLS retrieval (see Section 3.2.3), we use the DARDAR-Cloud product to form a dataset of cyclone overpasses. The CloudSat 2D-TC product [Tourville et al., 2015] is used to identify the moment when A-Train satellites pass over tropical cyclones in the western part of the Pacific from 2006 to 2016. From these overpasses, we select DARDAR footprints that are within 1000 km of the cyclone center locations. Based on the CloudSat-CLDCLASS product, 98293 of these footprints contain OT-DCCs that penetrate beyond 16 km in altitude. Each profile consists of IWC and effective radius at a vertical resolution of 60 m.

First, using the identified OT-DCC profiles from DARDAR-Cloud, we calculate the probability distribution function of the effective radius of ice particles at the topmost cloud layer. Fig. 3.2 shows that the ice particles are typically small, with an average effective radius of 21.5 $\mu\mathrm{m}$ (Re_0) and the 1st and 99th percentiles of 13.3 and 39.7 $\mu\mathrm{m}$ respectively. According to Heymsfield [1986] and Baum et al. [2011], over 80% of the small ice particles at tropical high altitudes are solid columns. Hence, we consider the ice particles to be solid columns with conserved ice mass but varying effective radii in the following

Then, 100 profiles are selected from OT-DCC samples to evaluate the effects of varying IWC and effective radii on the infrared radiance spectra at 0.1 cm^{-1} resolution, without applying an instrument-specific spectral response function. First, we calculate the upwelling infrared radiance, $R(Re, IWC)$, using the IWC profile (IWC), and effective radius (Re) of the topmost layer, for every sample. The mean temperature (t_0) and water vapor (q_0) profiles of the NWP simulation domain (Fig. 3.1) are used in the radiative transfer calculations. Next, the infrared radiances with mean effective radius (Re_0) or IWC profile (IWC_0) are calculated, denoted as $R(Re0, IWC)$ and $R(Re, IWC_0)$, respectively. The spectral response caused by the variation in effective radius is then represented by the mean (blue curve) and the standard deviation (STD, grey shaded area) of the equivalent brightness temperature of $R(Re, IWC_0)$, as shown in Fig. 3.3 (a). Using a mean effective radius leads to a mean absolute error (MAE), measured by the arithmetic average of the absolute errors between $R(Re, IWC)$ and $R(Re_0, IWC)$, which is shown as a red curve in Fig. 3.3 (a). Similar results are shown in Fig. 3.3 (b) for IWC.

In Fig.3.3 (a,b), the mean spectrum of OT-DCCs shows cold and relatively uniform brightness temperatures in the window and weak absorption channels that largely describe the emission from the cloud top. While varying effective radii and IWC have a weak effect on the strong absorption channels, they greatly impact the cloud emission, thus leading to large radiance variations in the window and weak absorption channels. As a result, the two MAE spectra are similar. The MAE due to a varying effective radius is within 1 K and the MAE due to a varying IWC profile is around 4 K. Hence, the infrared radiances are more sensitive to the IWC than the effective radius.

The normalized MAE spectra are shown in Fig.3.3 (c) to examine whether the effective radius produces a distinguishable signature against IWC. Despite the overall similarity, effective radius affects the spectrally dependent attenuation coefficients, leading to a tilted pattern across the infrared spectra, while the MAE due to IWC is relatively uniform across the infrared window. Therefore, it is possible to distinguish the radiative signals of effective radius from those of IWC with a mid-infrared coverage characteristic of existing instruments. Interestingly, the difference in the normalized MAE spectra is more apparent at smaller wavenumbers, suggesting that far-infrared channels, e.g., from future instruments, such as FORUM [Palchetti et al., 2020] and TICFIRE [Blanchet et al., 2011], may be advantageous for the UTLS retrieval, which is beyond the scope of this simulation experiment but warrants future investigation.

Furthermore, we quantify the spectral uncertainties caused by the slab-cloud assumption in Fig. 3.3 (d). For each radiance spectrum, $R(Re, IWC)$, the brightness temperature of a window channel at 1231 cm^{-1}, BT_{1231}, is calculated. Next, following the slab-cloud assumption used by Chapter 2, we place a slab of cloud at the vertical layer where the atmospheric temperature differs the least from BT_{1231}. This 500-m thick slab-cloud has uniform IWC of 1.5 $\mathrm{g/m^3}$ and an effective radius of 21.5 $\mu\mathrm{m}$. The temperature of this vertical layer is adjusted to BT_{1231}. With this prescribed cloud layer, radiances are calculated again for each profile, denoted as $R(Re_0, slab)$. The BT_{1231} values of $R(Re, IWC)$ and $R(Re_0, slab)$ are identical. Consequently, the difference between $R(Re, IWC)$ and $R(Re_0, slab)$ in other channels highlights the radiance uncertainty due to the slab-cloud assumption. The mean bias and STD of the radiance difference, as well as the root-mean-square (RMSE), are shown in Fig. 3.3 (d).

Fig. 3.3 (d) reveals that the slab-cloud assumption cannot fully account for the spectral variations of cloud emission. The assumption leads to a spectrally tilted mean radiance bias as shown by the blue curve in Fig. 3.3 (d). We note that this tilted pattern is related to the spectrally dependent extinction efficiency, which is affected by effective radius, so that the radiances at different wavenumbers are contributed by cloud emission at varying heights, which is in turn affected by the vertical distribution of ice mass. Therefore, the clear-cut cloud boundary in the slab-cloud and a constant effective radius collectively contribute to the radiance bias in Fig. 3.3 (d). The STD of the radiance residual is of a similar magnitude to the mean bias, suggesting that removing the mean bias would not significantly reduce the errors in the simulated spectra. The RMSE of $R(Re_0, slab)$ shows a minimum of around 0.1 K in the mid-infrared window and a maximum over 0.5 K in the far-infrared channels. This RMSE spectrum, referred to as ε_{cld}, is also calculated using an AIRS-like spectral response function to represent the radiance uncertainty induced by the slab-cloud assumption in the retrieval described in Section 3.2.3.

We further examine whether the addition of radiance uncertainty due to the slab-cloud assumption (ε_{cld}) masks spectral signals from atmospheric variations simulated by the NWP model. Figure 3.1 depicts that strong cooling and hydration appears above overshooting DCCs near the cyclone center (141°E, 16°N). We denote the mean profiles of this region as t_{cold} and q_{mois} for temperature and water vapor, respectively, which are shown in Fig.3.4 (b,d) blue curves. A set of radiative transfer calculations is conducted to obtain $R(t_0, q_0)$, $R(t_{cold}, q_{mois})$ and $R(t_{cold}, q_0)$ at 0.1 cm^{-1} spectral resolution, using an effective radius of $21.5\ \mu\mathrm{m}$ and a randomly selected IWC profile (cloud top at 100 hPa) of this region. The spectral signals of temperature and water vapor are then obtained from $R(t_0, q_0) - R(t_{cold}, q_0)$ and $R(t_0, q_0) - R(t_0, q_{mois})$, respectively. The strength of signals under different spectral specifications was examined by Chapter 2 and is not repeated here. The spectral signals are then compared to radiance uncertainties in Figure 3.4.

Figure 3.4 shows that the radiance uncertainty from the slab-cloud assumption, ε_{cld}, does not completely obscure the signal of temperature or water vapor. In the $\mathrm{CO_2}$ and water vapor channels, where the signal is the strongest, the TOA radiances are not as sensitive to cloud emission due to a stronger atmospheric attenuation at these channels. ε_{cld} becomes greater in the wings of absorption channels, where the signals are already masked by the instrument NEdT of $\sim 0.5\text{K}$.

3.2.3 Retrieval Algorithm

The cloud-assisted retrieval proposed by Chapter 2 is an optimal estimation method [Rodgers, 2000] that retrieves atmospheric states above clouds using infrared spectral radiance. Similar to Eq.1 in Chapter 2, we express the relation between the observation vector, y, and the state vector, x, as follows:

$$y = F(x_0) + \frac{\partial F}{\partial x}(x - x_0) + \varepsilon \tag{3.1}$$

$$= y_0 + K(x - x_0) + \varepsilon \tag{3.2}$$

Following a similar definition to Chapter 2, the state vector includes temperature x_t and the logarithm of specific humidity, x_q, in 67 model layers. x_0 refers to the first guess of the state vector, which is the mean of the $a\ priori$. y contains the infrared radiance observations, y_{rad}. F is the forward model that relates x to y. Here, the forward model is the radiative transfer model, MODTRAN 6.0, configured with the spectral response function of the AIRS instrument. The forward model can be linearly approximated by the Jacobian matrix K, which is iteratively computed at every time step. ε is the measurement error.

Following the optimal estimation method [Rodgers, 2000, Eq.5.16], an estimate of x, $\hat{x}$, is expressed as:

$$\hat{x} = x_0 + GK(x - x_0) + G(y - Kx) \tag{3.3}$$

$$G = S_a K^T (K S_a K^T + S_\varepsilon)^{-1} \tag{3.4}$$

Where S_a and S_ε are the covariance matrix of the state vector as given by the $a\ priori$ dataset and that of the error in the observation vector, respectively. S_ε is set to be a diagonal matrix because the observation errors in different channels are considered to be uncorrelated.

The $\hat{x}$ can then be iteratively solved through:

$$\hat{x}_{i+1} = x_0 + (K_i^T S_\varepsilon^{-1} K_i + S_a^{-1})^{-1} K_i^T S_\varepsilon^{-1} [y - F(\hat{x}_i) + K_i(\hat{x}_i - x_0)] \tag{3.5}$$

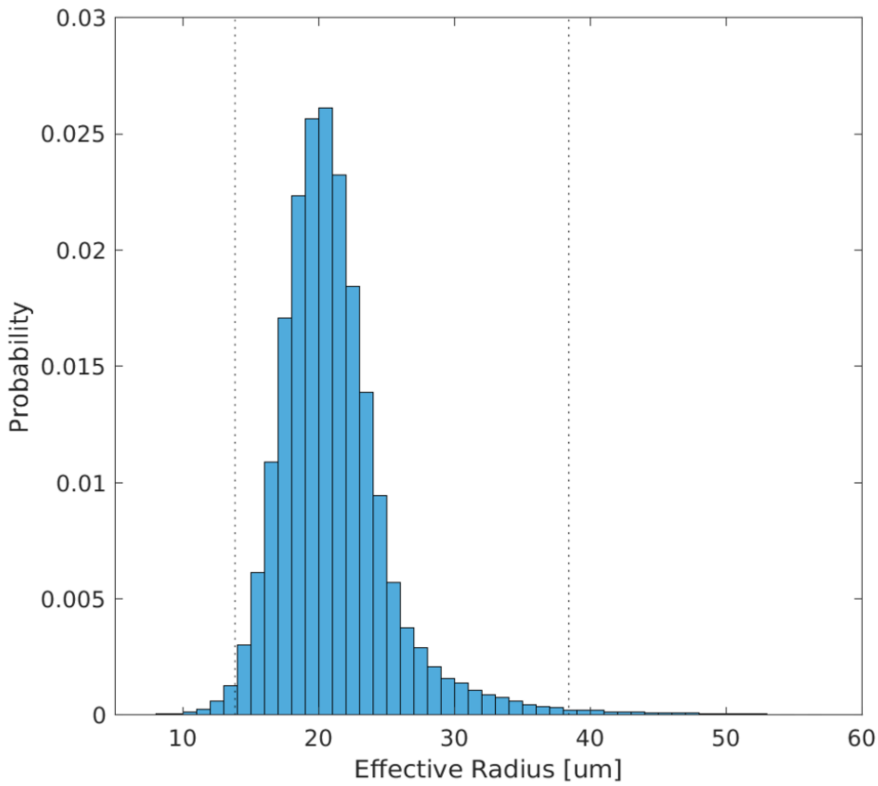

Figure 3.2: Histogram of the effective radius (μm) of cloud ice particles at the topmost layer of DARDAR, based on the 98293 overshooting deep convective samples from the DARDAR-Cloud dataset. Selected samples are within 1000 km of tropical cyclone center locations. The vertical dotted lines represent the 1st and 99th percentiles of the effective radius.

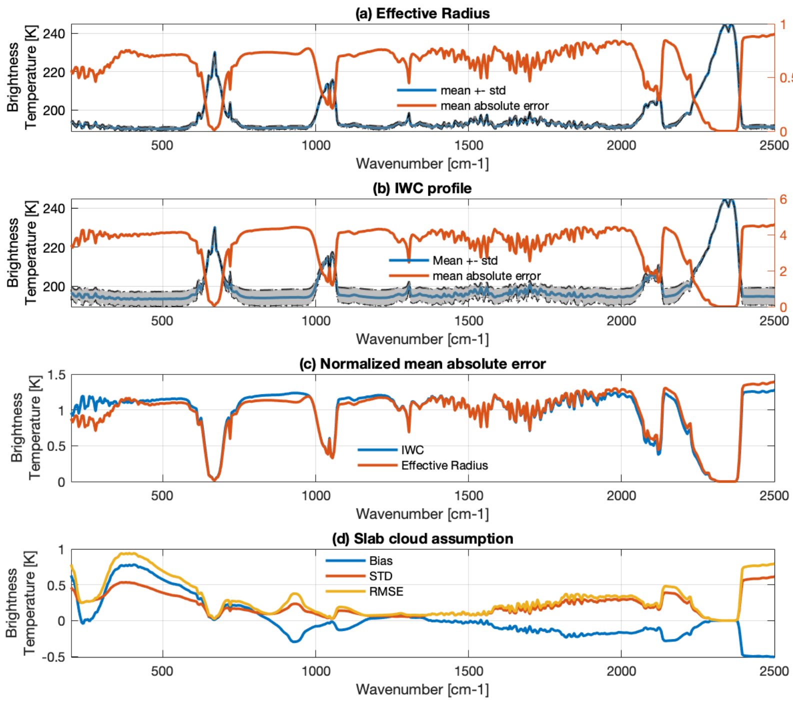

Figure 3.3: The effect of (a) effective radius and (b) IWC on the infrared radiance spectrum from 200 to 2500 cm^{-1}. The blue curves represent the mean radiance spectrum, $R(Re, IWC_0)$ and $R(Re, IWC_0)$, driven by effective radius and IWC variations, respectively. The grey areas denote the STD of the radiances. Red curves (corresponding to the right y-axis) are the mean absolute error (MAE) caused by neglecting the variation in effective radius and IWC variations. (c) The normalized MAE due to neglecting the variation in effective radius (red) and IWC (blue). (d) The mean bias, STD, and RMSE of the radiances simulated with the slab-cloud assumption, $R(Re_0, slab)$. The brightness temperature spectra are convolved and presented at a spectral resolution of 5 cm^{-1}.

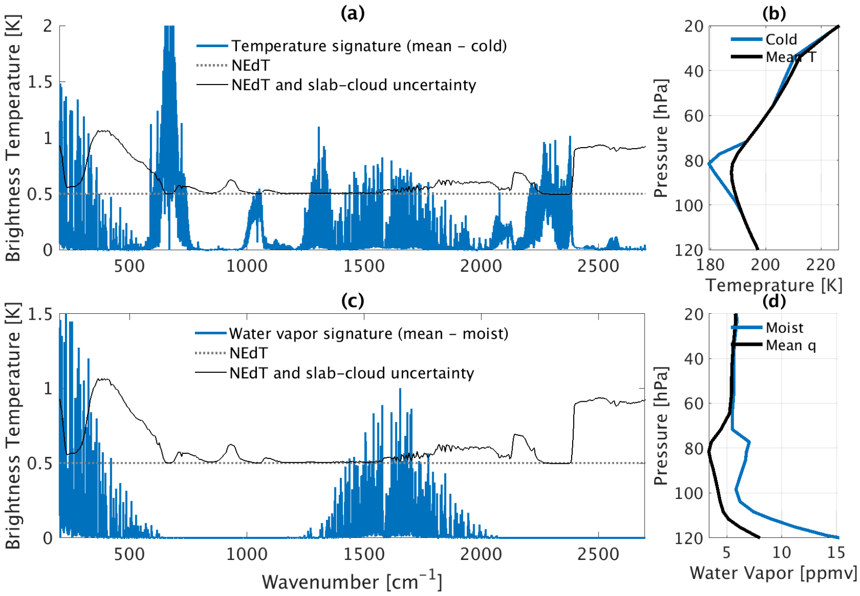

Figure 3.4: Spectral signals of above-storm atmospheric variations in (a) temperature and (c) water vapor from 200 to 2500 cm^{-1}. The signals are obtained by differencing the upwelling radiances at the TOA simulated from the mean profile (black curves in panels b and d) and the radiances simulated from the mean of profiles with overshooting convective clouds near the cyclone center (blue curves in panel b and d). These signals are shown at a spectral resolution of 0.1 cm^{-1}. In a and c, the grey dotted lines denote the NEdT of 0.5 K (characterizing the AIRS instrument at cold scene temperature) and the black solid lines denote the uncertainties combining the NEdT and ε_{cld}, which are convoluted in 5 cm^{-1} spectral intervals.

Where the subscript i refers to the ith iteration step.

The equations described above are adopted from Chapter 2, where the state vector x includes temperature and the logarithm of specific humidity. For comparison, we adopt the slab-cloud retrieval scheme of Chapter 2 as described above and refer to the result as the slab-cloud retrieval in the following. The only difference with Chapter 2 is in the S_ε. While S_ε in Chapter 2 is the square of radiometric noise of AIRS instrument, S_ε in this study for slab-cloud retrieval contains the sum of the square of radiometric noise and the square of ε_{cld}, as depicted in Figure 3.3, to account for radiance uncertainties induced by slab-cloud assumption.

3.2.3.1 Synergistic method

The radiance uncertainty due to the slab-cloud assumption, ε_{cld}, can be largely eliminated by incorporating collocated observations of cloud profiles, from active sensors (CloudSat-CALIPSO) along the same track as the hyperspectral infrared sounder (such as AIRS). Instead of simply prescribing the cloud profile from the active sensors in the forward model, motivated by the work of Turner and Blumberg [2018], we include relevant cloud variables in a synergistic retrieval. Turner and Blumberg [2018] demonstrated that additional observation vectors, such as atmospheric and cloud profiles from other instruments or NWP products, can improve convergence in cloudy scenes and the precision of the retrieval by constraining the posterior uncertainty. Following this idea, the observation vector y in Eq.1 is formulated as: $[y_{rad}, y_{other}]$, where y_{rad} contains the infrared radiance observations, and y_{other} includes elements other than radiance observations; we refer to the latter as the additional observation vector. Specifically, we include collocated cloud observations, $[y_{iwc}, y_{Re}]$ that mimic those from the DARDAR-Cloud product in the observation vector y and also add $[x_{iwc}, x_{Re}]$ to the state vector x. At every iteration step (Eq. 5), $[x_{iwc}, x_{Re}]$ is updated along with the temperature and humidity profiles.

In this simulation experiment, y_{iwc} is set to be the natural logarithm of the IWC profile to account for IWC variations from $O(10^{-5})$ to $O(1)$ $\mathrm{g/m^3}$ and to avoid negative values. The uncertainty in IWC measurements is estimated by averaging the posterior uncertainty of IWC, provided by the DARDAR-Cloud product for every footprint, in the OT-DCC profiles identified in Section 3.2.2.1. This estimated precision is denoted as ε_{iwc}, which corresponds to a roughly 20% uncertainty in IWC at vertical levels near the tropopause. Then, we account for the IWC observation uncertainty by randomly perturbing the y_{iwc} so that the y_{iwc} deviates from the true state by an error that has a standard deviation of ε_{iwc}. Similarly, the effective radius observation y_{Re} is obtained by assuming an uncertainty of 5 $\mu\mathrm{m}$. We note that this prescribed uncertainty is larger than the typical value in the DARDAR-Cloud product (1.6 $\mu\mathrm{m}$) to account for sampling differences between the instruments. Because the satellite-measured infrared radiances are most sensitive to cloud emission near the cloud top, only the top 1.5 km of the IWC profile in y_{iwc} is kept, which corresponds to six model layers in the radiative transfer calculations.

The diagonal elements of S_ε for y_{iwc} and y_{Re} are then set by conservatively quadrupling the square of the uncertainty ranges of the variables specified above.

The state vector, x_{iwc}, contains six layers of the logarithm of IWC at the same model layers as y_{iwc}. Note that x_{iwc} and y_{iwc} are not required to have the same vertical resolution; in practice, the vertical resolution of y_{iwc} can be much finer than that of the model layers. The first guess and covariance matrix of x_{iwc} are calculated using the same $a\ priori$ dataset described in the previous section, although cross-correlations between IWC and other atmospheric variables are neglected. Consequently, the forward model for relating x_{iwc} to y_{iwc} is a matrix that linearly interpolates the pressure level of x_{iwc} to match the level of y_{iwc}. x_{Re} is arbitrarily fixed at 18.5 $\mu\mathrm{m}$, assuming an uncertainty range of 5 $\mu\mathrm{m}$.

3.2.3.2 Additional atmospheric observations

Besides the cloud observations, other products that provide collocated atmospheric profiles can be useful in improving the precision of the posterior estimation. These additional products may include atmospheric observations from other instruments that are in the same satellite constellation as the hyperspectral infrared sounder. It can also come from reanalysis products, which typically do not assimilate cloudy infrared radiances in operation. In this study, we investigate the effect of incorporating coincident reanalysis products by adding an observation vector y_{atm}, which contains the temperature and the logarithm of specific humidity at a later time step: 810 minutes after the initial time, in the GEM simulation. This arbitrary choice of the simulation time step is to represent the potential quantitative differences in temperature, humidity, and cloud fields between a reanalysis product and the true state.

Distributions of retrieval variable fields are shown in Fig. 3.6. As inferred by the brightness temperature, the massive spatial coverage of DCCs is evident at the time step used as the 'Truth' (410 minutes after the initial time in the GEM simulation). At the later time step (810 minutes), the atmospheric data used as y_{atm} are taken from the same locations but deviate from the 'Truth' as they are not directly above convective overshoots at this later time step. The RMSE between atmospheric profiles from the two time steps (410 and 810 minutes) defines the uncertainties in y_{atm}. To be conservative, the uncertainty of y_{atm} is set by quadrupling the square of the RMSE in the corresponding diagonal elements of S_{ε}.

3.3 Results

Four retrieval cases are designed to assess the retrieval performance following different strategies. Among them, Cases 1 and 2 use the slab-cloud method; and Cases 3 and 4 use the synergistic method that incorporates cloud observations. Cases 2 and 4 differ from Cases 1 and 3 in that they add y_{atm} in the retrieval. The components of the state and observation vectors for the four cases are listed in Table 3.1. An additional case 5 is performed, which follows the same optimal estimation framework without using infrared radiances y_{rad} as in Case 4. It is expected to converge to $a\ posterior$ state that is jointly determined by the $a\ priori$ profile, y_{iwc}, and y_{atm}. Therefore, the statistical differences between Case 4 and 5 ascertain the improvements attributable to infrared radiances (as opposed to other sources of information). Case 5 is relatively uniform in space and it is therefore not included in the figures but listed in Tables 1 and 2 for comparison. Following the framework of this simulation experiment, retrievals are then performed for the 100-profile test set, using synthetic radiance observations (y_{rad}) generated in Section 3.2.2, IWC (y_{iwc}) and effective radius (y_{Re}) product described in Section 3.2.3.1, and additional atmospheric product (y_{atm}) constructed in Section 3.2.3.2.

We next examine the DFS [degrees of freedom for signal, [Rodgers, 2000]] of temperature and water vapor in the four retrieval cases (Table 3.1). DFS is defined as the trace of the averaging kernel A, which relates the retrieved state $\hat{x}$ to the true state x_0 , as derived from Equation 3.5 at the end of the iteration:

$$\hat{x} - x_0 = A(x - x_0) \tag{3.6}$$
$$A = (K^T S_\varepsilon^{-1} K + S_a^{-1})^{-1} K^T S_\varepsilon^{-1} K \tag{3.7}$$

While all observation vectors are used in the retrieval, only the radiance observation, y_{rad}, is included to calculate the DFS, so that a higher DFS indicates higher information content brought by y_{rad} alone. Because the DFS depends on the cloud distribution, the DFS shown in Table 3.1 is averaged over the 100-profile test set.

Although ε_{cld} does not mask the observable signals in Figure 3.4 (a,b), the DFS for temperature increases from 3.31 (Case 1) to 4.15 (Case 3) when the synergistic method is adopted. The improved DFS highlights the strong sensitivity of the synergistic method to temperature near the cloud top. In comparison, the slab-cloud method fails to fully capitalize on information near the cloud top, as it neglects contributions from the vertical layers around the assumed sharp cloud boundary. Therefore, the synergistic method is expected to achieve a better result for temperature.

Moreover, significant DFS values are found for IWC (1.87 out of 6, on average) and effective radius (0.66 out of 1, on average). The DFS confirms the sensitivity of infrared radiances to the IWC profile and effective radius near the cloud top, which is consistent with Figure 3.3 (a-c) as simulated from the DARDAR-Cloud product. The DFS for IWC varies from 0.96 to 2.71 in the test set, depending on the optical depth near the cloud top. Low ice density near the cloud top leads to a higher DFS for IWC and effective radius. For example, the DFS for IWC increases from 1.30 in Figure 3.7 (c) to 2.63 in Figure 3.7 (f), because thermal emission from lower levels can be transmitted through the topmost cloud layer. In the meantime, the DFS for effective radius increases from 0.04 to 0.66, because the thermal emission is more sensitive to the spectral shape of extinction efficiency induced by effective radius (as depicted in Fig. 3.3 (c)) when optical depth is small. Overall, the DFS values suggest that a synergistic method can improve the precision of IWC and effective radius measurements relative to collocated cloud products alone.

Retrieval performance is evaluated through the mean bias and RMSE in temperature, humidity, and IWC between the retrieved profiles and the truth, as shown in Figure 3.5.

Table 3.1: State vector and observation vector of four cases of retrieval strategies. Case 5 is a posterior estimation of the state vector from a combination of y_{atm}, y_{iwc}, y_{Re}, and $a\ priori$. DFS is compared to the number of vertical layers of the state vector. The DFS is counted from 130 hPa to 13.5 hPa for temperature and water vapor.

	x	y	DFS
		Slab-cloud	
Case 1	x_t,x_q	y_{rad}	t: 3.12/20, q: 0.78/20
Case 2	x_t,x_q	y_{rad}, y_{atm}	Same as Case 1
		Synergistic	
Case 3	x_t,x_q, x_{iwc},x_{Re}	y_{rad}, y_{iwc}, y_{Re}	t: 2.96/20, q :0.74/20, IWC :1.77/6, Re: 0.65/1
Case 4	x_t,x_q, x_{iwc},x_{Re}	y_{rad},y_{atm}, y_{iwc}, y_{Re}	same as Case 3
Case 5	x_t,x_q, x_{iwc},x_{Re}	y_{atm}, y_{iwc}, y_{Re}	\

The retrieval performance is also evaluated with regard to these quantities at selected levels and with regard to CIWV integrated from 110 to 70 hPa.

3.3.1 Slab-cloud retrieval

Improving upon Chapter 2, Case 1 accounts for the radiance uncertainties due to the slab-cloud assumption, while Case 2 further incorporates additional atmospheric constraints to improve the precision of the method.

The results of Case 1 are shown as red solid curves in Figures 3.5 and 3.7. The major improvement in Case 1, compared to the prior (blue solid curves), is the temperature profile from 100 to 75 hPa. Although DFS for water vapor reaches 0.8, Case 1 does not provide much improvement from the first guess in water vapor.

Case 2 improves from Case 1 owing to the information carried by the additional atmospheric constraints, y_{atm}. Case 2 is represented by the red dotted curves in Figures 3.5 and 3.7. It approaches the true state better than Case 1, despite warm and dry biases in the first guess and y_{atm} (See Figure 3.5 (a,c)). Notably, it increases the retrieved water vapor

Table 3.2: Performance assessments of four cases of retrieval strategies, in comparison with the prior, the observation vector, and Case 5.

	t [K] at 81 hPa		q [ppmv] at 81 hPa		CIWV [$\mathrm{g/m^2}$] from 110 to 70 hPa		IWC [$\mathrm{g/m^3}$] at 90 hPa		Re [μm]	
	Bias	RMSE	Bias	RMSE	Bias	RMSE	Bias	RMSE	Bias	RMSE
prior	6.8	7.1	-1.8	1.5	-0.30	0.34	-0.0014	0.0237	-3	3
$[y_{atm}, y_{iwc}]$	7.7	10.4	-1.7	2.3	-0.17	0.24	-0.0049	0.0094	4.48	5.56
Slab-cloud										
Case 1	-0.1	4.5	-1.8	2.4	-0.28	0.37	\	\	\	\
Case 2	0.8	4.1	-0.6	1.0	-0.11	0.16	\	\	\	\
Synergistic										
Case 3	-0.2	3.5	-1.7	2.2	-0.2	0.30	0.0028	0.0051	-0.25	0.84
Case 4	0.8	2.7	-0.8	1.1	-0.09	0.16	0.0027	0.0051	-0.23	0.83
Case 5	2.7	4.9	-1.5	2.0	-0.15	0.25	-0.0041	0.0089	1.42	1.62

concentration by around 1 ppmv on average and reduces the RMSE from 2.4 ppmv to 1.0 ppmv, as shown in Figure 3.5 (c,d) and Table 3.2. For the CIWV, Case 2 reduces the RMSE by half when compared to Case 1.

To demonstrate how well the retrieved atmospheric field represents the spatial variability in the true state (Figure 3.1), namely a moister and colder UTLS region in the cyclone center compared to the south of the domain, the distributions of water vapor, temperature, and CIWV are presented in Figure 3.6. It shows that the 'true' spatial patterns are well reproduced by the Case 2 retrieval.

Furthermore, individual profiles from two clusters of overshooting DCCs, which include the DCCs near the cyclone center and those in the south of the domain, are randomly selected to investigate how well the retrieval reproduces the spatial variability in temperature and water vapor. The all-sky optical depths from TOA and IWC profiles for the two locations are shown in Figure 3.7 (c,d). The retrievable signals mainly come from the atmospheric column above thick cloud layers, i.e., where optical depth is less than 2 (only 13.5% of the infrared emission is transmitted through this cloud layer).

Figure 3.7 (a-c) shows results for a location close to the cyclone center. At this location, the slab-cloud method prescribes the cloud layer to be located at the cold-point due to the strong cloud emission. Atmospheric anomalies above 86 hPa have an impact on TOA infrared radiances. Around 80 hPa, the truth profile that we aim to retrieve is around 8 K colder than the prior and nearly 3 ppmv moister. While the result from Case 1 overcomes the bias in temperature, it increases the water vapor over a broad vertical range which, as explained by Chapter 2, is due to the strong smoothing (smearing) effect of the averaging kernel in this case. In comparison, Case 2 correctly produces a peak moistening around 80 hPa, while keeping a retrieved temperature profile similar to Case 1.

Figure 3.7 (d-f) shows the results in a location in the southern part of the domain, where the slab-cloud method prescribes the cloud layer at 95 hPa. At this location, the cloud emission from the top 1.5 km cloud layer affects infrared radiances strongly, which can be inferred from the optical depth (Figure 3.7 (f)), leading to a large radiance residual that cannot be addressed under the slab-cloud assumption. Therefore, Case 1 fails to improve upon the prior. Case 2 leads to a moister posterior compared to the prior owing to the addition of y_{atm}. However, Case 2 fails to update the temperature profile above the cloud layer. Instead, it approaches y_{atm} in lower altitudes, leading to an unrealistic vertical oscillation in temperature near 100 hPa.

3.3.2 Synergistic method

Using the synergistic method, Case 3 becomes more sensitive to water vapor and temperature compared to Case 1, as indicated by the reduced RMSE in Table 3.2 and a closer match between the retrieved field and the true state in Figure 3.6. It retrieves higher water vapor concentrations from 110 to 70 hPa in comparison with Case 1. Owing to the radiative emission from in-cloud layers between 110 and 95 hPa, Cases 3 and 4 become sensitive to the temperature profile near the cloud top. Hence, Cases 3 and 4 reduce the RMSE compared to other cases.

The advantage of the synergistic method, especially when IWC near the cloud top is relatively small, is illustrated in Figure 3.7 (d-f). At this location, the radiative signal from the moistening near the cloud top can be transmitted to the TOA. As a result, Case 3 approaches the true cloud-top temperature much better than Cases 1 and 2 (Figure 3.7 (a,d)). It also produces higher water vapor compared to Case 1 (Figure 3.7 (e)). Case 4 further

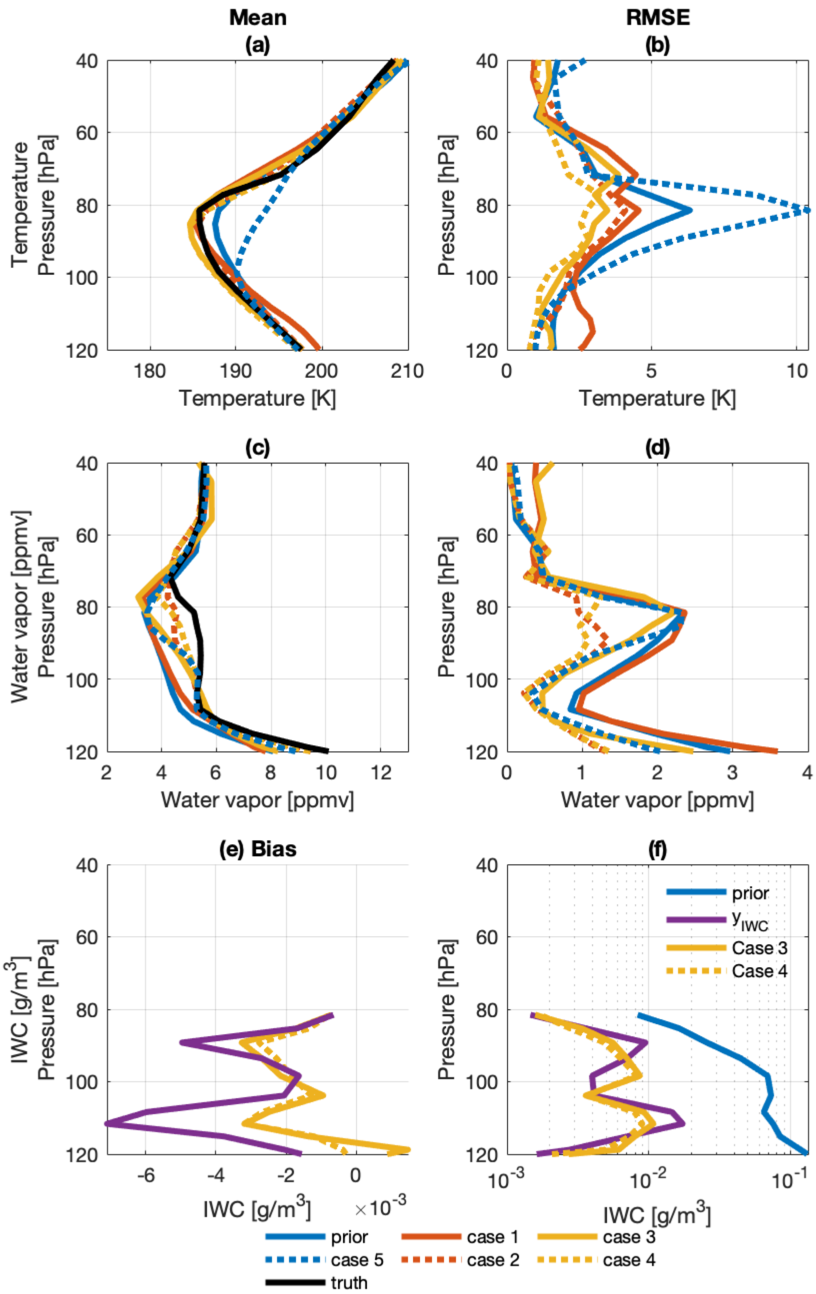

Figure 3.5: The mean and RMSE of temperature (a,b), water vapor (c,d) profiles from the four cases of retrieval strategies. Bias (e) and RMSE (f) of IWC profiles. Blue curves show the bias and RMSE in the prior. Retrieval cases using the slab-cloud method are marked by red curves (case 1 in solid and case 2 in dotted curves), while the retrievals using the synergistic method are marked by yellow curves (case 3 in solid and case 4 in dotted curves).

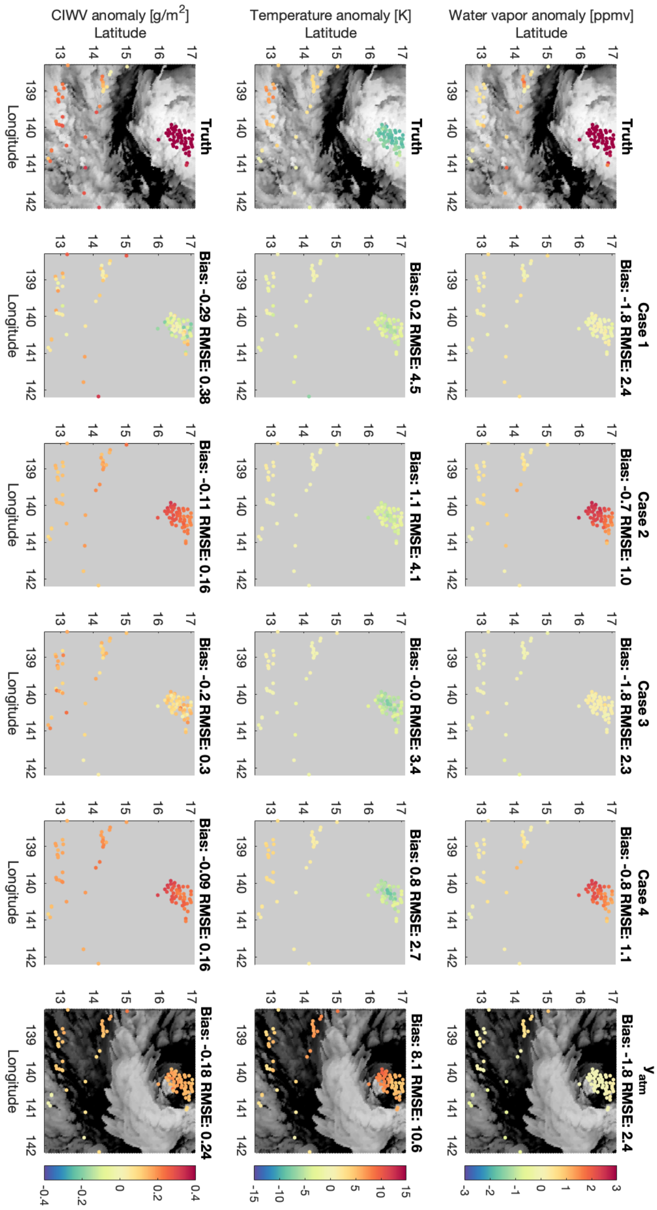

Figure 3.6: Horizontal distributions of the anomalies, defined as the deviation from x_0, in water vapor (in the units of ppmv, upper panels), temperature (in the units of K, middle panels) at 81 hPa, and column integrated water vapor between 110 and 70 hPa (in the units of $\mathrm{g/m^2}$, lower panels). The true states are shown in the first row, with background grey shaded for BT_{1231}. The second to fifth rows show retrieved results from the four cases of retrieval strategies described in Table 3.1. The sixth-row shows distribution of the additional observation vector, y_{atm}, incorporated in the retrievals of Cases 2 and 4. This additional atmospheric constraint, y_{atm}, is taken from the model fields 810 minutes after the initial simulation time step.

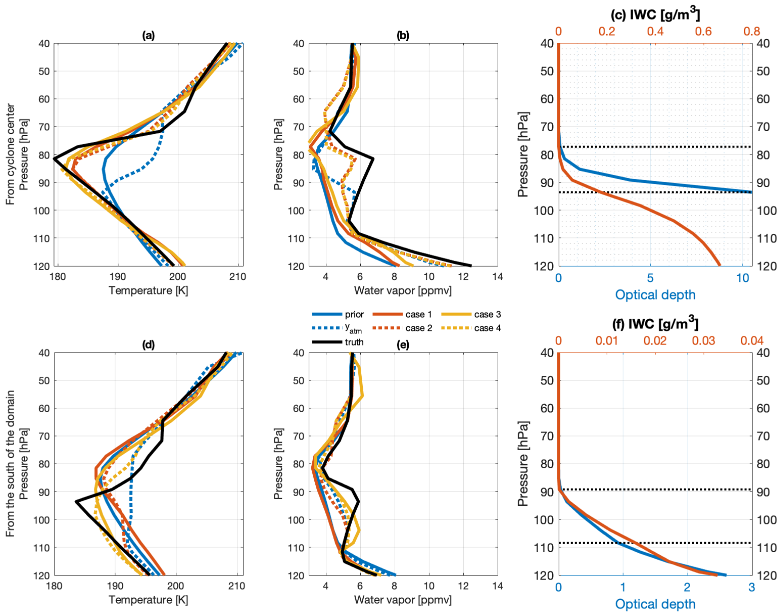

Figure 3.7: (a,d) Temperature and (b,e) water vapor profiles of first guess (blue solid), truth (black solid), and posterior results (red and yellow curves represent the slab-cloud and synergistic methods, respectively, while the solid curves are cases without y_{atm} and dotted curves include y_{atm}) for two profiles from the test set. (c,f) True IWC (red curve, corresponding to the upper x-axis) and all-sky optical depth from the TOA (blue curve, corresponding to the lower x-axis) of the two selected profiles. Retrieved IWC profiles and y_{iwc} are visually similar to the true state and therefore are not shown here. Dotted black lines mark the vertical ranges of ice cloud information included in y_{iwc} and x_{iwc}, while ice clouds in the lower vertical levels are prescribed to be the same as the cloud observation.

benefits from y_{atm} which constrains the profile in the vertical ranges below 110 hPa and above 80 hPa. Case 4 overcomes the warm bias around 90 hPa in y_{atm} and the first guess. It also reproduces the oscillating temperature feature in Figure 3.7 (d).

In addition, Figure 3.5 (e,f) shows that the synergistic method can improve upon the collocated cloud observations by reducing mean biases in the IWC profile. At 90 hPa, where the retrieved 1.5 km cloud layer overlaps the most with the test set, the retrieval reduces the RMSE and mean biases in y_{iwc} by half. This can be beneficial considering the sampling difference between active sensors and infrared instruments.

While the improvement in Cases 2 and 4 shows the advantage of including additional atmospheric products, y_{atm}, one caveat is in the proper evaluation of the uncertainty range, which is included in the covariance matrix of the observation vector. This is important as the uncertainty range in y_{atm} constrains the posterior uncertainty range of the retrieval at each vertical level. In this study, we account for the difficulties in evaluating S_ε by increasing the RMSE in y_{atm}, so that the square root of S_ε of y_{atm} is equivalent to a doubling of RMSE shown by the blue dotted line in Figure 3.5 (b,d).

Although the additional measurement vector, y_{atm}, itself does not contain the spatial variability pattern as seen in Figure 3.6, the corresponding covariance in S_ε properly accounts for its variability (uncertainty) by prescribing a large value around 80 hPa but smaller values at other vertical locations. Therefore, it increases confidence in the posterior at levels where the thermodynamic variables are relatively constant. The increased confidence in turn enhances the degrees of freedom in the ranges around 80 hPa, where the warm and dry signals mainly come from. Therefore, even though y_{atm} itself deviates from the true state, including y_{atm} in optimal estimation can still improve the posterior estimation. In practice, uncertainty in atmospheric products can be estimated by inflating the precision of the product to account for sampling size differences through comparison with NWP models and collocated observations.

3.4 Conclusion and Discussion

Sounding UTLS thermodynamic conditions has long been a challenge. A simulation experiment has been conducted to simulate hypothetical radiance observations from AIRS by incorporating NWP and a radiative transfer model, MODTRAN 6.0. By conducting the simulation experiment, this study evaluates the capability of existing hyperspectral infrared sounders in detecting temperature and humidity fields above convective storms. Our focus is to investigate and constrain the uncertainties induced by clouds. Two retrieval methods are tested, including a slab-cloud method that uses mainly the infrared radiance measurements (i.e., AIRS) and a synergistic method that combines cloud products from collocated active sensors (i.e., DARDAR-Cloud).

First, we find that uncertainties in cloud properties near the top of overshooting deep convective clouds have a non-negligible impact on the TOA infrared radiances (Figure 3.3). Variations in the brightness temperature of the TOA radiance due to the vertical distribution of IWC may amount to about 4 K. The uncertainties are largest in window channels and weak absorption channels because they are sensitive to cloud emission. The slab-cloud assumption locates a clear-cut cloud top that matches the brightness temperature of the window channel. This assumption alleviates, but does not fully eliminate, the cloud effect on the radiance spectrum (Figure 3.3 (d)). The remaining radiance uncertainty is accounted for in the retrieval framework of this study and is found to not significantly obscure the temperature and humidity signals in the retrieval. Therefore, the cloud-assisted retrieval as proposed by Chapter 2 is affirmed to improve the sounding of UTLS temperature and water vapor compared to prior knowledge. However, this retrieval neglects information content from the in-cloud atmosphere. As a result, it may lead to biases in individual temperature profiles. For example, as shown in Figure 3.7 (c), the slab-cloud retrieval fails to reproduce oscillating temperature anomalies, although it still detects anomalous moistening above convective storms. Although not explicitly discussed here, a similar OE framework adopting the slab-cloud assumption is expected to detect moistening anomalies when applied to other hyperspectral infrared sounders, e.g., IASI and CrIS, due to their similar spectral specifications to AIRS.

Second, we find that the synergistic method, especially after incorporating additional atmospheric constraint, y_{atm}, is sensitive to temperature, water vapor, the IWC profile, and effective radius near the cloud top. It substantially reduces the RMSE in temperature from 7.1 to 2.7 K compared to the prior. It also reduces the RMSE in column integrated water vapor by half. This method can capture strong moistening features in individual profiles (as shown by Figure 3.7 (b)) and detect oscillating temperature anomalies (as shown by Figure 3.7 (c)). The retrieved temperature and humidity fields by synergistic approach best match the true horizontal distribution patterns on a fixed pressure level (Figure 3.6).

In conclusion, our study suggests that the synergistic method holds promise for using hyperspectral infrared radiance and cloud profiles from the existing instruments (AIRS, CloudSat, and CALIPSO) to retrieve UTLS temperature and water vapor distributions above deep convective clouds. As discussed in Chapter 2, the sensitivity to water vapor and cloud microphysics properties (see Section 3.2.2.1) can be further improved by including the far-infrared coverage provided by future instruments, e.g., FORUM and TICFIRE. While a limited number of samples is available for applying the synergistic retrieval, instruments in geostationary orbit, such as IRS (Infrared Spectrometer) and GIIRS (Geostationary Interferometric Infrared Sounder) [Schmit et al., 2009, Holmlund et al., 2021], can greatly increase collocation with other space-borne active sensors over convective regions. Such an approach may also benefit the understanding of convective impacts by providing time-continuous observations [Li et al., 2018] in future research. The ability of the synergistic method to leverage hyperspectral infrared observations to improve the NWP outputs (y_{NWP}) also suggests the advantage of including cloudy-sky observations in global data assimilation systems, as performed by Okamoto et al. [2020].

4

Impacts of tropical cyclones on the thermodynamic conditions in the tropical tropopause layer observed by A-train satellites

The tropical tropopause layer (TTL) is the transition layer between the troposphere and the stratosphere. Tropical cyclones may impact the TTL by perturbing the vertical distributions of cloud, temperature, and water vapor, although this impact is poorly quantified due to the lack of collocated data. To address this problem, we implement a synergistic retrieval approach to obtain thermodynamic profiles and ice water content above thick high-level clouds using measurements from A-Train satellites that passed over tropical cyclones.

This study detects the signatures of cyclone impacts on the distribution patterns of cloud, water vapor, temperature, and radiation by compositing these thermodynamic fields with respect to cyclone center locations. It is found that tropical cyclone events considerably increase the occurrence frequencies of TTL clouds, in the form of cirrus clouds above a clear troposphere. The amount of TTL cloud ice, however, is found to be mostly contributed by overshooting deep convection that penetrates the base of the TTL.

Using the synergistic retrieval method, we find a vertically-oscillating pattern of temperature anomalies above tropical cyclones, with warming beneath the cloud top (around 16 km) and cooling above. The atmospheric column above 16 km is generally hydrated by overshooting convection, although dehydration is detected above non-overshooting TTL clouds. Above overshooting deep convection, the column-integrated water vapor is found to be on average 40 % higher than the climatology.

Moreover, the TTL is cooled above tropical cyclones by longwave radiation. The radiative heating rates above cyclones are well differentiated by the brightness temperature of a satellite infrared channel in the window band. Using radiative calculations, it is found that TTL hydration is usually associated with radiative cooling of the TTL, which inhibits the diabatic ascent of moist air. The radiative balance of the TTL under the impact of the cyclone is therefore not in favor of maintaining the moist anomalies in the TTL or transporting water vertically to the stratosphere.

4.1 Introduction

The tropical tropopause layer (TTL, located around 15-18 km) is the transition layer between the convective overturning circulation in the troposphere and the Brewer-Dobson circulation in the stratosphere. Once entering the TTL, air tends to rise into the stratosphere, in balance with radiative heating. Clear-sky radiative heating rates become positive above the bottom of the TTL, which is marked by the level of zero radiative heating (LZRH).

The TTL plays an important role in stratosphere-troposphere exchange [Holton et al., 1995]. For example, low temperature in the TTL act as a 'cold trap' that modulates both the vertical and isentropic (quasi-horizontal) transport of water vapor to the lower stratosphere [Dessler et al., 1995, Brewer, 1949, Holton and Gettelman, 2001, Gettelman et al., 2002a], where water vapor, despite its low concentration, may have a large impact on radiation, climate, and atmospheric chemistry [Solomon et al., 2010, Anderson et al., 2012, Dessler et al., 2013, Huang et al., 2016].

Given their vertical extent, deep convection potentially provides an important pathway to transport water vapor and other constituents to the stratosphere via the TTL. Deep convection may affect the TTL in several ways. First, tropical deep convection, especially in tropical cyclones, is associated with strong dynamical cooling around the tropopause level [Holloway and Neelin, 2007]. Second, the injected ice and water vapor, together with the temperature anomalies caused by deep convection, can modify the radiative heating in the TTL, which in turn can either speed up or slow down the upwelling motion of air and the transport to the stratosphere. Consequently, air convectively injected into the TTL can be either a source or a sink of water vapor, depending on the pre-existing relative humidity [Jensen et al., 2007, Ueyama et al., 2018, Schoeberl et al., 2018]. Simulations and observations have shown that deep convection may hydrate the upper-troposphere and lower-stratosphere (UTLS) by directly injecting water vapor and ice above mid-latitude [Anderson et al., 2012, Sun and Huang, 2015, Qu et al., 2020] and tropical storms [Avery et al., 2017, Schoeberl et al., 2018], or dehydrate it by condensing the pre-existing water vapor to ice particles in supersaturated environments [Ueyama et al., 2018].

On the other hand, climate models and global reanalysis datasets are subject to common problems in representing key processes, such as convective parameterization, [e.g., Takahashi et al., 2016], in the UTLS region. These problems include a persistent wet bias in upper tropospheric humidity [Huang et al., 2007, Jiang et al., 2012, 2015], discrepancies in the transportation speed of water vapor from the upper troposphere to the lower stratosphere [Jiang et al., 2015, Schoeberl et al., 2012] and contradictory assessments of cloud impacts on diabatic heating in the TTL region [Wright and Fueglistaler, 2013, Wright et al., 2020].

Existing satellite datasets [Waters et al., 2006, Bernath et al., 2005, Anthes et al., 2008] and aircraft campaigns [e.g., Jensen et al., 2013, Lee et al., 2019] have advanced understanding of the TTL region, although the study of deep convective impacts on temperature, water vapor, and clouds in the TTL region is still impeded by a lack of collocated measurements of these variables. The A-Train constellation [L'Ecuyer and Jiang, 2011], including Aqua, CloudSat, CALIPSO, PARASOL, and Aura, carries over 20 instruments that monitor clouds and other atmospheric variables. However, the sounding of thermodynamic conditions above deep convection, especially near the convective core, remains a challenge [Livesey et al., 2017, Olsen et al., 2013]. Chapter 2 found that the retrievability of temperature and water vapor is improved by an underlying cloud layer because the cloud layer reduces the degeneracy caused by non-monotonic vertical temperature variations and the smearing effect of lower-level water vapor, and proposed a cloud-assisted retrieval algorithm that can be applied to infrared hyperspectral measurements, such as those from the Atmospheric Infrared Sounder [AIRS, Chahine et al., 2006] aboard Aqua [Parkinson, 2003]. Chapter 3 further developed a synergistic method that incorporates cloud measurements of collocated active cloud profilers. By conducting a simulation experiment, Chapter 3 demonstrated that this method can capture the variability of temperature and humidity above tropical convective storms and improve retrievals near the cloud top through the incorporation of information from active sensors.

In this study, we aim to quantify the effect of tropical cyclones on TTL temperature, water vapor, and clouds using A-Train satellite observations, specifically hyperspectral infrared measurements from AIRS and cloud profiles from CloudSat/CALIPSO. Tropical cyclones are of particular interest here because they constitute a large fraction of the most energetic (overshooting) convective clouds in the tropics [Romps and Kuang, 2009] and provide vertically extended dense high clouds that enable the above-cloud temperature and humidity retrieval method developed by Chapters 2 and 3. By using satellite observational datasets, which are introduced in Section 4.2, we aim to understand: 1) how tropical cyclones, especially the overshooting events, impact TTL cloud occurrence and cloud ice (see Section 4.3.1 and 4.3.2), 2) whether tropical cyclones lead to an overall hydration in the TTL (see Section 4.3.3), and 3) how tropical cyclones affect radiative heating in the TTL (Section 4.4). These questions are further discussed together with key conclusions in Section 4.5.

4.2 Data and Methodology

4.2.1 Datasets

Following a sun-synchronized orbit with a repeat-cycle of 16 days, the A-Train satellites cross the equator at around 1:30 pm solar time in the ascending nodes and 1:30 am in the descending nodes every day.

CloudSat [Stephens et al., 2008] uses a cloud profiling radar operating at 94-GHz to observe cloud and precipitation. Sampling along-track at every 1.1 km, each measurement has a cross-track resolution of 1.4 km and along-track resolution of 1.8 km. With a vertical resolution of around 500 m, CloudSat provides several products, including cloud water content (2B-CWC-RVOD), cloud classification (2B-CLDCLASS-LIDAR), and radiative heating rates (2B-FLXHR-LIDAR). In the 2B-CLDCLASS-LIDAR product, eight cloud types are classified, including cirrus, altostratus, altocumulus, stratus, stratocumulus, cumulus, nimbostratus, and deep convective clouds, depending on the vertical distribution of hydrometeors inferred from radar signal intensity and also their horizontal length scales [Wang and Sassen, 2007]. The heating rate profiles in 2B-FLXHR [L'Ecuyer, 2007] are derived from two-stream broadband radiative transfer calculations combining the 2B-CWC cloud water content profile and atmospheric state profiles (temperature, water vapor, and ozone) from ECMWF forecasts, which are included in the ECMWF-AUX product [Partain, 2004].

The DARDAR [raDAR/liDAR; Delanoë and Hogan, 2008, 2010] product is based on a joint retrieval of ice cloud properties by using radar reflectivity measurements from CloudSat and lidar attenuated backscatter measurements obtained from CALIPSO [Cloud, Aerosol Lidar and the Infrared Pathfinder Satellite Observations; Winker et al., 2003] in synergy. Combining these two active instruments, DARDAR is sensitive to both optically thin cirrus in the TTL and optically thick deep convective clouds (DCC). It provides estimates of ice water content (IWC), the effective radius of ice particles, and the visible optical depth of ice clouds at each CloudSat footprint spaced every 1.1 km.

In this study, we obtain the IWC profiles from the DARDAR-Cloud product (v2.1.0) and the cloud types from the CloudSat 2B-CLDCLASS-LIDAR product. Discrepancies exist between the CloudSat 2B-CLDCLASS-LIDAR and DARDAR products in terms of ice cloud existence. To overcome these discrepancies, a cloud layer detected by DARDAR but not classified in 2B-CLDCLASS-LIDAR is treated as the same cloud type as its adjacent cloud layer, or as cirrus if it is isolated.

The Aura Microwave Limb Sounder [MLS, Waters et al., 2006] retrieves water vapor pressure less than 316 hPa with a vertical resolution of around 3 km. The documented accuracy of the version 4.2 product at the level of 100 hPa is 8% for water vapor. Although MLS can retrieve atmospheric states in moderately cloudy conditions, line shape distortion caused by the strong scattering of thick clouds limits the retrieval capability [Livesey et al., 2017]. Therefore, only data not affected by clouds, based on the $status$ flag included with the product, are used to avoid degraded data quality. Moreover, due to the limb-viewing scanning geometry, MLS has a relatively large sampling footprint with a horizontal resolution around 200 km along the track, which limits its sensitivity to small-scale variability [Schwartz et al., 2013].

AIRS measures infrared spectra from 650 cm^{-1} to 2665 cm^{-1} with 2378 channels, using cross-track scans to provide large spatial coverage. Only the fields-of-view (FOVs) with viewing angles within 15°of the nadir are used, considering that the limb-view geometry increases the optical depth and the atmospheric attenuation. The selected viewing angle corresponds to a cross-track span of around 400 km. The high spectral resolution in the mid-infrared makes AIRS sensitive to temperature, water vapor, and also clouds. However, the standard AIRS retrieval is not sensitive to the water vapor signal from the extremely dry UTLS region [Fetzer et al., 2008, Gettelman et al., 2004, Read et al., 2007]. Moreover, the cloud-clearing retrieval method adopted by the AIRS standard retrieval suffers from large uncertainties in overcast conditions. Therefore, instead of using the AIRS Level 2 product for above-cloud atmospheric conditions, we apply a synergistic, cloudy-sky retrieval method developed from the cloud-assisted method proposed by Chapter 2. This retrieval method jointly uses the AIRS L1B radiance measurements to retrieve water vapor and temperature above dense high-level clouds in FOVs where collocated DARDAR-Cloud contains thick upper-tropospheric clouds. This approach is hereafter referred to as either a joint AIRS-DARDAR retrieval or a synergistic retrieval. This method has been validated by Chapter 3 and has been found to be sensitive to spatial variability in thermodynamic conditions above deep convection through a simulation experiment. The details of this retrieval method are presented in Appendix 4A.

The impact of cyclones is assessed by calculating anomalies in clouds and non-cloud variables compared to their climatological values. In this paper, we define the climatology as the multi-year monthly mean of variables from 2006 to 2016, using temperature from AIRS L2 v6, water vapor from MLS v4.2, brightness temperatures derived from AIRS L1B v5, and IWC from DARDAR. All variables are assessed on a $1^{\circ} \times 1^{\circ}$longitude-latitude grid, unless specified otherwise.

4.2.2 Compositing method

In this study, a list of tropical cyclones observed by the A-Train satellites is obtained from the CloudSat tropical cyclone product [2D-TC, Tourville et al., 2015]. This product uses best-track information provided from the Automated Tropical Cyclone Forecasting System [Tourville et al., 2015, Sampson and Schrader, 2000] to identify the cyclone center position. Note that only daytime measurements are available after April 17th, 2011, due to a spacecraft battery issue. In addition to CloudSat, we combine CALIPSO, MLS, and AIRS together to provide the cloud distributions and atmospheric states associated with each cyclone overpass.

Measurements are composited with respect to cyclone center locations in the northern part of the West-Pacific region (the boxed region in Fig. 4.1 (a)), given the abundance of data samples in this region. The density of measurement locations for each instrument is shown in Fig. 4.1. Samples from AIRS (Fig. 4.1 (d)) are of higher density compared to CloudSat (Fig. 4.1 (b)) and MLS (Fig. 4.1 (c)) owing to the advantage of the cross-track scanning of AIRS. Considering the differences in the sample densities and FOV sizes of the original measurements of these instruments, the cyclone-centered composites are constructed by averaging variables over different spatial scales: 60 km (CloudSat, as well as DARDAR which reports at CloudSat footprints), 120 km (MLS), and 20 km (AIRS), to ensure sufficient samples are obtained. Only observations collected over the ocean are used to avoid sample discrepancies arising from land-sea contrast. Fewer nighttime measurements are available because of the daylight-only operation of CloudSat after 2011.

4.3 Tropical cyclone impacts

4.3.1 Cloud distribution

The datasets introduced earlier are used to depict the cloud distributions above cyclones. DCCs and TTL clouds are especially of interest here. DCCs are classified in the CloudSat 2B-CLDCLASS-LIDAR dataset based on several conditions, including a vast horizontal and vertical extent, dense hydrometers (as inferred from radar reflectivity near the cloud top), and also the presence of precipitation [Wang and Sassen, 2007]. TTL clouds, for the

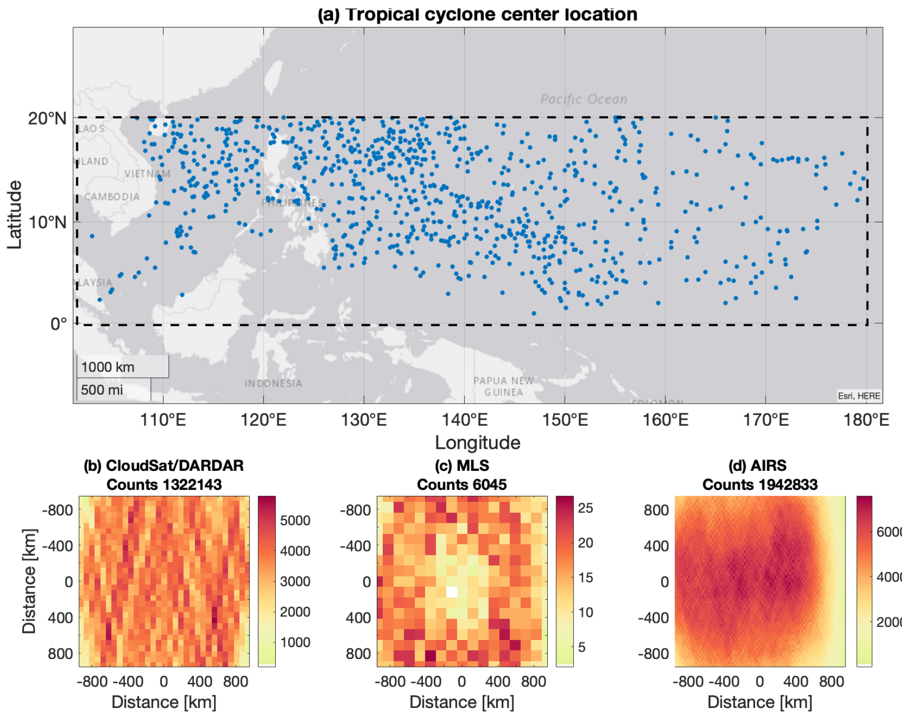

Figure 4.1: Distributions of cyclone centers passed over by A-Train and sample density from A-Train instruments with respect to cyclone center locations. (a) Locations of tropical cyclones centers (947 in total) overpassed by the A-Train satellites from 2006 to 2016 over the northern part of the West-Pacific region (within the boxed area). The sample density of (b) CloudSat (the DARDAR product is available at the horizontal footprints of CloudSat), (c) MLS, and (d) AIRS (limited to viewing angles within 15°of nadir) with respect to distances to cyclone center locations. The sample densities are measured as the number of samples per 100 $\mathrm{km} \times 100$ km area and are shown at resolutions of 60 km, 120 km, and 20 km, respectively, for the three instruments. The numbers on the top of each panel show the total number of samples.

convenience of the analysis, are defined as clouds above 16 km, near where the clear-sky LZRH and mean tropopause [WMO, 1957] height are typically located in the tropics [Yang et al., 2010].

The occurrence frequency of clouds is then calculated as the ratio between the number of samples with a certain feature, e.g., TTL clouds, and the number of overpass samples in each 60 km × 60 km grid box in the cyclone-centered composite domain (Fig. 4.2 (a-b)). Using IWC profiles from DARDAR-Cloud, a composite of ice water path (IWP) is derived in the same grid boxes. These results are also shown as a function of radial distance from the cyclone center in Fig. 4.3 (a-c).

Fig. 4.2 (a) and Fig. 4.3 (a) show that TTL clouds occur frequently above tropical cyclones. In the 2000 km × 2000 km cyclone-centered composite domain, TTL clouds have an occurrence frequency of 0.37 on average, which is significantly greater than the climatological value of 0.03. This climatological value is derived from the DARDAR-Cloud from 2006 to 2016, regardless of the presence of cyclones. DCCs occur mostly within 400 km of the cyclone center (Fig. 4.3 (a)) and are noticeably more often on the southwest side of tropical cyclones (Fig. 4.2 (b)). The occurrence frequency of DCCs in the composite domain is 0.1 on average, while the climatological value (regardless of cyclone condition) is only 0.008. These results suggest that tropical cyclones considerably increase the occurrence frequencies of both DCCs and TTL clouds.

In contrast to the uniformly distributed TTL cloud (Fig. 4.2 (a)), Fig. 4.2 (c) shows that the TTL cloud ice is concentrated in regions closest (within 200 km) of the cyclone center, most often to the southwest, similar to the DCCs (Fig. 4.2 (b)). This coincidence suggests a linkage between TTL cloud ice and DCCs that penetrate the bottom of TTL (around 16 km altitude). We refer to these as "overshooting" DCCs in the context of this paper.

TTL clouds are then broken into four categories to distinguish TTL clouds with or without underlying deep convective clouds. As shown by the schematic in Fig. 4.4, the four cloud categories are defined as follows:

- DCC-OT: overshooting DCCs, whose top boundary exceeds 16 km.
- DCC-NOT: non-overshooting DCCs, whose top boundary is below 16 km, with

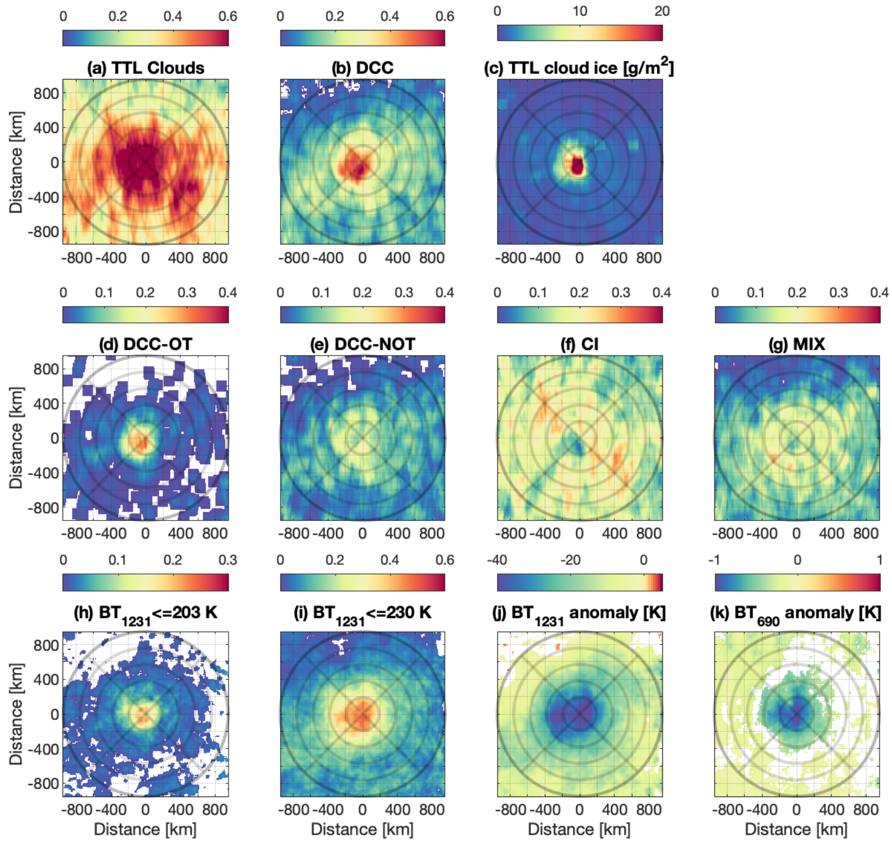

Figure 4.2: Cyclone-centered composite of cloud statistics. (a) The occurrence frequency of TTL clouds (i.e., clouds above 16 km) and (b) deep convective clouds (regardless of TTL cloud occurrence). (c) Ice water path ($\mathrm{g/m^2}$) above 16 km. The occurrence frequency of four cloud categories (schematically shown in Fig. 4.4): (d) DCC-OT, (e) DCC-NOT, (f) CI, and (g) MIX. The occurrence frequency of clouds identified by infrared radiance measurements: (h) deep convective clouds with $BT_{1231} <= 203$ K and (i) overcast high clouds with $BT_{1231} <= 230$ K. (j) Brightness temperature anomalies [K] in an atmospheric window channel (BT_{1231}) and (k) a CO_2 channel (BT_{690}). Upper (a-c), middle(d-g), and lower (h-k) panels are based on data from DARDAR-Cloud-IWC, CloudSat-2B-CLDCLASS-LIDAR, and the AIRS L1B v5 product, respectively. Only statistically significant occurrence frequencies (at a 99% confidence level, compared to zero) are shown in (a,b,d-i), and only significant brightness temperature anomalies (99%, compared to the climatology) are shown in (j,k).

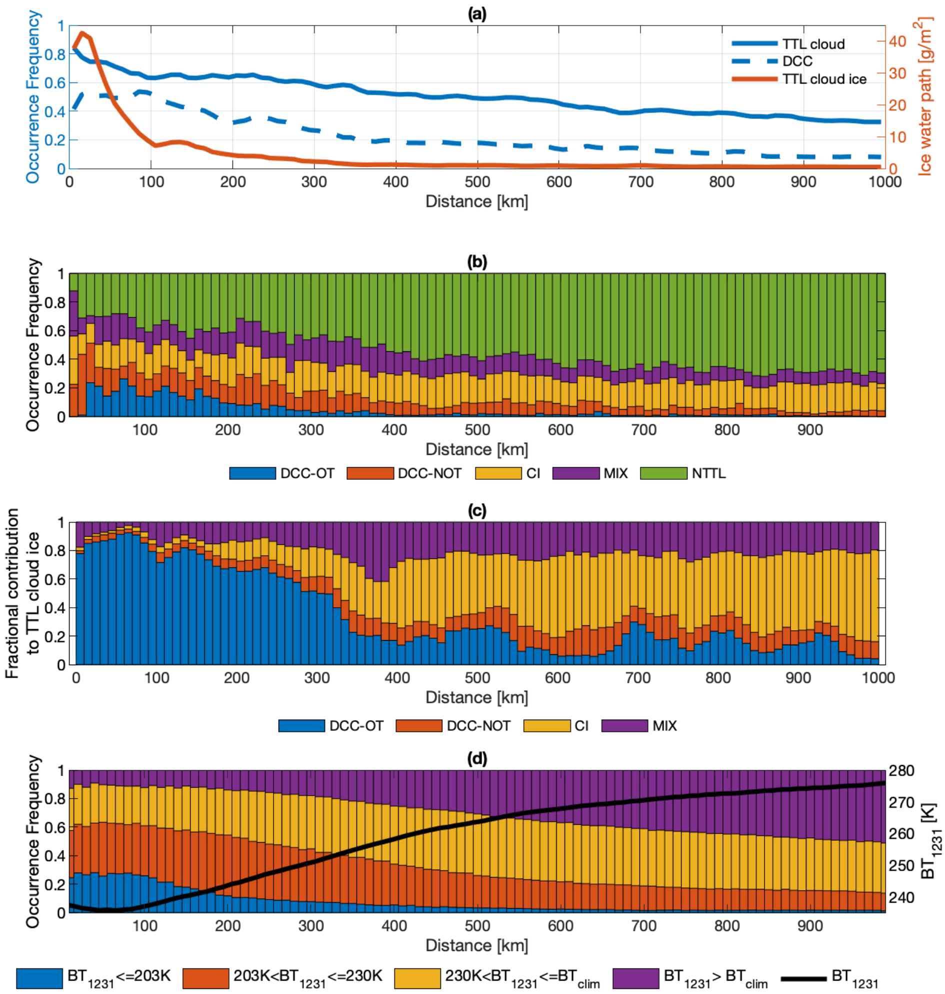

Figure 4.3: Cloud statistics as a function of radial distance to cyclone center. (a) Occurrence frequency of TTL clouds (blue solid curve) and deep convective clouds (blue dashed curve); the red curve is the ice water path ($\mathrm{g/m^2}$) above 16 km. (b) Occurrence frequency of each cloud category (schematically shown in Fig. 4.4). (c) Fractional contribution to the TTL cloud ice (the red curve in panel (a)) by each cloud category. (d) Occurrence frequencies of clouds classified by BT_{1231}. BT_{clim} refers to the multi-year monthly mean BT_{1231}. The black curve shows the average BT_{1231}.

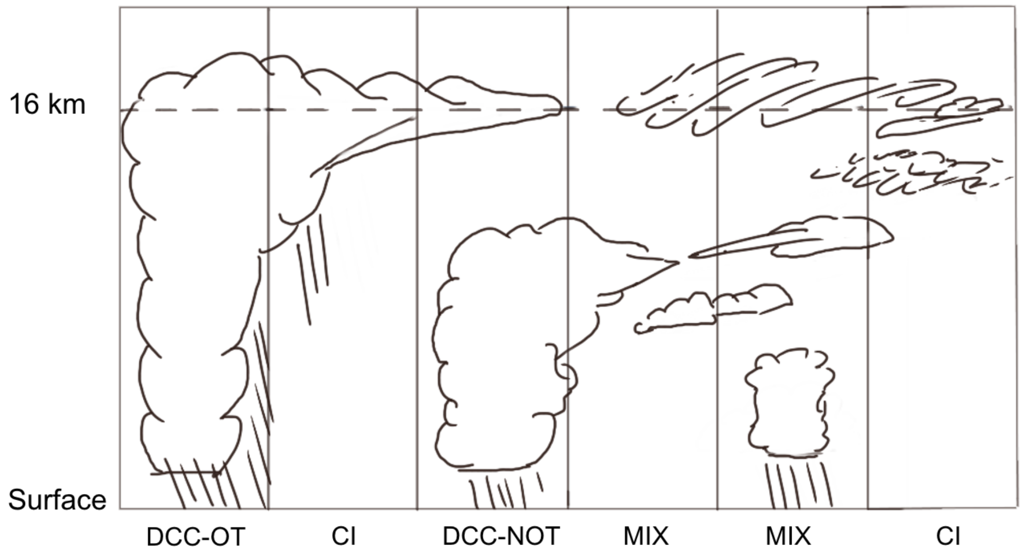

Figure 4.4: A schematic of the TTL cloud categories (see definitions in Section 4.3.1).

cloud detected above 16 km.

- CI: cirrus detected above 16 km and no DCC or any other cloud in the column.
- MIX: the remaining conditions (no DCC, but cloud detected above 16 km).

For convenience, TTL cloud categories without overshooting, including DCC-NOT, CI, and MIX, are also grouped as TTL-OTHER. Clouds with their top boundary below 16 km are referred to as NTTL.

As depicted by Fig. 4.4, we distinguish the DCC-OT and DCC-NOT by whether the lowermost TTL clouds are connected with underlying DCCs, because the adjacent clouds are essentially considered as the same cloud type in the CloudSat cloud classification dataset (2B-CLDCLASS). Columns with only cirrus clouds are classified as CI. In the MIX category, the TTL clouds may lie over either middle clouds (accounting for 90% of the MIX category) or low clouds (10% of the MIX category). MIX and CI categories also include optically thick anvil clouds near the edge of DCCs, because anvil cloud is classified as cirrus or altostratus in the 2B-CLDCLASS-LIDAR [Wang and Sassen, 2007, Young et al., 2013], depending on its vertical position,

Following this classification, we compute the occurrence frequency of each cloud category and its fractional contribution to TTL cloud ice. The fractional contribution to TTL cloud ice in a grid box is calculated as the ratio between the sum of TTL cloud ice of one cloud category and the total TTL cloud ice. DCC-OTs frequently occur within the 400 km radius, accounting for the majority of TTL cloud ice (Fig. 4.3 (c)). The CI category has an occurrence frequency generally over 0.2, which makes up over 60% of the total TTL cloud occurrence outside the 400 km radius (Fig. 4.2 (f) and Fig. 4.3 (b)), but contributes little to the TTL cloud ice (Fig. 4.3 (c)). Overall, Fig. 4.2 and 4.3 indicate that most TTL clouds above cyclones are of the CI type, while the TTL cloud ice is predominantly contributed by overshooting deep convective clouds (DCC-OT).

4.3.2 Infrared Radiance

In the previous section, the distribution patterns of clouds above tropical cyclones are analyzed by combining observational products from CloudSat and CALIPSO. Compared with the nadir-view-only instruments, AIRS provides expanded spatial coverage by performing a cross-track scan. With over two thousand channels, this hyperspectral instrument can resolve atmospheric absorbers and temperatures profile. For example, the brightness temperature (BT) in the atmospheric window channel is sensitive to cloud top temperature and this is useful for inferring cloud top height.

As described in Section 4.3.1, overshooting DCCs are a major source of TTL cloud ice. The spectral signatures of the overshooting DCCs are further investigated. Previous studies [Aumann et al., 2011, Aumann and Ruzmaikin, 2013] have shown that overshooting DCCs are identifiable by cold BT anomalies in the window channels, e.g., at the 1231 cm^{-1} channel (BT_{1231}) and also positive BT difference between the water vapor and window channels ($\Delta BT = BT_{1419} - BT_{1231}$), [Aumann et al., 2011, Aumann and Ruzmaikin, 2013]. The cold BT_{1231} is a result of the extremely high vertical reach (and thus the very low cloud top temperature) of the DCCs; the positive ΔBT indicates emission from warm stratospheric layers against the cold cloud top. However, there is no consensus on the threshold values of these quantities to identify DCCs, partly because of uncertainty in the temperature distribution above DCCs due to the impacts of convection. Following the statistical analysis detailed in Appendix 4B, we find the optimal threshold for identifying overshooting DCCs to be $BT_{1231} <= 203$ K, corresponding to a false positive rate of 0.008 and a false negative rate of 0.323. We find that incorporating ΔBT does not improve the detection.

We then apply this $BT_{1231} <= 203$ K criterion to AIRS overpass measurements (Fig. 4.1 (d)). Figure 4.2 (h) shows that the identified deep convective clouds under this criterion are distributed similarly to the overshooting DCC (DCC-OT) classified by CloudSat. It also confirms that overshooting DCCs prefer to occur in the southwest quadrant.

Similarly, a $BT_{1231} <= 230K$ criterion is used to identify thick upper-tropospheric clouds. This criterion detects cloud tops above 11 km, which corresponds to a climatological mean temperature of 230 K. The identified upper-tropospheric clouds are distributed mainly within the 400 km radius, as depicted in Fig. 4.2 (i), with a frequency of more than 0.3. Figure 4.2 (i) also reveals fewer thick high clouds on the northwestern quadrant of the domain, similar to the results based on CloudSat data (Fig. 4.2 (e,g)). This BT_{1231} criterion is also used for identifying FOVs with thick upper-tropospheric clouds to perform the synergistic retrieval method discussed in Section 4.3.3.

For each AIRS overpass sample, the BT_{1231} anomaly is calculated as the deviation from the climatology. As shown in Fig. 4.2 (j), cyclones induce a significant cold anomaly in BT_{1231} over the composite domain.

The reduced window channel radiance (BT_{1231}) suggests that cyclone clouds effectively attenuate infrared radiation emitted from the surface, thus potentially leading to a net radiative cooling of the atmospheric layers above the clouds. Hence, it is interesting to examine whether tropical cyclones leave detectable signatures in the temperature fields. A composite of BT anomalies using a CO_2 absorption channel (690 cm^{-1}) is shown in Fig. 4.2 (k). This channel has a weighting function that peaks at 85hPa, and is thus sensitive to the cold point temperatures (i.e., the vertical temperature minima) that climatologically occurs near this level. Indeed, Fig. 4.2 (k) shows a cold BT_{690} above cyclones, especially around the cyclone center. However, we cannot eliminate the possible impacts of cloud emission, which will be addressed in the following section using different methods, including a synergistic retrieval that we have developed for application to A-Train data.

4.3.3 Temperature and water vapor

In the previous sections, we find substantial increases in cloud occurrence and cloud ice above tropical cyclones. Previous studies [Ueyama et al., 2018, Schoeberl et al., 2018] have suggested that injection of TTL cloud ice can lead to either hydration or dehydration depending on the pre-existing conditions. Hence, it is important to examine the water vapor field above tropical cyclones to ascertain both the sign and the magnitude of the (de)hydration impact.

A joint AIRS-DARDAR retrieval method has been developed to retrieve atmospheric conditions above thick upper-tropospheric clouds, combining hyperspectral infrared radiances from AIRS and collocated IWC profiles from DARDAR-Cloud. The retrieval method was described in detail and validated using a simulation experiment in Chapter 3. The retrieval can achieve a precision of 0.31 K and 0.36 ppmv for temperature and water vapor at 100hPa, respectively. Additional information is provided in Appendix 4A to explain how the temperature and water vapor above tropical deep convection are retrieved.

The AIRS FOVs selected for the synergistic retrieval are within 6.75 km (half of the AIRS nadir footprint size) to the nearest DARDAR cloud profile and have window band brightness temperatures (BT_{1231}) colder than 230 K. The BT_{1231} threshold ensures that liquid clouds can be neglected in the retrieval. The frequency of AIRS FOVs passing this criterion is shown in Fig. 4.2 (i) and Fig. 4.3 (d). The selection of FOVs is illustrated in Fig. 4.6 for a tropical cyclone event. In this figure, the brightness temperature in a window channel from AIRS L1B observation depicts a typical cyclonic cloud distribution. The vertical cross-section illustrates the retrieval over selected AIRS FOVs. The same data selection and retrieval processes are performed for all tropical cyclone overpasses. In total, 3475 FOVs from 345 tropical cyclone events are selected, with 2735 profiles successfully retrieved (reaching convergence in the iterative retrieval procedure). The converged retrievals are mostly located within 500 km of the cyclone center; their distributions are shown in Fig.

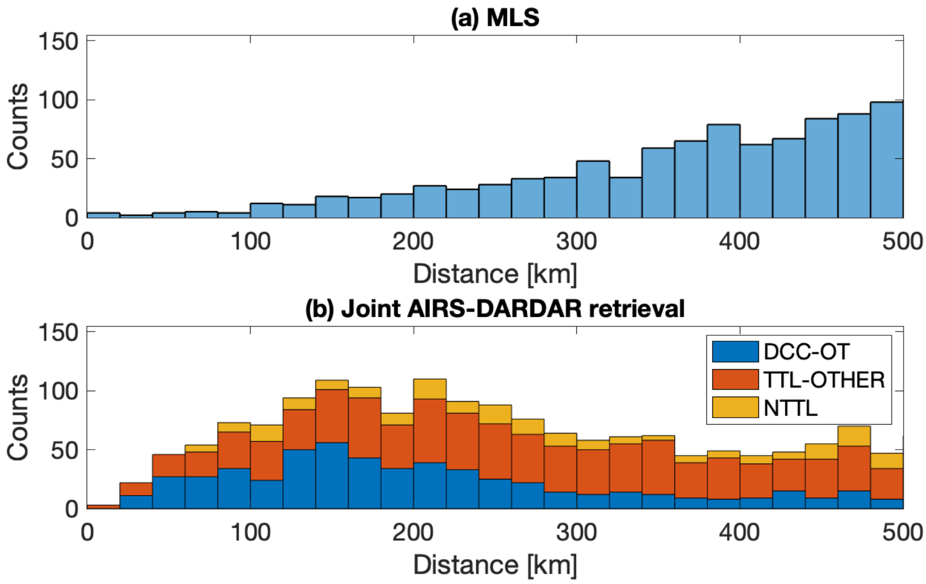

Figure 4.5: Sample densities used for assessing temperature and humidity distributions from (a) MLS and (b) the joint AIRS-DARDAR retrieval.

4.5 (b). The constructed cyclone-centered composites of retrieved temperature, water vapor, and cloud are shown as functions of vertical level and radial distance in Fig. 4.7 (a,e).

Owing to smaller horizontal sampling footprints and the availability of collocated cloud observations, the synergistic retrieval can reveal relatively small-scale variations in the thermodynamic fields above TTL clouds. In order to understand whether overshooting convection has a direct impact on water vapor, retrieved samples are classified into overshooting DCCs (DCC-OT), non-overshooting TTL clouds (TTL-OTHER), and non-TTL clouds (NTTL), using the same cloud classification introduced in Section 4.3.1. The converged profiles contain 731 DCC-OTs, 1508 TTL-OTHERs, and 496 NTTLs; their sample densities are shown in Fig. 4.5 (b). The mean profiles for each category are shown in Fig. 4.9 (a,b).

Meanwhile, similar cyclone-centered composites of thermodynamic fields are constructed using MLS v4.2 and ERA5 [Hersbach et al., 2020] in Fig. 4.7. The sample locations of ERA5 are identical to the measurement locations used for the synergistic (joint

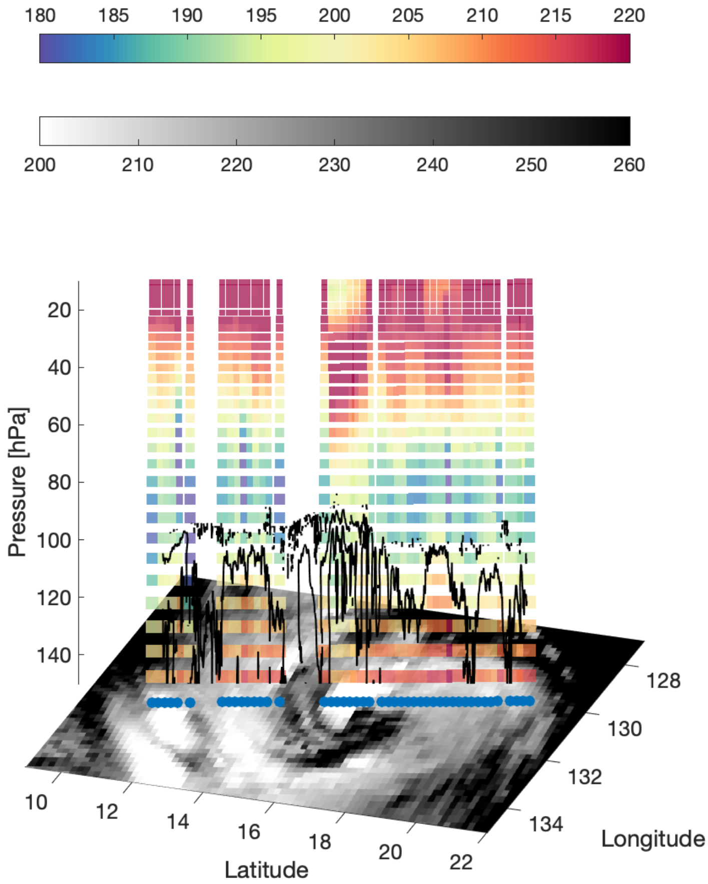

Figure 4.6: A-Train overpass and retrievals of a tropical cyclone event on October 2nd, 2007. The underlying image in greyscale shows the brightness temperature in a window channel (BT_{1231} [K]) from the AIRS L1B product and indicates the cloud-top temperature. The vertical cross-section in color contours illustrates the temperature [K] retrieval over thick upper-tropospheric clouds (BT_{1231} colder than 230 K) using the synergistic method described in the text; the black line marks the IWC at 10^{-4} g/m^3 based on the DARDAR data and outlines the cloud top positions.

AIRS-DARDAR) retrieval. The measurement locations of MLS products used in this study are shown in Fig. 4.1 (c) and Fig. 4.5 (a). The sample density of MLS near the cyclone center is lower because only measurements not affected by high clouds are used. Figure 4.7 also shows composites of IWC from the synergistic retrieval (Fig. 4.7 (a,e)), from DARDAR-Cloud (Fig. 4.7 (b,f), corresponding to measurements shown in Fig. 4.1 (b)), and from ERA5 (Fig. 4.7 (c,g)) at retrieved sample locations. We note that there is no collocation between DARDAR-Cloud and MLS in Fig. 4.7 (b,f) as only MLS observations not impacted by high clouds are selected.

The effects of cyclones on temperature and water vapor are examined by subtracting the multi-year monthly mean at every sample location from Fig. 4.7. The anomalous thermodynamic fields are presented in Figure 8, while the mean anomalies for the three cloud categories (DCC-OT, TTL-OTHER, and NTTL) are shown in Fig. 4.9 (c,d). For MLS and ERA5, the monthly mean climatologies are constructed using the same dataset (MLS or ERA5, respectively). For the synergistic retrieval, there is no available 'climatology' from this retrieval dataset for non-cyclonic conditions. AIRS L2 temperature and MLS water vapor products are used instead, which are converted to the same vertical resolution to reduce systematic bias, as described in Appendix 4A.

4.3.3.1 Temperature

Using the synergistic retrieval, we find that tropical cyclone events lead to an oscillating pattern of temperature anomalies above the cloud top (Fig. 4.8 (a)). This pattern shifts the cold-point tropopause to higher altitudes (see also Fig. 4.9 (a)). Compared with the climatology, the mean temperature profile above cyclones shows a noticeable negative anomaly between 40 to 100hPa and positive anomalies at other vertical ranges. We note that this cold anomaly around 80hPa also supports the cold signature in BT_{690} displayed in Fig. 4.2 (k). This vertically-oscillating anomaly feature is consistent with previous findings using radiosonde and GPS radio occultation measurements [Holloway and Neelin, 2007, Biondi et al., 2013, Rivoire et al., 2016].

The oscillating pattern of temperature anomalies may arise for a few reasons. The good alignment of the cold anomaly with the cloud top position around the cold point ($\sim$80 hPa) implicates the impact of cloud radiative effects. This motivates us to ascertain the role of

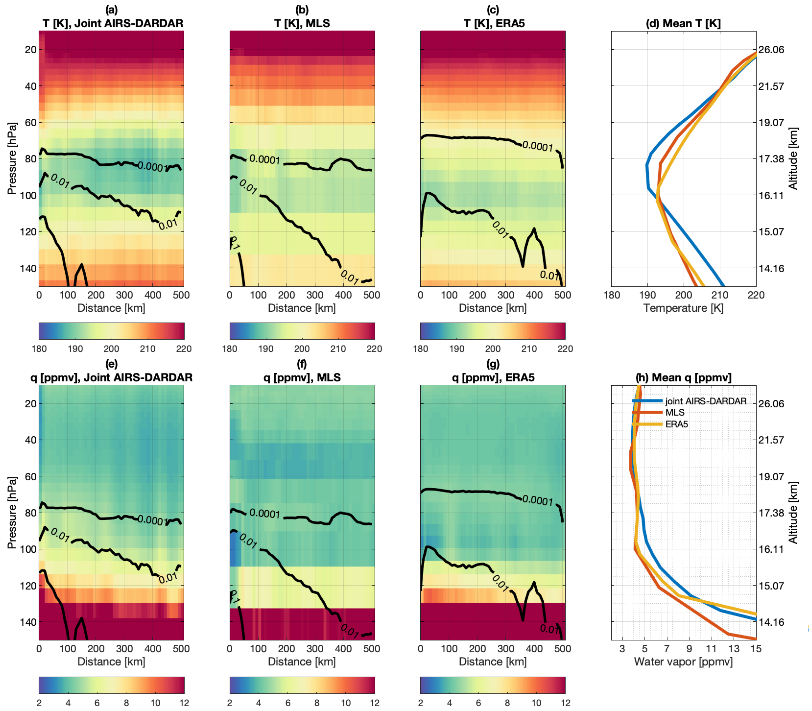

Figure 4.7: Cyclone-centered composites of temperature $[\mathrm{K}]$, water vapor $[\mathrm{ppmv}]$, and ice water content $[\mathrm{g/m^3}]$. Temperature (a) and water vapor (e) from the joint AIRS-DARDAR retrieval; the sample counts are shown in Fig. 4.5 (b). Temperature (b) and water vapor (f) from the MLS v4.2 product; the sample counts are shown in Fig. 4.1 (c) and Fig. 4.5 (a). The IWC is from the DARDAR-Cloud; the sample density is shown in Fig. 4.1 (a) Temperature (c) and water vapor (g) from the ERA5 product sampled at the same locations as (a,e). Mean temperature (d) and water vapor (h) profiles from the different datasets.

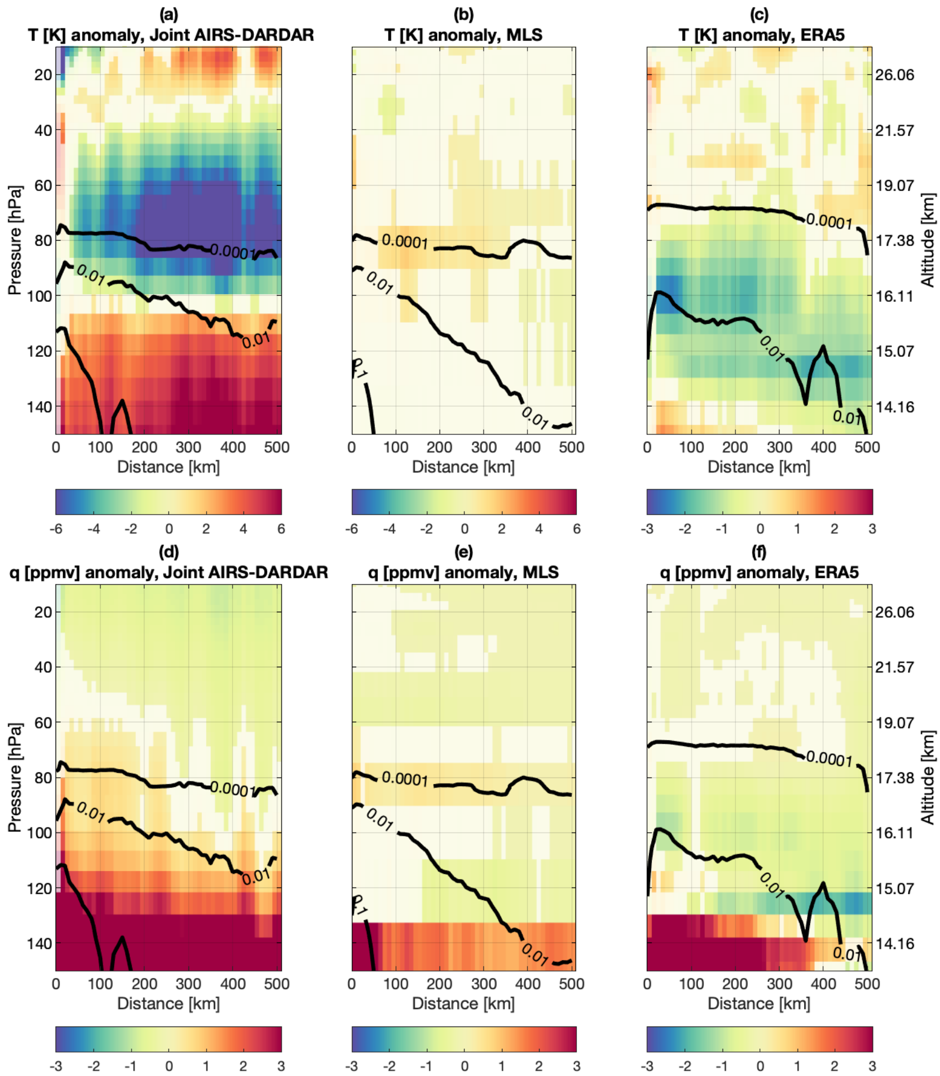

Figure 4.8: Cyclone-centered composites of temperature and water vapor anomalies. Anomalies below the 99% confidence level are set to be transparent. (a,d) Similar to Fig. 4.7 (a,e) but after subtracting the climatologies of temperature from the AIRS L2 product and water vapor from the MLS v4.2 product, respectively. (b,e) Similar to Fig. 4.7 (b,f) but after subtracting the climatologies of temperature and water vapor from the MLS v4.2 product. (c,f) Similar to Fig. 4.7 (c,g) but after subtracting the climatologies of temperature and water vapor from ERA5.

radiation in forming the retrieved temperature pattern. The thick cloud layers may absorb incoming solar radiation to heat the cloud top while attenuating emission from the warm surface to cool the atmospheric layers above the cloud. These expected cloud radiative effects agree with the signs of temperature anomalies and will be further examined in Section 4.5. On the other hand, Rivoire et al. [2020] pointed out that cloud radiative cooling only partly explains the cooling tendency above tropical cyclones. Other mechanisms at play may include the adiabatic expansion [Holloway and Neelin, 2007] in convective overshoots [Robinson and Sherwood, 2006] and the outward branches of secondary circulation [Rivoire et al., 2020, Schubert and McNoldy, 2010].

It is also interesting to find that the temperature anomaly is stronger above non-overshooting clouds (TTL-OTHERs) than over DCC-OTs or NTTLs (Fig. 4.9 (a,c)). This finding suggests a potential linkage between the temperature anomaly and the formation of TTL clouds. For example, one plausible explanation is that the cooling of air above cyclones promotes the formation of thicker TTL clouds by favoring water vapor deposition onto ice particles, as seen in Fig. 4.9 (d) and Fig. 4.10 and discussed in Section 4.3.3.2.

We note that the significant temperature anomaly pattern identified by the synergistic retrieval is not found in either MLS or ERA5. Livesey et al. [2017] have documented that MLS temperature retrievals are particularly susceptible to cloud contamination, while Schwartz et al. [2008] note that this issue cannot be effectively screened out by the $status$ flag of the MLS product. Therefore, the MLS temperature product may not be able to observe the pattern of temperature anomaly.

By comparing ERA5 (Fig. 4.7 (c) and Fig. 4.8 (c)) to the synergistic retrieval (Fig. 4.7 (a) and Fig. 4.8 (a)), we find that although ERA5 produces a higher cloud top (marked by 10^{-4} $\mathrm{g/m^3}$ IWC contour) than the DARDAR observation, it generally underestimates TTL cloud ice. ERA5 also exhibits a cold anomaly but places it at lower altitudes compared to the synergistic retrieval, which is partly attributable to different radiative heating signatures due to differences in cloud ice. Previous studies [Wright et al., 2020] have also found large discrepancies in the upper-tropospheric temperature and tropical high clouds among reanalysis products, likely due to convective parameterization [Takahashi et al., 2016, Wright et al., 2020].

4.3.3.2 Water Vapor

Using the synergistic retrieval, Fig. 4.8 (d) shows that both hydration and dehydration can occur above cyclones. Hydration is found below 80hPa, especially near the cyclone center, while dehydration is found above 60hPa. This finding is consistent with MLS observations (Fig. 4.8 (e)), even though the synergistic retrievals are performed above thick upper-tropospheric clouds while the selected MLS observations are high-cloud free.

We note that the synergistic retrieval does not have sufficient vertical sensitivity to fully resolve the vertical distribution of water vapor, due to the smearing effect of the averaging kernel discussed in Appendix 4A. Nevertheless, the retrieval is sensitive to the spatial variability of the column integrated water vapor (CIWV), which has been validated by Chapter 3 and in Appendix 4A. The retrieved CIWV above 16 km is shown in Fig. 4.10 (a, b) as a function of radial distance from the cyclone center. Therefore, we focus on the horizontal variability of CIWV above cyclones, which can be more confidently detected by the synergistic retrieval, to disclose overall hydration or dehydration above 16 km.

The synergistic retrieval detects a decreasing CIWV with increasing radial distance (Fig. 4.10 (a,b)). Significant hydration occurs near the cyclone center, increasing the CIWV by up to 0.18 $\mathrm{g/m^2}$ ($\sim$ 9%), while dehydration occurs around a distance of 375 km. In MLS, the CIWV does not substantially differ from the climatology, possibly because MLS samples large, high-cloud free areas.

The (de)hydration impact of cyclones is classified after isolating DCC-OTs, TTL-OTHERs, and NTTLs. As depicted in Fig. 4.10 (a,b), significant dehydration is only found above non-overshooting TTL clouds, while significant hydration is found above overshooting clouds and non-TTL clouds. DCC-OTs increase the CIWV above 16 km by up to 0.4 $\mathrm{g/m^2}$, which is equivalent to 20 % of the climatological value. It suggests that overall the air above cyclones is hydrated by convection, especially overshooting convection that penetrates the base of the TTL. The non-overshooting TTL clouds (TTL-OTHER), however, are found to be associated with a drier environment, possibly due to the deposition of water vapor onto ice particles in colder temperatures (as suggested by Fig. 4.8 (a) and Fig. 4.9 (a,c)).

The occurrence frequency of thick upper-tropospheric clouds (AIRS FOVs being colder

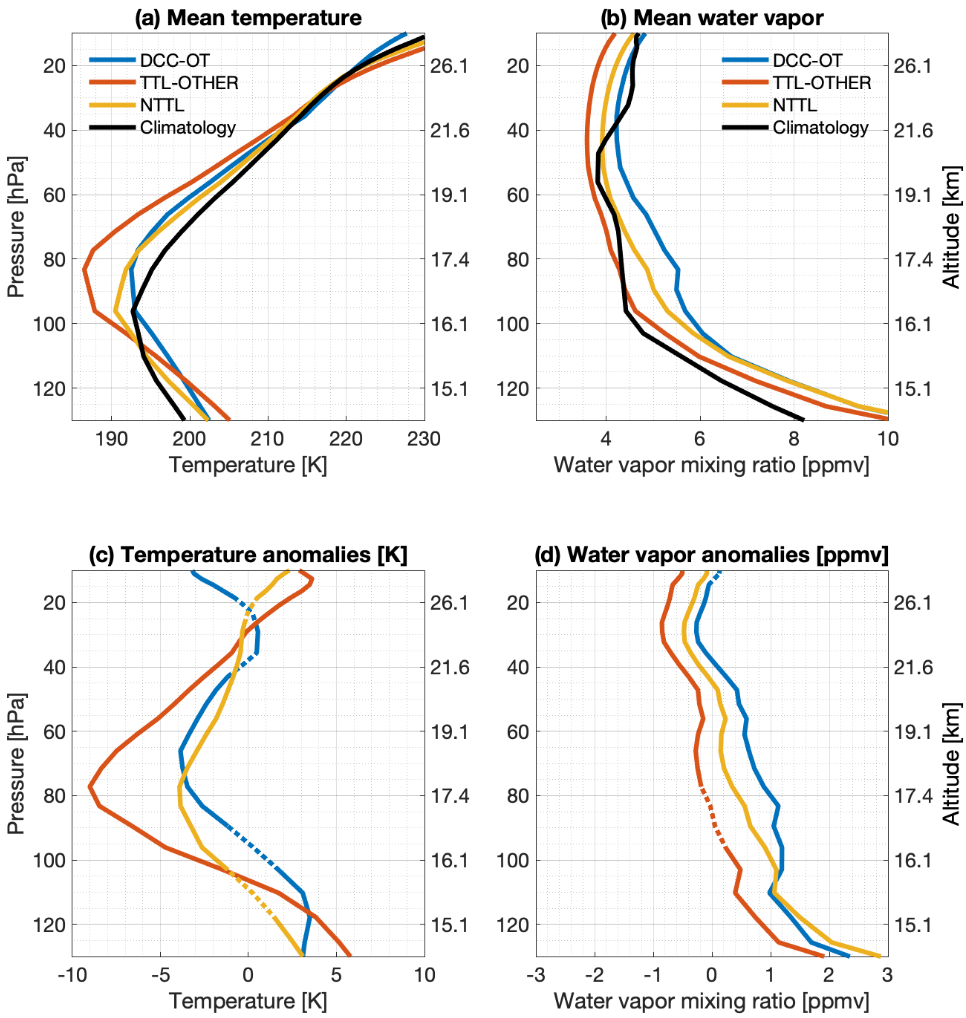

Figure 4.9: The mean (a) temperature $[\mathrm{K}]$ and (b) water vapor $[\mathrm{ppmv}]$ profiles above cyclones, for overshooting TTL clouds (DCC-OTs, blue), non-overshooting TTL clouds (TTL-OTHERs, orange), and non-TTL clouds (NTTL, yellow), along with the climatology (black). (c,d) the same as (a,b), but for anomalies with respect to the climatology.

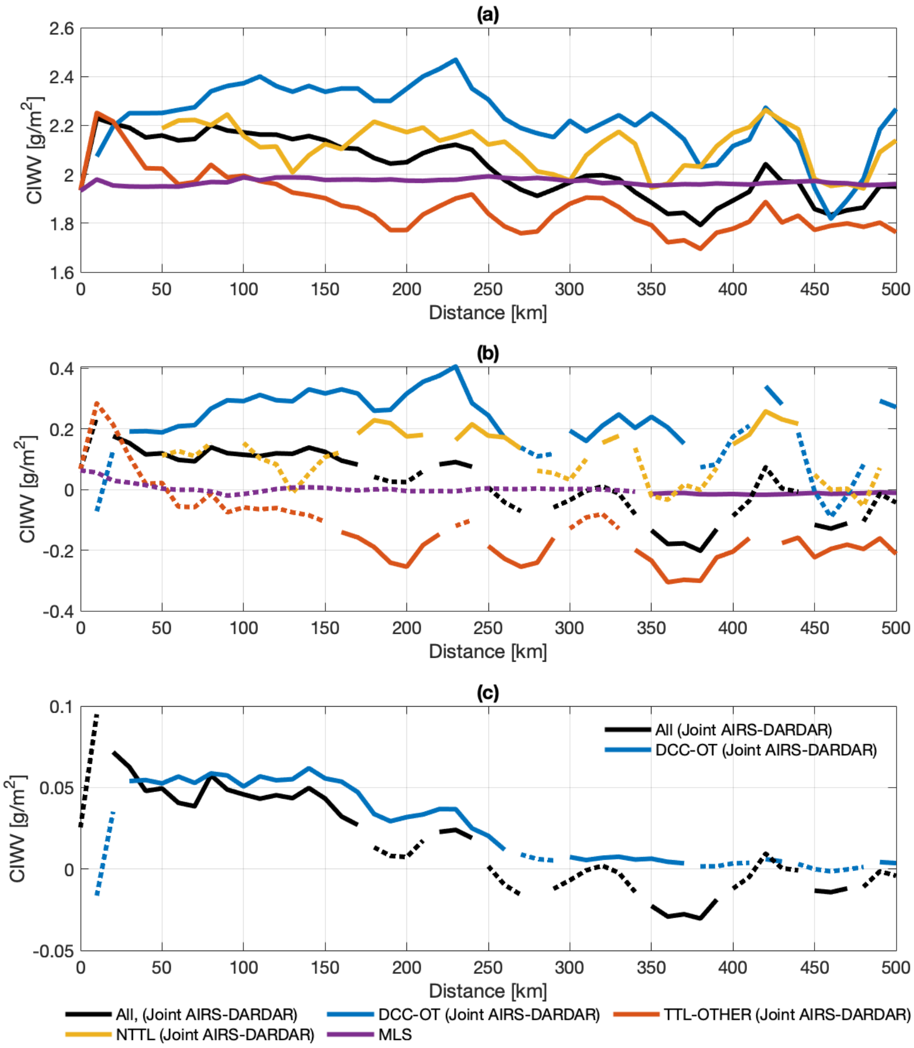

Figure 4.10: (a) Column integrated water vapor (CIWV) above 16 km from the joint AIRS-DARDAR retrieval (black) and MLS (purple). Samples retrieved by the synergistic retrieval are separated into overshooting TTL clouds (DCC-OT, blue), other non-overshooting TTL clouds (red), and non-TTL clouds (yellow). Solid curves show the statistically significant (99% confidence level) anomalies while dashed curves are not statistically significant at the 99% level. (b) Same as (a) except for the anomaly in CIWV. (c) Contributions to the CIWV anomaly from thick upper-tropospheric clouds (BT_{1231}<230 K, black) and DCC-OTs (blue).

than 230 K), above which the synergistic retrieval is conducted, is shown in Fig. 4.3 (d). The expectation of changes in CIWV contributed by thick upper-tropospheric clouds is then estimated by multiplying the CIWV anomaly (Fig. 4.10 (b)) by the occurrence frequency of these clouds (Fig. 4.3 (d), blue and orange areas). Figure 4.10 (c) shows that the CIWV above cyclones is expected to be around 0.05 $\mathrm{g/m^2}$ (1.5%) larger than the climatology within a 150 km radius of the cyclone center, and to be as much as 0.03 $\mathrm{g/m^2}$ (0.9%) smaller at a distance of 375 km. On average, the stratospheric column above thick upper-tropospheric clouds within 500 km of cyclone centers is 0.014 $\mathrm{g/m^2}$ moister than the climatology. A similar calculation is performed for DCC-OTs, using the occurrence frequency of DCC-OTs shown by the blue area in Fig. 4.3 (b). It is found that DCC-OT alone increases the mean CIWV above tropical cyclones by 0.024 $\mathrm{g/m^2}$, which is around 0.7 $\%$ of the climatological value.

In summary, hydration is found to result from overshooting convection, which injects water substance directly. The moisture injected by overshoots hydrates the surrounding environment so that the cloud-free TTL (NTTLs) also shows higher CIWV compared to the climatology. However, at locations away from overshoots, we find that overflow or pre-existing clouds in the TTL are associated with a colder and drier environment, potentially due to water vapor deposition onto ice particles.

4.4 Radiative effects

In the context of this paper, we have defined the lower boundary of the TTL to be the clear-sky level of zero-radiative heating (LZRH). Radiative heating rates in the TTL are crucial, for instance, to the cross-tropopause transport of water vapor, as they indicate the diabatic ascent of air parcels across isentropic surfaces to the stratosphere. While the ascending motion that prevails in the tropical lower-stratosphere is largely driven by dissipating waves [Holton et al., 1995, Plumb, 2002], it is found that TTL clouds can heat the air through infrared radiation and is important to explain the mass flux to the stratosphere [Corti et al., 2006, Yang et al., 2010]. Therefore, we are interested in how radiative heating rates are perturbed above tropical cyclones and whether this helps retain the moisture anomaly in the TTL.

Moreover, as indicated by the close alignment of cloud boundary and temperature anomalies, cloud radiative effects may have played a role in forming the temperature anomalies seen in Fig. 4.8. Therefore, a cyclone-centered composite of radiative heating rates is constructed using the CloudSat 2B-FLXHR-LIDAR product to help address these questions.

The cloud radiative effect, measured by the radiative heating rate difference between all-sky and clear-sky overpasses, is shown as a function of pressure level and radial distance from the cyclone center in Fig. 4.11 (c,d). Only daytime samples (overpasses at 13:30 local solar time) are used to exclude the lack of shortwave heating during the nighttime. We identify the LZRH in the heating rate profiles as the level where heating rates change from negative to positive. Note that there is no LZRH identified under two conditions: in Fig. 4.11 (a,c) when the longwave heating rate is entirely negative in the TTL, and in Fig. 4.11 (b,d,e) when the net heating rate is entirely positive.

In the longwave, Fig. 4.11 (c) shows that clouds generally produce positive perturbations inside the clouds (below 200hPa) but strong cooling at the atmosphere near and above the cloud top (marked by the 0.01 $\mathrm{g/m^3}$ IWC contour). Figure 4.11 (d) shows that this cloud top longwave cooling effect is offset by the shortwave effect. The compensation between longwave and shortwave leads to a net cloud radiative cooling effect in the layers above the cloud top but a net cloud radiative heating effect below the cloud top. These effects shift the clear-sky LZRH to higher altitudes, suppressing diabatic ascent in the TTL.

The cloud radiative heating composited here, particularly the in-cloud heating (below 0.01 $\mathrm{g/m^3}$ IWC contour) and cloud-top cooling feature (above 0.01 $\mathrm{g/m^3}$ IWC contour), corroborates the temperature structure retrieved using the synergistic retrieval method (Fig. 4.8 (a)). It is also consistent with the finding of Rivoire et al. [2020] based on an analysis of COSMIC data, who noted a cooling tendency above 100hPa that is partially attributable to radiative effects.

Fig. 4.11 demonstrates that the qualitative structure of cloud radiative heating/cooling effects change little with radial distance from the cyclone center. This insensitivity, however, hides the distinct radiative effects of different types of clouds. For instance, it is well known that thin cirrus clouds absorb longwave emission from the surface and warm the air

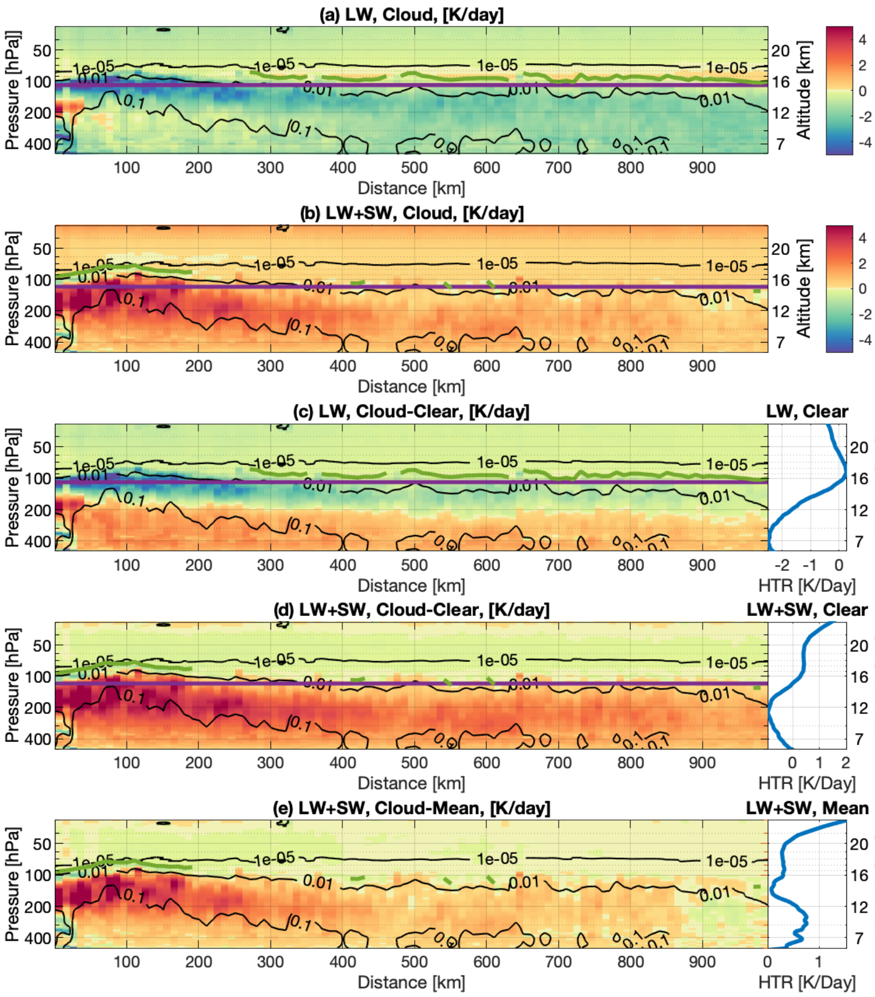

Figure 4.11: Cloud radiative heating $[\mathrm{K/day}]$ as a function of distance to cyclone center. (a) Longwave and (b) net (longwave + shortwave) radiative heating rates from CloudSat 2B FLXHR-LIDAR. (c,d) Same as (a,b) but for cloud radiative effects, which are defined as the differences between all-sky heating rates and the mean clear-sky heating rate (blue curve in the right panel). (e) Same as (d) but for net radiative heating anomalies, which are defined as the differences between all-sky heating rates and the mean all-sky heating rate. Black contour lines show the DARDAR ice water content $(\mathrm{g/m^3})$. The Magenta line marks the clear-sky LZRH. The green line marks the cloudy-sky LZRH, determined as the vertical position where heating rate changes from positive to negative.

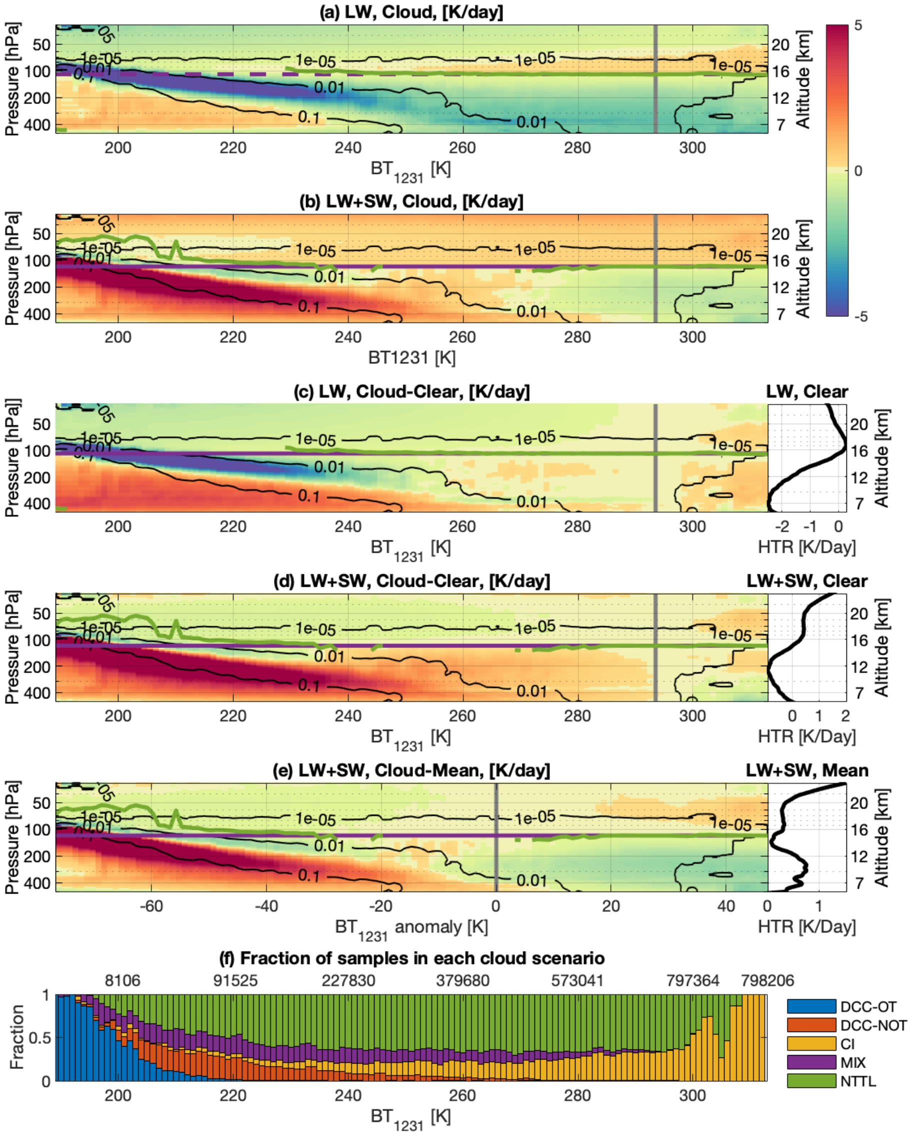

Figure 4.12: Cloud radiative heating rates $[\mathrm{K/day}]$ as a function of window band radiance, BT_{1231}, from collocated AIRS L1B observation. (a) Longwave and (b) net (longwave + shortwave) radiative heating rates from CloudSat 2B FLXHR-LIDAR. (c,d) Same as (a,b) but for cloud radiative effects, which are defined as the differences between all-sky heating rates and the mean clear-sky heating rate (black curve in the right panel). (e) Same as (d) but for net radiative heating anomalies, which are defined as the differences between all-sky and the mean all-sky cyclone overpass (black curve in the right panel). (f) The proportion of samples in each cloud category (classified in Section 4.3.1) to all cloudy overpass samples. The numbers on the top indicate the number of cloudy samples with BT_{1231} colder than the corresponding temperature marked at the bottom. Black contour lines show the DARDAR ice water content $(\mathrm{g/m^3})$. The Magenta line marks the clear-sky LZRH. The green line marks the cloudy-sky LZRH, determined as the vertical position where heating rate changes from positive to negative.

locally (e.g., Fig. 5 (c) of Rivoire et al. [2020]), although this type of effect is not evident anywhere in Fig. 4.11 (c). Recognizing that cloud types can be differentiated by cloud optical depth and that the window band radiance (BT_{1231}) is sensitive to cloud optical depth over tropical ocean FOVs, we composite cloud radiative heating with respect to BT_{1231} to characterize the radiative effects of different types of clouds.

The CloudSat/DARDAR cloud profile is paired with the nearest AIRS spectra. The AIRS FOVs evaluated here are limited to those with scanning angles less than 14 degrees, which has a negligible (<3$\%$) effect on optical depth and those with CloudSat samples locations fall within their ground footprints (13.5 km). A composite of all-sky radiative heating rates over every 1-K bin of BT_{1231} is shown in Fig. 4.12, along with differences relative to clear sky conditions.

Fig. 4.12 shows that different regimes of cloud radiative effects are well differentiated by BT_{1231}. When BT_{1231} is colder than 230 K (indicating thick upper tropospheric clouds, as discussed in Section 4.3), net radiative cooling is observed in the TTL. This net cooling is largely caused by longwave cooling above DCC cloud tops (indicated by IWC contours in Fig. 4.12). Note that this BT condition (colder than 230 K) occurs in more than 50 $\%$ of overpasses within a 300 km radius of the cyclone center (Fig. 4.3 (d)), indicating that the TTL is dominated by radiative cooling within this range. In this cloud regime, the cloud effect lifts the LZRH to higher altitudes, reaching 19.5 km when BT_{1231} is around 200 K. When BT_{1231} is between 240 K and 280 K, noticeable heating emerges near the cloud top (compare Fig. 4.12 (a) and (b)), attributable to the deeper penetration of solar radiation into the less opaque cloud layer. When BT_{1231} is greater than 294 K (the clear-sky climatological mean value), TTL heating is evident. This TTL heating is accompanied by a substantial increase of CI (cirrus) scenes with increasing BT_{1231} as shown in Fig. 4.12 (f), which suggests the contribution of thin cirrus in the TTL heating as mentioned above.

Furthermore, we compute the net heating anomaly with respect to the all-sky climatology. The all-sky net heating anomaly is then shown as a function of the BT_{1231} anomaly, which is also defined with respect to the all-sky average, in Fig. 4.12 (e). It is clear that cloud effects on TTL heating rates above 16 km are well-differentiated by BT_{1231}: cooling when the BT_{1231} anomaly is negative and heating when the BT_{1231} anomaly is positive. Given that a negative BT_{1231} anomaly prevails within 1000 km of the cyclone center (see the black line in Fig. 4.3 (d)), it is no wonder that Fig. 4.11 generally shows TTL cooling above tropical cyclones.

The prevalence of TTL radiative cooling in Fig.4.12(c,d) suggests that the diabatic ascent that normally (climatologically) occurs within the TTL is greatly suppressed by cloud radiative effects in a 2000 km $\times$ 2000 km domain surrounding tropical cyclone centers. A hydrated air parcel above a cyclone has to be advected further away from the cyclone centers to experience radiative heating and ascend to the stratosphere.

Finally, it is worth noting a few caveats of the cloud radiative effect assessed here. As the cloud radiative effect is measured by the difference in radiative heating between all-sky and clear-sky conditions, the result is subject to differences in surface emissions and thermodynamic conditions between the clear-sky and all-sky situations. We cannot quantify how much of the TTL cooling (as shown in Fig. 4.12 (d,e)) is directly attributable to clouds because large anomalies in temperature and water vapor (as shown in Fig. 4.8) also exist above tropical cyclones. It is unclear how much these non-cloud variables account for the radiative heating anomalies shown in Fig. 4.11 and 4.12. Moreover, the CloudSat radiative heating data used here may be subject to errors because their calculation is based on the ECMWF forecast which does not fully capture the above-cyclone temperature and water vapor perturbations (see Fig. 4.8). It is therefore useful to examine the heating rate change above these tropical cyclones using collocated observations of cloud, temperature, and water vapor profiles from our synergistic retrieval.

4.4.1 Heating rate decomposition

Large temperature and water vapor anomalies in the TTL above tropical cyclones (as depicted in Fig. 4.8) are detected using the joint AIRS-DARDAR retrieval method. Here, using the radiative transfer model RRTM [Iacono et al., 2000], the radiative effects of the cloud, temperature, and water vapor anomalies are isolated in Fig. 4.13. The shortwave effects of temperature and water vapor are not shown because they are negligible compared to the longwave effects.

Following the Partial Radiative Perturbation approach [Wetherald and Manabe, 1988], we measure the radiative effect of a variable by differencing the RRTM computations with perturbed and unperturbed values of this variable. For instance, the radiative effect of cyclonic clouds is measured as:

$$dHTR(c) = HTR(c, t0, q0) - HTR(c0, t0, q0) \tag{4.1}$$

Here, HTR denotes the instantaneous heating rate profile and is computed using RRTM, and c, t, and q denote cloud, temperature, and water vapor profiles from the cyclone samples, respectively. Note that for the t and q profiles, only the portions above 16 km are of concern and replaced in the PRP computation. Variables with subscript 0 denote values from the all-sky climatology. The mean instantaneous longwave and net radiative heating rate profiles for DCC-OTs, TTL-OTHERs, and NTTLs are shown in Fig. 4.13. The radiative effects of temperature and water vapor are examined in both all-sky conditions, denoted by the subscript cld in Fig. 4.13 (g,h), and clear-sky conditions ($c = 0$), denoted by the subscript clr in Fig. 4.13 (c,d).

By comparing Fig. 4.13 (a) and (e), we find that the total net radiative effect, $dHTR_{net}(c, t, q)$, is dominated by clouds. The sign and magnitude of the cloud radiative effect are consistent with our previous conclusion, namely a cooling effect at the cloud top as indicated by a cold BT_{1231} anomaly (Fig. 4.12 (a,e)). The cloud longwave cooling effect around 90 hPa is much larger above DCC-OTs due to higher cloud ice water content near this level.

As seen in Fig. 4.13 (g,h), above 80hPa where cloud ice diminishes, the all-sky radiative effects of anomalies in temperature and humidity become more important. Temperature modulate longwave emission in ways that damp the temperature anomalies (compare Fig. 4.13 (g) to Fig. 4.9 (c)). For water vapor, a moistening at the cold point increases thermal emissivity, which leads to cooling at the cold point and heating at lower levels. Therefore, TTL hydration above DCC-OTs and NTTLs leads to radiative cooling in the TTL. Assuming a similar pattern in thermodynamic anomalies to Fig. 4.9 (c,d) in the clear-sky, we compute the radiative effects of temperature and water vapor above 80 hPa in the clear-sky (Fig. 4.13 (c,d)) and find that they are similar to the all-sky results.

Despite the limited vertical resolution of the water vapor retrieval, as discussed in Appendix 4A, it is unambiguous that TTL hydration leads to radiative cooling. It suggests that

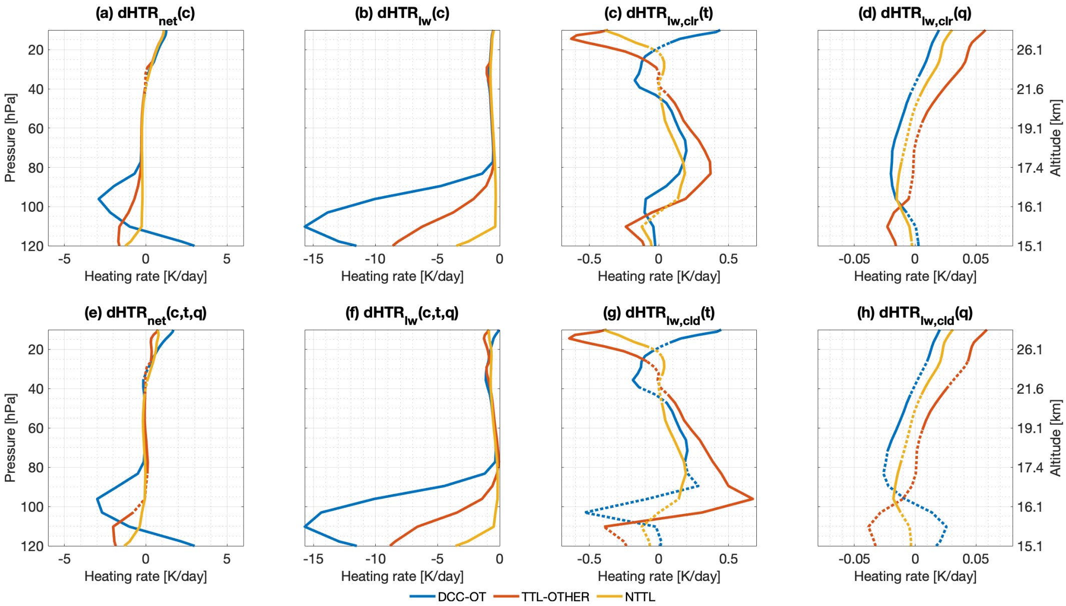

Figure 4.13: The radiative heating effects of cloud, temperature, and water vapor. (a) The net effects of cloud, $dHTR_{net}(c)$. (b) The longwave effects of cloud, $dHTR_{lw}(c)$. (c) The longwave effects of temperature under clear-sky conditions, $dHTR_{lw,clr}(t)$. (d) The longwave effects of water vapor under clear-sky conditions, $dHTR_{lw,clr}(q)$. (e) The net effects of cloud, temperature and water vapor, collectively, $dHTR_{net}(c,t,q)$. (f) The longwave effects of cloud, temperature, and water vapor, collectively, $dHTR_{lw}(c,t,q)$). (g) The longwave effects of temperature under cloudy-sky conditions, $dHTR_{lw,cld}(t)$. (h) The longwave effects of water vapor under cloudy-sky conditions, $dHTR_{lw,cld}(q)$.

moisture above overshooting convection radiatively cools the layer, thus constraining the moist air from diabatically ascending to higher altitudes. This finding is consistent with the robust radiative cooling seen above cyclones in Fig. 4.12.

4.5 Conclusions

In this study, we aim to understand the impacts of tropical cyclones on thermodynamic conditions in the TTL using multiple instruments aboard the A-Train satellites. We use a TC-overpass product to composite multiple observation products relative to 947 tropical cyclone center locations over the northern part of the West-Pacific region to ascertain the effect of cyclones. To address the lack of reliable observations of temperature and water vapor when thick convective clouds are present, a retrieval scheme proposed by Chapter 2 is improved by incorporating cloud properties measured by active sensors to retrieve the above-cyclone temperature and water vapor profiles simultaneously.

This study finds that tropical cyclones substantially increase TTL clouds. These TTL clouds occur frequently above tropical cyclones, mostly as non-convective high clouds (type CI) (Fig. 4.3 (b)). This distribution of high clouds is consistent with in-situ aircraft observations [e.g., Jensen et al., 2013]. Our finding emphasizes that the occurrence of TTL cloud is 37.2% on average (Fig. 4.2 (a) and Fig.3(a)) within the 2000 km $\times$ 2000 km cyclone-centered composite domain, highlighting the importance of tropical cyclones in generating TTL clouds. In contrast to the horizontally extensive occurrence of TTL cloud cover, TTL cloud ice is most concentrated near the cyclone center (Fig. 4.2 (c) and Fig. 4.3 (a)), as a result of direct convective overshooting and detrainment (Fig. 4.3 (c)). Furthermore, we find that the northwestern quadrant of the composite domain is less impacted by cyclones Fig. 4.2 (b,j). There is also a persistent southwest preference in TTL cloud ice and DCCs.

The results produced by the synergistic retrieval (Fig.10 (b)) suggest that cyclones mostly hydrate the atmospheric column above them. Above overshooting deep convective clouds, the column-integrated water vapor above 16 km altitude is found to be 40 $\%$ higher than the local climatology (Fig. 4.10 (b)). Substantial hydration is also found above clouds located beneath 16 km (NTTL). We suspect that this is likely from advected moist plumes from overshooting injection, though we are unable to prove these suspicions at this time. After isolating different cloud categories, dehydration is only found above non-overshooting TTL clouds (TTL-OTHERs) which are coincidently associated with colder temperatures than other cloud categories (Fig. 4.9 and 4.10). The coexistence of dehydration (as opposed to the moistening above other cloud categories), cold anomalies, and non-overshooting TTL clouds suggests that in this situation water vapor is likely deposited onto ice particles.

A noticeable pattern of vertically-oscillating temperature anomalies, which lifts the cold-point tropopause level to higher altitudes, is found above cyclones. After investigating the cloud radiative effects in Section 4.4, we find that the signs of the temperature anomaly agree well with cloud effects on radiative heating rates, for example, the in-cloud warming (below the 0.01 $\mathrm{g/m^3}$ IWC contour in Fig. 4.8 (a) and Fig. 4.12 (d)) due to shortwave heating and cloud-top cooling due to longwave cooling. Environmental cooling above clouds may also facilitate the formation of TTL clouds that deplete moisture from the detrainment of tropical cyclones, as indicated by the drier TTL over non-overshooting clouds. The cooling effect of tropical cyclones on cold-point temperatures also implies the importance of deep convection in modulating the stratospheric water vapor, so that a strong linkage between stratospheric water vapor and cold-point temperature, as noted by Randel and Park [2019], cannot preclude the role of convection in water vapor variability.

By comparing the nearest thermodynamic profiles from the ERA5 reanalysis (Fig. 4.8 (c,f)) to the synergistic retrieval (Fig. 4.8 (a,d)), we find that the cold anomaly in ERA5 is at a lower altitude, which is partially attributable to biases in cloud ice in the reanalysis. The moistening signals around 80 hPa, as detected by the synergistic retrieval and MLS (Fig. 4.8 (d,e)), are not shown in ERA5. These results suggest that the above-cyclone water vapor in reanalysis products may be susceptible to the ability of the convective parameterization in the model to simulate cloud ice and temperature [Wright et al., 2020].

Furthermore, we find that the cloud radiative effect is well-differentiated by BT_{1231}. Clouds heat the TTL via radiation when BT_{1231} shows a warm anomaly and cool the TTL when BT_{1231} shows a cold anomaly. Radiative cooling prevails above DCCs and thick anvils, which greatly reduce BT_{1231}. Radiative warming becomes more noticeable away from the cyclone center over thin cirrus. The radiative cooling anomaly further impacts the diabatic heating budget above tropical cyclones, suppressing diabatic ascent and air mass transport across isentropic surfaces to higher altitudes. It remains unclear how this suppressed diabatic ascent, together with the strong horizontal divergence created by the pressure gradient above the cyclone, affects stratosphere-tropopause exchange and the water vapor budget. To elucidate this effect in the trajectory modeling in future work, it will require the use of instantaneous radiative heating computed from deep convection-perturbed TTL thermodynamic conditions (temperature, humidity, and cloud), as opposed to climatologic or reanalysis heating profiles that do not properly represent the convective perturbations.

Finally, we would like to highlight the advantages of the synergistic method in retrieving the above-cloud thermodynamic conditions. This method takes advantage of collocated infrared hyperspectra and active sensors and is capable of retrieving temperature and water vapor under overcast cloud conditions. These features are highly complementary to other datasets, including MLS v4.2 and AIRS L2 v6, that are limited to clear-sky conditions. So far, this approach has only been applied to limited samples in the vicinity of tropical cyclones. It can be applied to other tropical and extra-tropical convective events, with potential implementation in other hyperspectral infrared sounders, such as IASI (Infrared Atmospheric Sounding Interferometer), CrIS (Cross-track Infrared Sounder), IRS (Infrared Spectrometer), and GIIRS (Geostationary Interferometric Infrared Sounder), to provide thermodynamic information over deep convective clouds on a global scale in future research.

4.A Joint AIRS-DARDAR retrieval algorithm

Chapter 2 applied a cloud-assisted retrieval to AIRS L1B infrared radiance from FOVs filled with deep convective clouds, assuming a blackbody cloud top. This method retrieves atmospheric temperature and humidity profiles above the cloud top as described in Section 4.2.1 and is especially advantageous for overcast conditions during tropical cyclone events. An updated version of this retrieval method has been validated by Chapter 3 using simulation experiments and is adopted here. We briefly describe this retrieval method below and interested readers can find more details of this retrieval method from Chapter 3.

4.A Joint AIRS-DARDAR retrieval algorithm

In this method, we retrieve atmospheric states x that include temperature, humidity, and ice water content (IWC) as an optimal estimation [Rodgers, 2000] that combines the a $priori$ of x and the observation vector, y. The relationship between the state vector and the observation vector is expressed as:

$$\begin{aligned} y &= F(x_0) + \frac{\partial F}{\partial x}(x - x_0) + \varepsilon \\ &= y_0 + K(x - x_0) + \varepsilon \end{aligned} \tag{4.2}$$

Where F is the forward model, K is the J453acobian matrix, which is a first-order linear approximation of F, and ε is the residual. x_0 is the first guess, for which we use the mean of the a $priori$. Following the synergistic retrieval method (Chapter 3), additional observation vectors are added, so that y is formed as $[y_{rad}, y_{iwc}, y_{atm}]$. y_{rad} is the infrared hyperspectra from the AIRS L1B product, for which 1109 channels are selected, based on the radiometric quality of each channel. This rigorous channel selection also excludes O3 absorption channels (980-1140 cm^{-1}), CH4 absorption channels (1255-1355 cm^{-1}), and shortwave infrared channels (2400-2800 cm^{-1}). y_{iwc} is a 2-km vertical IWC profile from the DARDAR-Cloud product, from 1.5 km below the DARDAR-identified cloud top to 0.5 km above it, and y_{atm} is the temperature and humidity profile from the nearest ERA5 reanalysis product (hourly, 0.25 x 0.25). The a $priori$ dataset is obtained from the AIRS L2 supplementary product from 2006 to 2016 in the Northern part of the West Pacific.

The forward model to convert the atmospheric states to y_{rad} is a radiative transfer model, the line-by-line version of MODerate spectral resolution TRANsmittance [MODTRAN 6.0 Berk et al., 2014]. To relate x to y_{iwc} and y_{atm}, the forward model and the corresponding Jacobian matrix work as a linear interpolation matrix Chapter 2 and 3.

Using the Gaussian-Newton method, the best estimate of x, $\hat{x}$, is iteratively solved as:

$$\begin{aligned} \hat{x}_{i+1} &= x_0 + (K_i^T S_\varepsilon^{-1} K_i + S_a^{-1})^{-1} K_i^T S_\varepsilon^{-1} [y - F(\hat{x}_i) + K_i(\hat{x}_i - x_0)] \\ \hat{x}_{i+1} &= x_0 + (K_i^T S_\varepsilon^{-1} K_i + S_a^{-1})^{-1} K_i^T S_\varepsilon^{-1} [y - F(\hat{x}_i)] + A(\hat{x}_i - x_0) \end{aligned} \tag{4.3}$$

Where the subscript i refers to the ith time step. S_a and S_ε are the covariance matrix of the a $priori$ dataset and the observation vector, respectively, which are constructed the same as in Chapter 3. More specifically, the S_ε for y_{iwc} is a diagonal matrix, containing the square of the posterior uncertainty of the IWC profile which is provided by the DARDAR-Cloud product at every measurement location and vertical level. The S_ε for y_{atm} is denoted as S_{atm}; it contains the square of a doubling of the root-mean-square difference between collocated ERA5 and MLS v4.2 products at every vertical level of ERA5.

The A in Eq. 4.3 is referred to as averaging kernel. Given a 'truth' state vector that $F(x_t) = y$, it links the truth state to the retrieved state, so that:

$$\hat{x} - x_0 = A(x_t - x_0). \tag{4.4}$$

Therefore, it regulates the vertical shape of the posterior estimation.

The iteration converges when:

$$(\hat{x}_{i+1} - \hat{x}_i)^T S(\hat{x}_{i+1} - \hat{x}_i) \ll N, \tag{4.5}$$

where N is the dimension of the state vector, and S is the posterior covariance matrix, which is computed combining the covariance matrix of $a\ priori$ and observation vector:

$$S = (S_a^{-1} + K^T S_\varepsilon^{-1} K)^{-1} \tag{4.6}$$

Therefore, the uncertainty in the $\hat{x}$ is equivalent to the square root of the diagonal element of the posterior covariance matrix S.

Chapter 3 used a simulation experiment to evaluate a synergistic retrieval approach that combines infrared spectra (y_{rad}) with another observation vector that includes the IWC product from collocated observation vector, denoted as y_{iwc}, and additional atmospheric observations, denoted as y_{atm}. In this simulation experiment, the 'truth' atmospheric condition is simulated from a cloud-resolving model during a tropical cyclone event. We mimic the infrared spectra from AIRS observation by adding synthetic noise to the forward model simulated infrared radiances that follow the spectral response function of AIRS. The IWC observation is simulated by perturbing the 'truth' IWC profile following the mean posterior uncertainty range provided by the DARDAR-Cloud product within 1000 km from cyclone centers. Therefore, the simulation experiment is designed to evaluate the realistic retrieval performance above thick upper-tropospheric clouds using AIRS L1B and DARDAR-Cloud products, with the same S_ε for the observation vectors.

The synergistic retrieval performed here is similar to Case 4 in Chapter 3; the only differences are in the $a\ priori$ dataset and the y_{atm}, which Chapter 3 constructed hypothetically using numerical model simulation. To examine the capacity of the retrieval method in revealing the realistic thermodynamic conditions, a simulation experiment similar to Chapter 3 is performed here, using the $a\ priori$ dataset and S_ε we introduced earlier. Fig. 4.14 shows the horizontal distribution of temperature and water vapor at 81 hPa, as well as the column-integrated water vapor (CIWV, between 100 and 70 hPa) from the simulated 'truth', the prior, the nearest ERA5 (y_{atm}), and the posterior of the retrieval. In Fig. 4.14, the posterior shows a noticeable improvement compared to the prior and y_{atm} in reducing the mean biases and root-mean-square-error (RMSE). As a result, the posterior reveals the spatial feature of the 'truth', namely a moister and colder cyclone center.

According to Eq. 4.5 and 4.6, the precision of this synergistic retrieval algorithm is given by the posterior uncertainty S, which is shown in Fig. 4.15. The posterior uncertainty is within 1 K in temperature and is around 0.5 ppmv in water vapor around 80 hPa. While the uncertainty in IWC is equivalent to the DARDAR-Cloud product, the simulation experiment conducted by Chapter 3 showed that the retrieval is able to reduce the mean biases and RMSE in collocated IWC products caused by issues such as footprint mismatch.

Compared to other current satellite observational products in the UTLS, this retrieval has several advantages. First, the relatively small sampling footprint (15km, the same as the size of the AIRS instantaneous FOV in the nadir) compared to limb-viewing sounders (>100 km) is beneficial for capturing small-scale variability directly impacted by deep convection. Second, the ability to retrieve temperature and water vapor above storms simultaneously. Third, the ability to retrieve atmospheric profiles near the cloud top. The simulation experiment conducted by Chapter 3 evidenced that the synergistic method is capable of sounding the temperature profile near and slightly below the cloud top (within cloud optical depth of 1), while other products may not perform all-sky retrieval [AIRS L2, Susskind et al., 2003] or may be degraded by cloud presence [MLS v4.2 Schwartz et al., 2008, Livesey et al., 2017].

As depicted in the simulation experiment, the synergistic retrieval reveals the spatial variation in temperature and humidity. The retrieval is sensitive to the vertical variation of temperature (Fig. 4.16 (a,b)) but is not as sensitive to the vertical variation of water vapor (Fig. 4.16 (c,d)). The coarse resolution of the water vapor retrieval is due to the smearing effect of the averaging kernel (Chapter 3). This smearing effect is illustrated in Fig. 4.16. In this test, we increase the temperature at every 20hPa interval by 5 K as shown in Fig. 4.16 (a), this corresponds to the term $x_t - x_0$ in Eq. 4.4. Similarly, the water vapor mixing ratio at every 20 hPa interval is increased by 50 $\%$ (considering the water vapor radiative effect is logarithmically scaled), as shown in Fig 4.16 (c). The responses from the averaging kernel are then calculated using Eq. 4.4, which are shown in Fig. 4.16 (b,d) for temperature and water vapor, respectively. Fig. 4.16 (a,b) shows that the retrieved temperature responds well to perturbation at different vertical ranges. However, Fig. 4.16 (c,d) shows that the fine-scale water vapor perturbation would result in vertically broad, bottom-heavy water vapor anomalies in the retrieval. Nevertheless, the retrieval determines the changes in CIWV properly to detect (de)hydration. This is verified by the tests illustrated in Fig. 4.16 (c). Here, we prescribe random hydrations or dehydrations in randomly selected 20 hPa thick layers between 20 and 100 hPa, following the same pattern in Fig. 4.16 (c), for 1000 cases. We find that the CIWV changes produced by averaging kernel approach the truth better at higher altitudes, suggesting that the retrieval is more sensitive to perturbations at higher altitudes.

To evaluate the effects of cyclones on water vapor, samples above cyclones are compared to the climatology computed from the multi-year monthly mean of MLS data at the same grid as the retrieval samples. To remove the systematic bias caused by the higher vertical resolution of the MLS product, the MLS climatology is converted to the same vertical resolution using the averaging kernel of the synergistic retrieval, following Eq. 4. The mean of the converted climatology profiles at retrieved sample locations is shown in Fig. 4.9 (b) black line, while the mean of retrieved water vapor anomalies in comparison with this converted climatology is shown in Fig. 4.8 (d) and Fig. 4.9 (d). These anomalies measure the impacts of cyclones. We note that this bias correction procedure affects the vertical structure of anomaly in water vapor, but has a negligible impact on the anomaly in CIWV. Therefore, the conclusion on the hydration and dehydration impacts as shown in Fig. 4.10

are robust.

4.B Binary classification of overshooting deep convective clouds

Similar to previous studies [Aumann and Ruzmaikin, 2013], we investigate BT of window channel at wavenumber 1231 cm^{-1} (BT_{1231}) and water vapor absorption channel at wavenumber 1419 cm^{-1} (BT_{1419}). In this section, we use collocated AIRS radiance observations and the DARDAR-Cloud product to evaluate the two metrics quantitatively and to identify the best threshold for determining the DCC-OTs.

As shown in Fig. 4.17, the distributions of BT_{1231} and ΔBT of overshooting DCCs resemble the Gaussian distribution in the intervals of [185 210] K and [-2 12] K, respectively. To find the optimized threshold for DCC-OT classification, we calculate the accuracy and the f1 score of DCC-OT classification combining $BT_{1231} <= \varepsilon_{BT}$ and $\Delta BT >= \varepsilon_{\Delta BT}$. The accuracy ($\alpha$) and the f1 score ($F1$) are defined as:

$$
\begin{aligned}
\alpha &= \frac{TP + TN}{TP + FP + FN + TN};\\
P &= \frac{TP}{TP + FP};\\
R &= \frac{TP}{TP + FN};\\
F1 &= 2 \times \frac{R \times P}{R + P};
\end{aligned}
\tag{4.7}
$$

Where the TP, TN, FP, and FN are the number of true positive, true negative, false positive, and false negative, respectively. While the P and R represent the precision and recall (equivalent with true positive rate) of this classification, the f1 score considers both by a harmonic average of the two factors.

As indicated by Fig. 4.17 (c), the accuracy of the classification gets around 0.985 when $\varepsilon_{BT} <= 204$ K or $\varepsilon_{\Delta BT} >= 2$ K. However, this high accuracy is partly a result of a small sample size from DCC-OT compared to the total. The f1 score is therefore used instead. The maximum $F1$ appears when $\varepsilon_{BT} = 203$ K and $\varepsilon_{\Delta BT} = 1$ K, although adding

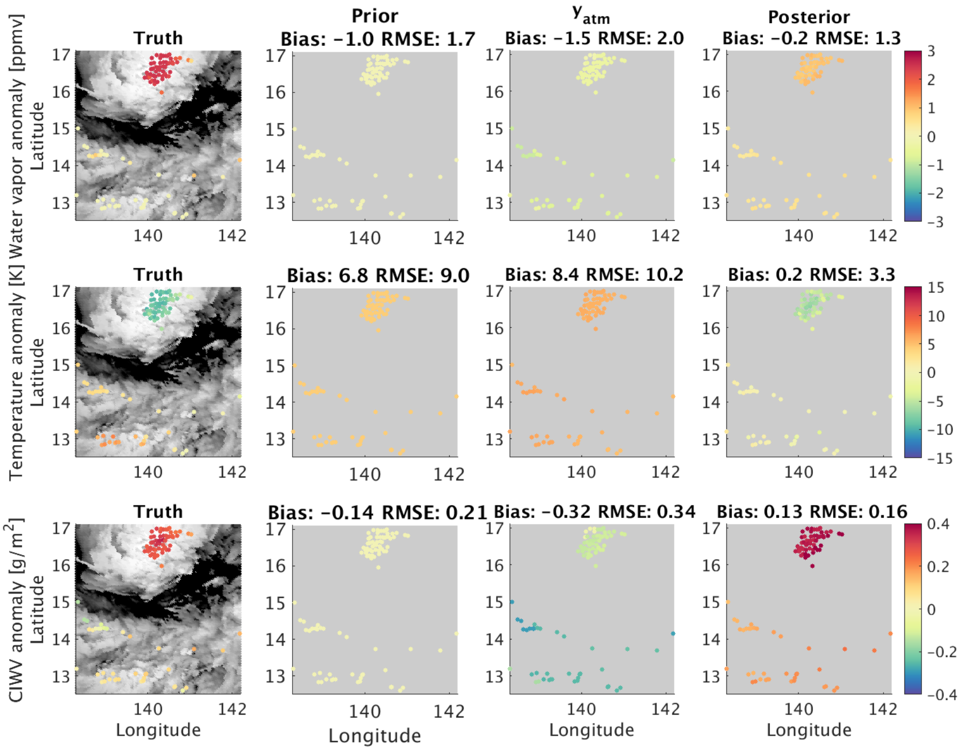

Figure 4.14: Horizontal distributions of the anomalies, defined as the deviation from the all-sky mean of the simulation field, in water vapor (in the units of ppmv, upper panels), temperature (in the units of K, middle panels) at 81hPa, and column integrated water vapor between 110 and 70 hPa (in the units of $\mathrm{g/m^2}$, lower panels). The truth fields are shown in the first column, with its background grey-shaded for BT_{1231}. The other columns show the distribution in the prior, nearest ERA5 (y_{atm}), and the posterior of the retrieval.

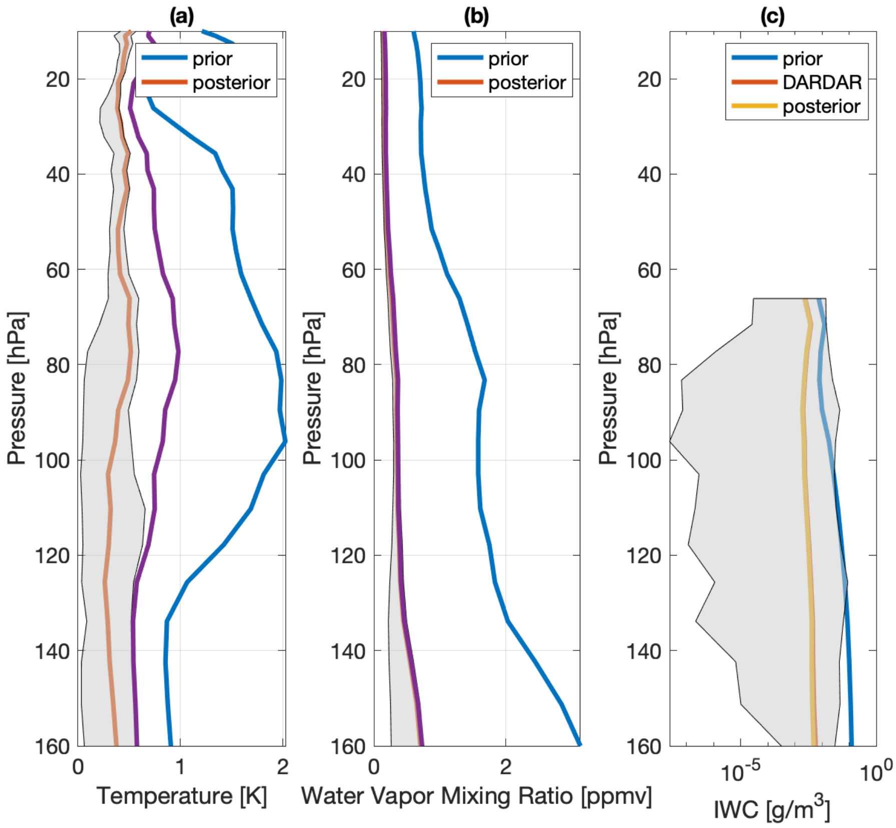

Figure 4.15: Uncertainties in temperature, water vapor mixing ratio, and IWC, estimated from the average of 2735 retrieved profiles with varied cloud top heights. Blue, red, and yellow curves show uncertainties of the prior (S_a), the ERA5 (S_{model}), and the posterior (S_{post}), respectively. The grey shaded area is the range of posterior uncertainties.

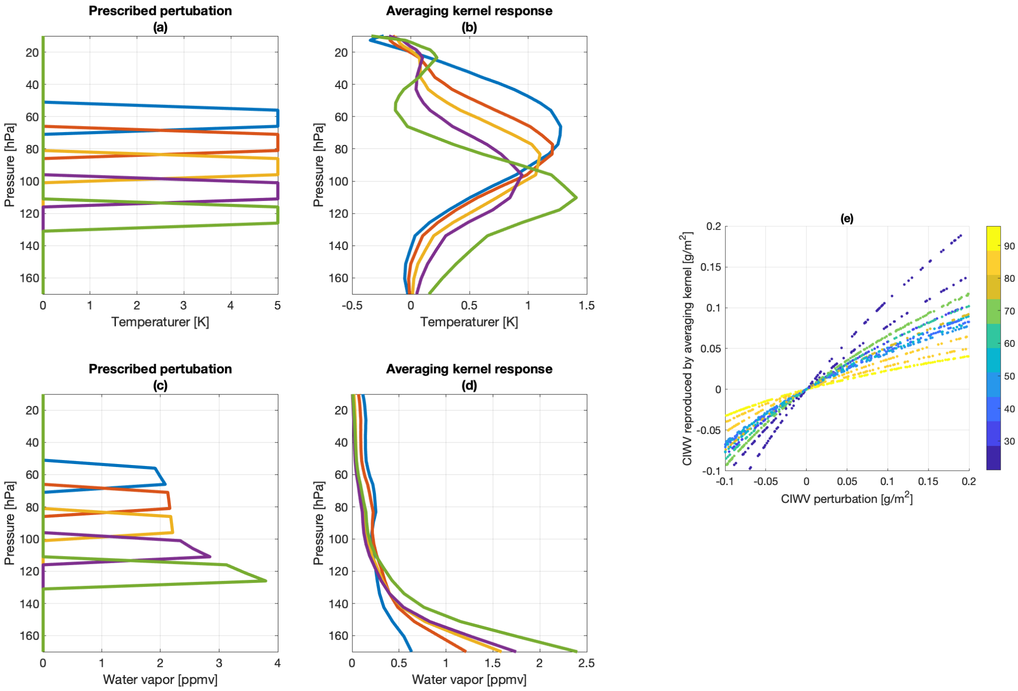

Figure 4.16: Averaging kernel responses to temperature and water vapor perturbation in thin layers. (a) Prescribed perturbation and (b) the response of averaging kernel in temperature $[\mathrm{K}]$. (c) Prescribed perturbation and (d) the response of averaging kernel in water vapor $[\mathrm{ppmv}]$. (e) CIWV perturbation $[\mathrm{g/m^2}]$ between 100 and 20 hPa reproduced by averaging kernel, color-coded for vertical pressure intervals (hPa) where the perturbation is prescribed.

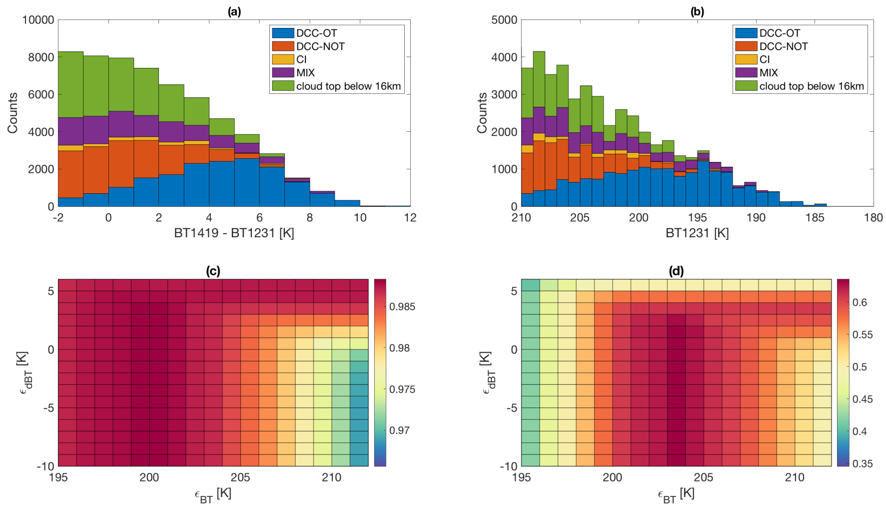

Figure 4.17: Distribution of (a) BT_{1419}-BT_{1231} and (b) BT_{1231} of AIRS FOVs under four TTL cloud categories and NTTLs (cloud top below 16 km). (c) The accuracy (Eq.1, α) and (d) f1 score ($F1$) of the DCC-OT classification using $BT_{1231} <= \varepsilon_{BT}$ and BT_{1419}-$BT_{1231} >= \varepsilon_{\Delta BT}$ criterion.

$\varepsilon_{\Delta BT}$ criterion only increase $F1$ by 0.0004 which is considered to be negligible here. Using $\varepsilon_{BT} = 203$ K leads to an FP rate at 0.008 and an FN rate at 0.323. Figure 4.17 (b) shows that the FP mainly comes from MIX and CI; their cold brightness temperature signal indicates sources from thick anvil cloud near the edge of the DCC system.

5

Final Conclusion & Future Work

In this dissertation, we use satellite observations to quantify the direct convective impacts on UTLS water vapor. To overcome the lack of observations, we develop an innovative, synergistic method to retrieve temperature, water vapor, and clouds above convective storms, combining space-borne infrared observations and cloud products, as described in Chapters 2 and 3. This method is validated with a simulation experiment in Chapter 3.

This synergistic method has several advantages in evaluating convective impacts. First, owing to a small sampling footprint compared to limb-viewing or occultation instruments, it can reveal small-scale variations in the thermodynamic fields above convective events. Second, with the benefits provided by collocated active sensors, it can identify impacts of convective overshoots from deep convection, as seen in Figure 4.10. Third, it is sensitive to atmospheric profiles near the cloud top, while other products may not perform all-sky retrieval [AIRS L2, Susskind et al., 2003] or may be affected by cloud presence [MLS v4.2 Schwartz et al., 2008, Livesey et al., 2017].

In Chapter 4, we apply the synergistic method to tropical cyclone events to evaluate their role in generating overshooting deep convective clouds in the tropics [Romps and Kuang, 2009]. Using multiple instruments aboard A-Train satellites, we develop the first infrared hyperspectra-based observational dataset of temperature and water vapor profiles above deep convective clouds.

The constructed dataset stresses the importance of tropical cyclones in TTL with respect to overshooting cloud ice, generating a horizontally extensive TTL cloud cover, and creating a strong, oscillating pattern of temperature anomalies in the vertical profile. With a focus on water vapor, this dataset reveals that both hydration and dehydration are evident above tropical cyclones. We find that the water vapor above overshooting deep convective clouds (DCC-OTs) is up to 40 % higher than its climatological value. Hydration also appears above clouds located below tropopause (NTTL), possibly from advected moist plumes from nearby overshooting injections, although further investigations are necessary. On the other hand, dehydration exists above non-overshooting TTL clouds (TTL-OTHERs), which are associated with a colder TTL. This dehydration may result from ice deposition growth and sedimentation in the cold environment. Despite the competing effects of DCC-OTs and TTL-OTHERs, tropical cyclones overall hydrate the atmospheric column above them.

Interestingly, tropical cyclones also give rise to prevailing radiative cooling in the TTL by significantly increasing the TTL cloud. We find that the convective hydration radiatively cools the TTL under both clear-sky and cloudy-sky conditions which inhibits the diabatic ascent that typically prevails in the TTL. Therefore, the radiative balance under the influence of cyclones is not in favor of maintaining the moisture-enriched air within the TTL nor transporting it vertically to the stratosphere. Considering that most trajectory modeling studies of UTLS water vapor tend to use diabatic heating rates which are either fixed at seasonal mean values or from reanalysis datasets, our study suggests that it is important to include instantaneous radiative transfer calculations to account for the radiative effects of cloud and water vapor.

As discussed in Chapter 4, the capability of satellite retrieval products in detecting the water vapor variability is limited by averaging kernels and instrument sampling footprints. Hence, it is worthwhile to further investigate how convective hydration, as shown in the NWP simulation conducted in Chapter 3, can be captured by current and future satellite instruments. In combination with trajectory calculations, we will also examine how the retrieved humidity fields above convection agree with in-situ observations of convective detrainment.

Finally, it is promising to obtain a global assessment of direct convective impacts on UTLS water vapor by extending our current study to include other tropical and extratropical deep convective systems. This assessment is warranted in near future. We will also seek opportunities to apply this method with other satellite instruments. For example, future instruments (e.g., FORUM and TICFIRE) that cover far-infrared channels can improve the sensitivity to UTLS water vapor and cloud microphysical properties, as demonstrated in Chapters 2 and 3. Instruments in geostationary orbit, such as IRS and GIIRS, also offer advantages in increasing the collocation with other space-borne active sensors over convective regions and offering the potential for time-continuous observations.

Bibliography

J. G. Anderson, D. M. Wilmouth, J. B. Smith, and D. S. Sayres. UV dosage levels in summer: Increased risk of ozone loss from convectively injected water vapor. *Science*, 337(6096):835–839, 2012.

R. A. Anthes, P. Bernhardt, Y. Chen, L. Cucurull, K. Dymond, D. Ector, S. Healy, S.-P. Ho, D. Hunt, Y.-H. Kuo, et al. The COSMIC/FORMOSAT-3 mission: Early results. *Bulletin of the American Meteorological Society*, 89(3):313–334, 2008.

H. Aumann and A. Ruzmaikin. Frequency of deep convective clouds in the tropical zone from 10 years of AIRS data. *Atmospheric Chemistry and Physics*, 13(21):10795, 2013.

H. Aumann, S. DeSouza-Machado, and A. Behrangi. Deep convective clouds at the tropopause. *Atmospheric Chemistry and Physics*, 11(3):1167, 2011.

M. A. Avery, S. M. Davis, K. H. Rosenlof, H. Ye, and A. E. Dessler. Large anomalies in lower stratospheric water vapour and ice during the 2015–2016 El Niño. *Nature Geoscience*, 10(6):405–409, 2017.

M. Bani Shahabadi and Y. Huang. Measuring stratospheric H2O with an airborne spectrometer. *Journal of Atmospheric and Oceanic Technology*, 31(7):1502–1515, 2014.

B. A. Baum, P. Yang, A. J. Heymsfield, C. G. Schmitt, Y. Xie, A. Bansemer, Y.-X. Hu, and Z. Zhang. Improvements in shortwave bulk scattering and absorption models for the remote sensing of ice clouds. *Journal of Applied Meteorology and Climatology*, 50(5): 1037–1056, 2011.

B. A. Baum, P. Yang, A. J. Heymsfield, A. Bansemer, B. H. Cole, A. Merrelli, C. Schmitt, and C. Wang. Ice cloud single-scattering property models with the full phase matrix at wavelengths from 0.2 to 100 μm. *Journal of Quantitative Spectroscopy and Radiative Transfer*, 146:123–139, 2014.

R. Beer, T. A. Glavich, and D. M. Rider. Tropospheric Emission Spectrometer for the Earth Observing System's Aura satellite. *Applied optics*, 40(15):2356–2367, 2001.

S. Bélair, J. Mailhot, C. Girard, and P. Vaillancourt. Boundary layer and shallow cumulus clouds in a medium-range forecast of a large-scale weather system. *Monthly weather review*, 133(7):1938–1960, 2005.

A. Berk and F. Hawes. Validation of MODTRAN® 6 and its line-by-line algorithm. *Journal of Quantitative Spectroscopy and Radiative Transfer*, 203:542–556, 2017.

A. Berk, G. P. Anderson, P. K. Acharya, L. S. Bernstein, L. Muratov, J. Lee, M. Fox, S. M. Adler-Golden, J. H. Chetwynd, M. L. Hoke, et al. MODTRAN 5: a reformulated atmospheric band model with auxiliary species and practical multiple scattering options: update. In *Defense and Security*, pages 662–667. International Society for Optics and Photonics, 2005.

A. Berk, P. Conforti, R. Kennett, T. Perkins, F. Hawes, and J. Van Den Bosch. MODTRAN® 6: A major upgrade of the MODTRAN® radiative transfer code. In *2014 6th Workshop on Hyperspectral Image and Signal Processing: Evolution in Remote Sensing (WHISPERS)*, pages 1–4. IEEE, 2014.

P. F. Bernath, C. T. McElroy, M. Abrams, C. D. Boone, M. Butler, C. Camy-Peyret, M. Carleer, C. Clerbaux, P.-F. Coheur, R. Colin, et al. Atmospheric chemistry experiment (ACE): mission overview. *Geophysical Research Letters*, 32(15), 2005.

R. Biondi, W. Randel, S.-P. Ho, T. Neubert, and S. Syndergaard. Thermal structure of intense convective clouds derived from GPS radio occultations. *Atmospheric Chemistry and Physics*, 12(12):5309–5318, 2012.

R. Biondi, S.-P. Ho, W. Randel, S. Syndergaard, and T. Neubert. Tropical cyclone cloud-top height and vertical temperature structure detection using GPS radio occultation measurements. *Journal of Geophysical Research: Atmospheres*, 118(11):5247–5259, 2013.

J.-P. Blanchet, A. Royer, F. Châteauneuf, Y. Bouzid, Y. Blanchard, J.-F. Hamel, J. de Lafontaine, P. Gauthier, N. T. O'Neill, O. Pancrati, et al. TICFIRE: a far infrared payload to monitor the evolution of thin ice clouds. In *Sensors, Systems, and Next-Generation*

Satellites XV, volume 8176, page 81761K. International Society for Optics and Photonics, 2011.

H. J. Bloom. The Cross-track Infrared Sounder (CrIS): a sensor for operational meteorological remote sensing. In *IGARSS 2001. Scanning the Present and Resolving the Future. Proceedings. IEEE 2001 International Geoscience and Remote Sensing Symposium (Cat. No. 01CH37217)*, volume 3, pages 1341–1343. IEEE, 2001.

D. Blumstein, G. Chalon, T. Carlier, C. Buil, P. Hebert, T. Maciaszek, G. Ponce, T. Phulpin, B. Tournier, D. Simeoni, et al. IASI instrument: Technical overview and measured performances. In *Infrared Spaceborne Remote Sensing XII*, volume 5543, pages 196–207. International Society for Optics and Photonics, 2004.

M. Bolot and S. Fueglistaler. Tropical water fluxes dominated by deep convection up to near tropopause levels. *Geophysical Research Letters*, 2021.

A. Brewer. Evidence for a world circulation provided by the measurements of helium and water vapour distribution in the stratosphere. *Quarterly Journal of the Royal Meteorological Society*, 75(326):351–363, 1949.

M. T. Chahine, T. S. Pagano, H. H. Aumann, R. Atlas, et al. AIRS: Improving weather forecasting and providing new data on greenhouse gases. *Bulletin of the American Meteorological Society*, 87(7):911, 2006.

T. Corti, B. P. Luo, Q. Fu, H. Vömel, and T. Peter. The impact of cirrus clouds on tropical troposphere-to-stratosphere transport. *Atmospheric Chemistry and Physics*, 6(9):2539–2547, 2006.

T. Corti, B. Luo, M. De Reus, D. Brunner, F. Cairo, M. Mahoney, G. Martucci, R. Matthey, V. Mitev, F. Dos Santos, et al. Unprecedented evidence for deep convection hydrating the tropical stratosphere. *Geophysical Research Letters*, 35(10), 2008.

J. Côté, S. Gravel, A. Méthot, A. Patoine, M. Roch, and A. Staniforth. The operational CMC–MRB global environmental multiscale (GEM) model. part i: Design considerations and formulation. *Monthly Weather Review*, 126(6):1373–1395, 1998.

S. M. Davis, M. I. Hegglin, M. Fujiwara, R. Dragani, Y. Harada, C. Kobayashi, C. Long, G. L. Manney, E. R. Nash, G. L. Potter, S. Tegtmeier, T. Wang, K. Wargan, and J. S. Wright. Assessment of upper tropospheric and stratospheric water vapor and ozone in reanalyses as part of S-RIP. *Atmospheric Chemistry and Physics*, 17(20):12743–12778, 2017.

D. Dee, S. Uppala, A. Simmons, P. Berrisford, P. Poli, S. Kobayashi, U. Andrae, M. Balmaseda, G. Balsamo, P. Bauer, et al. The ERA-Interim reanalysis: Configuration and performance of the data assimilation system. *Quarterly Journal of the royal meteorological society*, 137(656):553–597, 2011.

J. Delanoë and R. J. Hogan. A variational scheme for retrieving ice cloud properties from combined radar, lidar, and infrared radiometer. *Journal of Geophysical Research: Atmospheres*, 113(D7), 2008.

J. Delanoë and R. J. Hogan. Combined CloudSat-CALIPSO-MODIS retrievals of the properties of ice clouds. *Journal of Geophysical Research: Atmospheres*, 115(D4), 2010.

S. DeSouza-Machado, L. L. Strow, A. Tangborn, X. Huang, X. Chen, X. Liu, W. Wu, and Q. Yang. Single-footprint retrievals for airs using a fast twoslab cloud-representation model and the sarta all-sky infrared radiative transfer algorithm. *Atmospheric Measurement Techniques*, 11(1), 2018.

A. Dessler, E. Hintsa, E. Weinstock, J. Anderson, and K. Chan. Mechanisms controlling water vapor in the lower stratosphere:"a tale of two stratospheres". *Journal of Geophysical Research: Atmospheres*, 100(D11):23167–23172, 1995.

A. Dessler, M. Schoeberl, T. Wang, S. Davis, and K. Rosenlof. Stratospheric water vapor feedback. *Proceedings of the National Academy of Sciences*, 110(45):18087–18091, 2013.

K. Drdla and R. Müller. Temperature thresholds for chlorine activation and ozone loss in the polar stratosphere. In *Annales geophysicae*, volume 30, pages 1055–1073. Copernicus GmbH, 2012.

V. L. Dvortsov and S. Solomon. Response of the stratospheric temperatures and ozone to past and future increases in stratospheric humidity. *Journal of Geophysical Research: Atmospheres*, 106(D7):7505–7514, 2001.

J. Feng and Y. Huang. Cloud-assisted retrieval of lower-stratospheric water vapor from nadir-view satellite measurements. *Journal of Atmospheric and Oceanic Technology*, 35 (3):541–553, 2018.

E. J. Fetzer, W. G. Read, D. Waliser, B. H. Kahn, B. Tian, H. Vömel, F. W. Irion, H. Su, A. Eldering, M. de la Torre Juarez, J. Jiang, and V. Dang. Comparison of upper tropospheric water vapor observations from the Microwave Limb Sounder and Atmospheric Infrared Sounder. *Journal of Geophysical Research: Atmospheres*, 113 (D22):n/a–n/a, 2008. ISSN 2156-2202. doi: 10.1029/2008JD010000. URL `http://dx.doi.org/10.1029/2008JD010000`. D22110.

S. Fueglistaler, A. Dessler, T. Dunkerton, I. Folkins, Q. Fu, and P. W. Mote. Tropical tropopause layer. *Reviews of Geophysics*, 47(1), 2009.

A. Gambacorta, C. Barnet, W. Wolf, T. King, N. Nalli, M. Wilson, L. Soulliard, K. Zang, X. Xiong, and M. Goldberg. The NOAA operational hyper spectral retrieval algorithm: a cross-comparison among the CrIS, IASI and AIRS processing system. In *19th International TOVS Study Conference, Jeju Island, Korea*, 2014.

A. Gettelman, W. Randel, F. Wu, and S. Massie. Transport of water vapor in the tropical tropopause layer. *Geophysical research letters*, 29(1):9–1, 2002a.

A. Gettelman, M. Salby, and F. Sassi. Distribution and influence of convection in the tropical tropopause region. *Journal of Geophysical Research: Atmospheres*, 107(D10): ACL–6, 2002b.

A. Gettelman, E. M. Weinstock, E. J. Fetzer, F. W. Irion, A. Eldering, E. C. Richard, K. H. Rosenlof, T. L. Thompson, J. V. Pittman, C. R. Webster, and R. L. Herman. Validation of Aqua satellite data in the upper troposphere and lower stratosphere with in situ aircraft instruments. *Geophysical Research Letters*, 31(22):n/a–n/a, 2004. ISSN 1944-8007. doi: 10.1029/2004GL020730. URL `http://dx.doi.org/10.1029/2004GL020730`. L22107.

C. Girard, A. Plante, M. Desgagné, R. McTaggart-Cowan, J. Côté, M. Charron, S. Gravel, V. Lee, A. Patoine, A. Qaddouri, et al. Staggered vertical discretization of the Canadian Environmental Multiscale (GEM) model using a coordinate of the log-hydrostatic-pressure type. *Monthly Weather Review*, 142(3):1183–1196, 2014.

D. Grosvenor, T. Choularton, H. Coe, and G. Held. A study of the effect of overshooting deep convection on the water content of the TTL and lower stratosphere from Cloud Resolving Model simulations. *Atmospheric Chemistry and Physics*, 7(18):4977–5002, 2007.

J. Hampson. Photochemical behavior of the ozone layer, Canadian Armament Research and Development Establishment. *Tech. Note*, 1964.

I. M. Held and B. J. Soden. Water vapor feedback and global warming. *Annual review of energy and the environment*, 25(1):441–475, 2000.

H. Hersbach, B. Bell, P. Berrisford, S. Hirahara, A. Horányi, J. Muñoz-Sabater, J. Nicolas, C. Peubey, R. Radu, D. Schepers, et al. The ERA5 global reanalysis. *Quarterly Journal of the Royal Meteorological Society*, 146(730):1999–2049, 2020.

A. J. Heymsfield. Ice particles observed in a cirriform cloud at- 83 C and implications for polar stratospheric clouds. *Journal of the atmospheric sciences*, 43(8):851–855, 1986.

A. J. Heymsfield, C. Schmitt, and A. Bansemer. Ice cloud particle size distributions and pressure-dependent terminal velocities from in situ observations at temperatures from 0° to- 86° c. *Journal of Atmospheric Sciences*, 70(12):4123–4154, 2013.

C. E. Holloway and J. D. Neelin. The convective cold top and quasi equilibrium. *Journal of the atmospheric sciences*, 64(5):1467–1487, 2007.

K. Holmlund, J. Grandell, J. Schmetz, R. Stuhlmann, B. Bojkov, R. Munro, M. Lekouara, D. Coppens, B. Viticchie, T. August, et al. METEOSAT THIRD GENERATION (MTG): Continuation and innovation of observations from geostationary orbit. *Bulletin of the American Meteorological Society*, pages 1–71, 2021.

J. R. Holton and A. Gettelman. Horizontal transport and the dehydration of the stratosphere. *Geophysical Research Letters*, 28(14):2799–2802, 2001.

J. R. Holton, P. H. Haynes, M. E. McIntyre, A. R. Douglass, R. B. Rood, and L. Pfister. Stratosphere-troposphere exchange. *Reviews of geophysics*, 33(4):403–439, 1995.

Y. Huang and M. Bani Shahabadi. Why logarithmic? a note on the dependence of radiative forcing on gas concentration. *Journal of Geophysical Research: Atmospheres*, 119(24), 2014.

Y. Huang, V. Ramaswamy, X. Huang, Q. Fu, and C. Bardeen. A strict test in climate modeling with spectrally resolved radiances: Gcm simulation versus airs observations. *Geophysical Research Letters*, 34(24), 2007.

Y. Huang, S. S. Leroy, and J. G. Anderson. Determining longwave forcing and feedback using infrared spectra and GNSS radio occultation. *Journal of climate*, 23(22):6027–6035, 2010.

Y. Huang, M. Zhang, Y. Xia, Y. Hu, and S.-W. Son. Is there a stratospheric radiative feedback in global warming simulations? *Climate dynamics*, 46(1-2):177–186, 2016.

D. F. Hurst, S. J. Oltmans, H. Vömel, K. H. Rosenlof, S. M. Davis, E. A. Ray, E. G. Hall, and A. F. Jordan. Stratospheric water vapor trends over Boulder, Colorado: Analysis of the 30 year boulder record. *Journal of Geophysical Research: Atmospheres*, 116(D2), 2011.

M. J. Iacono, E. J. Mlawer, S. A. Clough, and J.-J. Morcrette. Impact of an improved longwave radiation model, RRTM, on the energy budget and thermodynamic properties of the NCAR community climate model, CCM3. *Journal of Geophysical Research: Atmospheres*, 105(D11):14873–14890, 2000.

IPCC. *Climate Change: The IPCC Scientific Assessment (eds J. T. Houghton, G. J. Jenkins, J. J. Ephraums.)*. Mass, Cambridge, 1990.

F. W. Irion, B. H. Kahn, M. M. Schreier, E. J. Fetzer, E. Fishbein, D. Fu, P. Kalmus, R. C. Wilson, S. Wong, and Q. Yue. Single-footprint retrievals of temperature, water vapor and cloud properties from AIRS. *Atmospheric Measurement Techniques Discussions*, 2017:1–35, 2017. doi: 10.5194/amt-2017-197. URL https://www.atmos-meas-tech-discuss.net/amt-2017-197/.

F. W. Irion, B. H. Kahn, M. M. Schreier, E. J. Fetzer, E. Fishbein, D. Fu, P. Kalmus, R. C. Wilson, S. Wong, and Q. Yue. Single-footprint retrievals of temperature, water vapor and cloud properties from airs. *Atmospheric Measurement Techniques*, 11(2):971–995, 2018.

E. Jensen, A. Ackerman, and J. Smith. Can overshooting convection dehydrate the tropical tropopause layer? *Journal of Geophysical Research: Atmospheres*, 112(D11), 2007.

E. J. Jensen, L. Pfister, D. E. Jordan, D. W. Fahey, P. A. Newman, T. Thornberry, A. Rollins, G. Diskin, T. P. Bui, M. McGill, et al. The NASA Airborne Tropical TRopopause EXperiment (ATTREX). *SPARC Newsletter*, 41:15–24, 2013.

B. Jiang, W. Lin, C. Hu, and Y. Wu. Tropical cyclones impact on tropopause and the lower stratosphere vapour based on satellite data. *Atmospheric Science Letters*, page e1006, 2020.

J. H. Jiang, H. Su, C. Zhai, V. S. Perun, A. Del Genio, L. S. Nazarenko, L. J. Donner, L. Horowitz, C. Seman, J. Cole, et al. Evaluation of cloud and water vapor simulations in CMIP5 climate models using NASA "A-Train" satellite observations. *Journal of Geophysical Research: Atmospheres*, 117(D14), 2012.

J. H. Jiang, H. Su, C. Zhai, L. Wu, K. Minschwaner, A. M. Molod, and A. M. Tompkins. An assessment of upper troposphere and lower stratosphere water vapor in MERRA, MERRA2, and ECMWF reanalyses using Aura MLS observations. *Journal of Geophysical Research: Atmospheres*, 120(22):11–468, 2015.

B. H. Kahn, F. W. Irion, V. T. Dang, E. M. Manning, S. L. Nasiri, C. M. Naud, J. M. Blaisdell, M. M. Schreier, Q. Yue, K. W. Bowman, E. J. Fetzer, G. C. Hulley, K. N. Liou, D. Lubin, S. C. Ou, J. Susskind, Y. Takano, B. Tian, and J. R. Worden. The Atmospheric Infrared Sounder version 6 cloud products. *Atmospheric Chemistry and Physics*, 14(1):399–426, 2014. doi: 10.5194/acp-14-399-2014. URL https://www.atmos-chem-phys.net/14/399/2014/.

D. B. Kirk-Davidoff, E. J. Hintsa, J. G. Anderson, and D. W. Keith. The effect of climate change on ozone depletion through changes in stratospheric water vapour. *Nature*, 402 (6760):399–401, 1999.

D. Kley. SPARC assessment of upper tropospheric and stratospheric water vapor. *WCRP-113, WMO/TD*, 1043, 2000.

T. S. L'Ecuyer and J. H. Jiang. Touring the atmosphere aboard the A-Train. In *AIP Conference Proceedings*, volume 1401, pages 245–256. American Institute of Physics, 2011.

K.-O. Lee, T. Dauhut, J.-P. Chaboureau, S. Khaykin, M. Krämer, and C. Rolf. Convective hydration in the tropical tropopause layer during the StratoClim aircraft campaign: pathway of an observed hydration patch. 2019.

Z. Li, J. Li, P. Wang, A. Lim, J. Li, T. J. Schmit, R. Atlas, S.-A. Boukabara, and R. N. Hoffman. Value-added impact of geostationary hyperspectral infrared sounders on local severe storm forecasts—via a quick regional OSSE. *Advances in Atmospheric Sciences*, 35(10):1217–1230, 2018.

N. Livesey, W. Read, P. Wagner, L. Froidevaux, A. Lambert, G. Manney, L. Millán Valle, H. Pumphrey, M. Santee, M. Schwartz, et al. Version 4.2 x level 2 data quality and description document, JPL D-33509 Rev. C, 2017.

T. L'Ecuyer. Level 2 fluxes and heating rates product process description and interface control document, v. 5, 2007.

R. A. McClatchey. *Optical properties of the atmosphere*. Number 411. Air Force Cambridge Research Laboratories, Office of Aerospace Research, United States Air Force, 1972.

J. Milbrandt and M. Yau. A multimoment bulk microphysics parameterization. part i: Analysis of the role of the spectral shape parameter. *Journal of the atmospheric sciences*, 62(9):3051–3064, 2005.

J. F. Mitchell. The "greenhouse" effect and climate change. *Reviews of Geophysics*, 27(1): 115–139, 1989.

R. B. Neale, C.-C. Chen, A. Gettelman, P. H. Lauritzen, S. Park, D. L. Williamson, A. J. Conley, R. Garcia, D. Kinnison, J.-F. Lamarque, et al. Description of the NCAR community atmosphere model (CAM 5.0). *NCAR Tech. Note NCAR/TN-486+ STR*, 2010.

K. Okamoto, H. Owada, T. Fujita, M. Kazumori, M. Otsuka, H. Seko, Y. Ota, N. Uekiyo, H. Ishimoto, M. Hayashi, et al. Assessment of the potential impact of a hyperspectral infrared sounder on the himawari follow-on geostationary satellite. *SOLA*, 2020.

E. Olsen, E. Fetzer, G. Hulley, E. Manning, J. Blaisdell, L. Iredell, J. Susskind, J. Warner, Z. Wei, W. Blackwell, et al. AIRS/AMSU/HSB version 6 level 2 product user guide. *Jet Propulsion Laboratory, Version*, 1, 2013.

S. J. Oltmans, H. Vömel, D. J. Hofmann, K. H. Rosenlof, and D. Kley. The increase in stratospheric water vapor from balloonborne, frostpoint hygrometer measurements at Washington, DC, and Boulder, Colorado. *Geophysical Research Letters*, 27(21):3453–3456, 2000.

L. Palchetti, H. Brindley, R. Bantges, S. Buehler, C. Camy-Peyret, B. Carli, U. Cortesi, S. Del Bianco, G. Di Natale, B. Dinelli, et al. unique far-infrared satellite observations to better understand how earth radiates energy to space. *Bulletin of the American Meteorological Society*, 1(aop):1–52, 2020.

C. L. Parkinson. Aqua: An earth-observing satellite mission to examine water and other climate variables. *IEEE Transactions on Geoscience and Remote Sensing*, 41(2):173–183, 2003.

P. Partain. Cloudsat ECMWF-AUX auxiliary data process description and interface control document. *Cooperative Institute for Research in the Atmosphere Rep*, 2004.

S. Platnick, M. D. King, S. A. Ackerman, W. P. Menzel, B. A. Baum, J. C. Riédi, and R. A. Frey. The modis cloud products: Algorithms and examples from terra. *IEEE Transactions on geoscience and Remote Sensing*, 41(2):459–473, 2003.

R. A. Plumb. Stratospheric transport. *Journal of the Meteorological Society of Japan. Ser. II*, 80(4B):793–809, 2002.

Z. Qu, Y. Huang, P. A. Vaillancourt, J. N. Cole, J. A. Milbrandt, M.-K. Yau, K. Walker, and J. de Grandpré. Simulation of convective moistening of the extratropical lower stratosphere using a numerical weather prediction model. *Atmospheric Chemistry & Physics*, 20(4), 2020.

W. Randel and M. Park. Diagnosing observed stratospheric water vapor relationships to the cold point tropical tropopause. *Journal of Geophysical Research: Atmospheres*, 124 (13):7018–7033, 2019.

W. J. Randel, F. Wu, S. J. Oltmans, K. Rosenlof, and G. E. Nedoluha. Interannual changes of stratospheric water vapor and correlations with tropical tropopause temperatures. *Journal of the Atmospheric Sciences*, 61(17):2133–2148, 2004.

W. J. Randel, K. Zhang, and R. Fu. What controls stratospheric water vapor in the nh summer monsoon regions? *Journal of Geophysical Research: Atmospheres*, 120(15): 7988–8001, 2015.

W. G. Read, A. Lambert, J. Bacmeister, R. E. Cofield, L. E. Christensen, D. T. Cuddy, W. H. Daffer, B. J. Drouin, E. Fetzer, L. Froidevaux, R. Fuller, R. Herman, R. F. Jarnot, J. H. Jiang, Y. B. Jiang, K. Kelly, B. W. Knosp, L. J. Kovalenko, N. J. Livesey, H.-C. Liu, G. L. Manney, H. M. Pickett, H. C. Pumphrey, K. H. Rosenlof, X. Sabounchi, M. L. Santee, M. J. Schwartz, W. V. Snyder, P. C. Stek, H. Su, L. L. Takacs, R. P. Thurstans, H. Vömel, P. A. Wagner, J. W. Waters, C. R. Webster, E. M. Weinstock, and D. L. Wu. Aura Microwave Limb Sounder upper tropospheric and lower stratospheric H2O and relative humidity with respect to ice validation. *Journal of Geophysical Research: Atmospheres*, 112(D24):n/a–n/a, 2007. ISSN 2156-2202. doi: 10.1029/2007JD008752. URL http://dx.doi.org/10.1029/2007JD008752. D24S35.

L. Rivoire, T. Birner, and J. A. Knaff. Evolution of the upper-level thermal structure in tropical cyclones. *Geophysical Research Letters*, 43(19):10–530, 2016.

L. Rivoire, T. Birner, J. A. Knaff, and N. Tourville. Quantifying the radiative impact of clouds on tropopause layer cooling in tropical cyclones. *Journal of Climate*, (2020), 2020.

F. Robinson and S. Sherwood. Modeling the impact of convective entrainment on the tropical tropopause. *Journal of the atmospheric sciences*, 63(3):1013–1027, 2006.

C. D. Rodgers. *Inverse methods for atmospheric sounding: theory and practice*, volume 2. World scientific, 2000.

A. Rollins, T. Thornberry, R. Gao, S. Woods, R. Lawson, T. Bui, E. Jensen, and D. Fahey. Observational constraints on the efficiency of dehydration mechanisms in the tropical tropopause layer. *Geophysical Research Letters*, 43(6):2912–2918, 2016.

D. M. Romps and Z. Kuang. Overshooting convection in tropical cyclones. *Geophysical Research Letters*, 36(9), 2009.

K. Rosenlof, S. Oltmans, D. Kley, J. Russell III, E.-W. Chiou, W. Chu, D. Johnson, K. Kelly, H. Michelsen, G. Nedoluha, et al. Stratospheric water vapor increases over the past half-century. *Geophysical research letters*, 28(7):1195–1198, 2001.

C. R. Sampson and A. J. Schrader. The automated tropical cyclone forecasting system (version 3.2). *Bulletin of the American Meteorological Society*, 81(6):1231–1240, 2000.

C. Schiller, J.-U. Grooß, P. Konopka, F. Plöger, F. dos Santos, and N. Spelten. Hydration and dehydration at the tropical tropopause. *Atmospheric Chemistry & Physics*, 9(24), 2009.

T. J. Schmit, J. Li, S. A. Ackerman, and J. J. Gurka. High-spectral-and high-temporal-resolution infrared measurements from geostationary orbit. *Journal of Atmospheric and Oceanic Technology*, 26(11):2273–2292, 2009.

M. Schoeberl, A. Dessler, and T. Wang. Simulation of stratospheric water vapor and trends using three reanalyses. *Atmospheric Chemistry and Physics*, 12(14):6475–6487, 2012.

M. Schoeberl, E. Jensen, L. Pfister, R. Ueyama, T. Wang, H. Selkirk, M. Avery, T. Thornberry, and A. Dessler. Water vapor, clouds, and saturation in the tropical tropopause layer. *Journal of Geophysical Research: Atmospheres*, 124(7):3984–4003, 2019.

M. R. Schoeberl, E. J. Jensen, L. Pfister, R. Ueyama, M. Avery, and A. E. Dessler. Convective hydration of the upper troposphere and lower stratosphere. *Journal of Geophysical Research: Atmospheres*, 123(9):4583–4593, 2018.

W. H. Schubert and B. D. McNoldy. Application of the concepts of Rossby length and Rossby depth to tropical cyclone dynamics. *Journal of Advances in Modeling Earth Systems*, 2(3), 2010.

M. Schwartz, A. Lambert, G. Manney, W. Read, N. Livesey, L. Froidevaux, C. Ao, P. Bernath, C. Boone, R. Cofield, et al. Validation of the aura microwave limb sounder temperature and geopotential height measurements. *Journal of Geophysical Research: Atmospheres*, 113(D15), 2008.

M. J. Schwartz, W. G. Read, M. L. Santee, N. J. Livesey, L. Froidevaux, A. Lambert, and G. L. Manney. Convectively injected water vapor in the north american summer lowermost stratosphere. *Geophysical Research Letters*, 40(10):2316–2321, 2013.

S. C. Sherwood, J.-H. Chae, P. Minnis, and M. McGill. Underestimation of deep convective cloud tops by thermal imagery. *Geophysical Research Letters*, 31(11), 2004.

D. T. Shindell. Climate and ozone response to increased stratospheric water vapor. *Geophysical Research Letters*, 28(8):1551–1554, 2001.

J. B. Smith. *The sources and significance of stratospheric water vapor: mechanistic studies from Equator to Pole*. PhD thesis, 2013.

J. B. Smith, D. M. Wilmouth, K. M. Bedka, K. P. Bowman, C. R. Homeyer, J. A. Dykema, M. R. Sargent, C. E. Clapp, S. S. Leroy, D. S. Sayres, et al. A case study of convectively sourced water vapor observed in the overworld stratosphere over the united states. *Journal of Geophysical Research: Atmospheres*, 122(17):9529–9554, 2017.

D. L. Solomon, K. P. Bowman, and C. R. Homeyer. Tropopause-penetrating convection from three-dimensional gridded nexrad data. *Journal of Applied Meteorology and Climatology*, 55(2):465–478, 2016.

S. Solomon, R. R. Garcia, F. S. Rowland, and D. J. Wuebbles. On the depletion of antarctic ozone. *Nature*, 321(6072):755–758, 1986.

S. Solomon, K. H. Rosenlof, R. W. Portmann, J. S. Daniel, S. M. Davis, T. J. Sanford, and G.-K. Plattner. Contributions of stratospheric water vapor to decadal changes in the rate of global warming. *Science*, 327(5970):1219–1223, 2010.

G. L. Stephens, D. G. Vane, R. J. Boain, G. G. Mace, K. Sassen, Z. Wang, A. J. Illingworth, E. J. O'connor, W. B. Rossow, S. L. Durden, et al. The CloudSat mission and the A-Train:

A new dimension of space-based observations of clouds and precipitation. *Bulletin of the American Meteorological Society*, 83(12):1771–1790, 2002.

G. L. Stephens, D. G. Vane, S. Tanelli, E. Im, S. Durden, M. Rokey, D. Reinke, P. Partain, G. G. Mace, R. Austin, et al. Cloudsat mission: Performance and early science after the first year of operation. *Journal of Geophysical Research: Atmospheres*, 113(D8), 2008.

Y. Sun and Y. Huang. An examination of convective moistening of the lower stratosphere using satellite data. *Earth and Space Science*, 2(7):320–330, 2015.

J. Susskind, C. D. Barnet, and J. M. Blaisdell. Retrieval of atmospheric and surface parameters from AIRS/AMSU/HSB data in the presence of clouds. *IEEE Transactions on Geoscience and Remote Sensing*, 41(2):390–409, 2003.

J. Susskind, J. M. Blaisdell, L. Iredell, and F. Keita. Improved temperature sounding and quality control methodology using AIRS/AMSU data: The AIRS science team version 5 retrieval algorithm. *IEEE Transactions on Geoscience and Remote Sensing*, 49(3): 883–907, 2011.

H. Takahashi, H. Su, and J. H. Jiang. Error analysis of upper tropospheric water vapor in CMIP5 models using “A-Train” satellite observations and reanalysis data. *Climate dynamics*, 46(9-10):2787–2803, 2016.

N. Tourville, G. Stephens, M. DeMaria, and D. Vane. Remote sensing of tropical cyclones: Observations from CloudSat and A-Train profilers. *Bulletin of the American Meteorological Society*, 96(4):609–622, 2015.

D. D. Turner and W. G. Blumberg. Improvements to the AERIoe thermodynamic profile retrieval algorithm. *IEEE Journal of Selected Topics in Applied Earth Observations and Remote Sensing*, 12(5):1339–1354, 2018.

R. Ueyama, E. J. Jensen, and L. Pfister. Convective influence on the humidity and clouds in the tropical tropopause layer during boreal summer. *Journal of Geophysical Research: Atmospheres*, 123(14):7576–7593, 2018.

B. Vogel, T. Feck, and J.-U. Grooß. Impact of stratospheric water vapor enhancements caused by ch4 and h2o increase on polar ozone loss. *Journal of Geophysical Research: Atmospheres*, 116(D5), 2011.

X. Wang and H. Jiang. A 13-year global climatology of tropical cyclone warm-core structures from AIRS data. *Monthly Weather Review*, 147(3):773–790, 2019.

Z. Wang and K. Sassen. Level 2 cloud scenario classification product process description and interface control document. *Coop. Inst. for Res. in the Atmos*, 2007.

J. W. Waters, L. Froidevaux, R. S. Harwood, R. F. Jarnot, H. M. Pickett, W. G. Read, P. H. Siegel, R. E. Cofield, M. J. Filipiak, D. A. Flower, et al. The earth observing system microwave limb sounder (eos mls) on the aura satellite. *IEEE Transactions on Geoscience and Remote Sensing*, 44(5):1075–1092, 2006.

E. Weinstock, J. Smith, D. Sayres, J. Pittman, J. Spackman, E. Hintsa, T. Hanisco, E. Moyer, J. St Clair, M. Sargent, et al. Validation of the Harvard Lyman-α in situ water vapor instrument: Implications for the mechanisms that control stratospheric water vapor. *Journal of Geophysical Research: Atmospheres*, 114(D23), 2009.

F. Werner, M. Schwartz, N. Livesey, W. Read, and M. Santee. Extreme outliers in lower stratospheric water vapor over north america observed by MLS: Relation to overshooting convection diagnosed from colocated aqua-modis data. *Geophysical Research Letters*, 47(24):e2020GL090131, 2020.

R. Wetherald and S. Manabe. Cloud feedback processes in a general circulation model. *Journal of Atmospheric Sciences*, 45(8):1397–1416, 1988.

B. A. Wielicki, D. Young, M. Mlynczak, K. Thome, S. Leroy, J. Corliss, J. Anderson, C. Ao, R. Bantges, F. Best, et al. Achieving climate change absolute accuracy in orbit. *Bulletin of the American Meteorological Society*, 94(10):1519–1539, 2013.

D. M. Winker, J. R. Pelon, and M. P. McCormick. CALIPSO mission: spaceborne lidar for observation of aerosols and clouds. In *Lidar Remote Sensing for Industry and Environment Monitoring III*, volume 4893, pages 1–11. International Society for Optics and Photonics, 2003.

WMO. *Definition of the tropopause*, volume 6. 1957.

S. Wong, E. J. Fetzer, M. Schreier, G. Manipon, E. F. Fishbein, B. H. Kahn, Q. Yue, and F. W. Irion. Cloud-induced uncertainties in AIRS and ECMWF temperature and specific humidity. *Journal of Geophysical Research: Atmospheres*, 120(5):1880–1901, 2015.

J. Wright and S. Fueglistaler. Large differences in reanalyses of diabatic heating in the tropical upper troposphere and lower stratosphere. *Atmospheric Chemistry & Physics*, 13(18), 2013.

J. S. Wright, X. Sun, P. Konopka, K. Krüger, A. M. Molod, S. Tegtmeier, G. J. Zhang, and X. Zhao. Differences in tropical high clouds among reanalyses: origins and radiative impacts. *Atmospheric Chemistry & Physics*, 2020.

P. Yang, L. Bi, B. A. Baum, K.-N. Liou, G. W. Kattawar, M. I. Mishchenko, and B. Cole. Spectrally consistent scattering, absorption, and polarization properties of atmospheric ice crystals at wavelengths from 0.2 to 100 μ m. *Journal of the Atmospheric Sciences*, 70(1):330–347, 2013.

Q. Yang, Q. Fu, and Y. Hu. Radiative impacts of clouds in the tropical tropopause layer. *Journal of Geophysical Research: Atmospheres*, 115(D4), 2010.

A. H. Young, J. J. Bates, and J. A. Curry. Application of cloud vertical structure from CloudSat to investigate MODIS-derived cloud properties of cirriform, anvil, and deep convective clouds. *Journal of Geophysical Research: Atmospheres*, 118(10):4689–4699, 2013.

W. Yu, A. E. Dessler, M. Park, and E. J. Jensen. Influence of convection on stratospheric water vapor in the North American monsoon region. *Atmospheric Chemistry and Physics*, 20(20):12153–12161, 2020.

D. K. Zhou, W. L. Smith Sr, X. Liu, A. M. Larar, H.-L. A. Huang, J. Li, M. J. McGill, and S. A. Mango. Thermodynamic and cloud parameter retrieval using infrared spectral data. *Geophysical research letters*, 32(15), 2005.

List of Publications

Published:

- Feng, J. and Huang, Y., 2018. Cloud-Assisted Retrieval of Lower-Stratospheric Water Vapor from Nadir-View Satellite Measurements. Journal of Atmospheric and Oceanic Technology, 35(3), pp.541-553, https://doi.org/10.1175/JTECH-D-17-0132.1.
- Feng, J. and Huang, Y., 2019. Diffusivity-Factor Approximation for Spectral Outgoing Longwave Radiation. Journal of the Atmospheric Sciences, 76(7), pp.2171-2180, https://doi.org/10.1175/JAS-D-18-0246.1.

Under Review:

- Feng, J., Huang, Y., Zhipeng, Q., 2021. A simulation experiment-based assessment of retrievals of above-cloud temperature and water vapor using hyperspectral infrared sounder. Atmospheric Measurement Techniques Discussions, https://doi.org/10.5194/amt-2020-518.
- Feng, J. and Huang, Y., 2021. Impacts of tropical cyclones on the thermodynamic conditions in the tropical tropopause layer observed by A-train satellites. Atmospheric Chemistry and Physics Discussions, https://doi.org/10.5194/acp-2021-154.